5-2013

Three Dimensional Equation of State for Core-Collapse Supernova Matter

Helena Sofia de Castro Felga Ramos Pais
hpais@utk.edu

To the Graduate Council:

I am submitting herewith a dissertation written by Helena Sofia de Castro Felga Ramos Pais entitled "Three Dimensional Equation of State for Core-Collapse Supernova Matter." I have examined the final electronic copy of this dissertation for form and content and recommend that it be accepted in partial fulfillment of the requirements for the degree of Doctor of Philosophy, with a major in Physics.

Michael W. Guidry, Major Professor

We have read this dissertation and recommend its acceptance:

William Raphael Hix, Joshua Emery, Jirina R. Stone

Accepted for the Council:
Carolyn R. Hodges

Vice Provost and Dean of the Graduate School

(Original signatures are on file with official student records.)

Three Dimensional Equation of State for Core-Collapse Supernova Matter

A Dissertation

Presented for the

Doctor of Philosophy

Degree

The University of Tennessee, Knoxville

Helena Sofia de Castro Felga Ramos Pais

May 2013

Acknowledgements

I would like to thank all the people in the Theoretical Astrophysics group at UT/ORNL for giving me the opportunity to pursue my PhD studies. In particular, I would like to thank Reuben D. Budiardja for all the help with the optimization and implementation of the codes and Eric Lingerfelt with providing interfaces with the VisIt graphics package. I also wanted to thank Raph Hix for all the useful comments concerning this work. I am also grateful to Tony Mezzacappa for his continuing interest and support during the course of this work. I also would like to thank Mike Guidry, my major professor, for his constant interest and encouragement.

And, last but definitely not least, I am also very grateful to Jirina R. Stone, my research supervisor, for all her expert guidance, motivation, support, and extreme patience throughout this work!

I also wish to thank Will Newton, who developed the original code used in this work, for all the useful discussions and input.

I am also grateful to Constança Providência, my former supervisor, for introducing me to this amazing world of compact objects, and for answering all my questions, even now that I am across the Atlantic.

Also, a big thank you to all my friends and colleagues here in Knoxville for making these 3 and half years go by so fast!

Finally, I am also very grateful to my favourite political, social, cultural, non-religious, non-profit and non-governmental Institution, that has been supporting me, inconditionally, since 1981: my parents, Carolina and Duarte. And, of course, to my

brother, Pedro, as well! This Thesis is dedicated to them. Um muito obrigada por tudo!

This research used resources of the Oak Ridge Leadership Computing Facility, located in the National Center for Computational Sciences at Oak Ridge National Laboratory, which is supported by the Office of Science of the Department of Energy under Contract DE-AC05-00OR22725. It was supported by an INCITE grant AST005: Multidimensional Simulations of Core-Collapse Supernovae, PI: Anthony Mezzacappa, Oak Ridge National Laboratory.

O sonho comanda a vida.

In *Pedra Filosofal*, 1956

António Gedeão

Abstract

The core-collapse supernova (CCSN) phenomenon, one of the most explosive events in the Universe, presents a challenge to theoretical astrophysics. Stellar matter in supernovae, experiencing most extreme pressure and temperature, undergoes transformations that cannot be simulated in terrestrial laboratories. Construction of astrophysical models is the only way towards comprehension of CCSN. The key microscopic input into CCSN models is the Equation of State (EoS), connecting the pressure of stellar matter to the energy density and temperature, dependent upon its composition. Of the large variety of forms of CCSN matter, we focus on the transitional region between homogeneous and inhomogeneous phases. Here the nuclear structures undergo a series of changes in shape from spherical to exotic deformed forms: rods, slabs, cylindrical holes and bubbles, termed "nuclear pasta". We perform a three-dimensional, finite temperature Skyrme-Hartree-Fock + BCS (3D-SHF) study of the inhomogeneous nuclear matter, where we calculate self-consistently the nuclear pasta phase and determine the phase transition between pasta and uniform matter and its character. As the nuclear matter properties depend on the effective nucleon-nucleon interaction in the 3D-SHF model, we employ four different parametrizations of the Skyrme interaction, SkM*, SLy4, NRAPR and SQMC700. For each of these interactions we calculate free energy, pressure, entropy and chemical potentials in the space of particle number densities, temperatures and proton fractions, expected to cover the pasta region. The available data analysed are for particle number densities 0.02 - 0.12 fm^{-3} [reciprocal of cubic fermi], temperatures

0 - 10 MeV and a proton fraction equal to 0.3. The data indicate a distinct discontinuity in the first derivatives of the free energy, which can be interpreted as a fingerprint of the first order transition between inhomogeneous and homogeneous supernova matter. This transition occurs naturally in our model, without a need for thermodynamic constructions. However, the transitions between distinct pasta formations are much less pronounced and hard to detect with certainty.

Contents

1 Introduction **1**

1.1 Core Collapse Supernovae 4

1.2 The Pasta Phase 8

1.3 The phase transition 13

1.3.1 First and second order phase transitions 15

1.3.2 The critical point 16

1.3.3 Order parameter 17

2 Nuclear Forces **19**

2.1 Microscopic Models 20

2.2 Phenomenological Effective Interactions 22

2.2.1 The Skyrme Interaction 23

2.2.2 Mean field approximation 27

2.2.3 The Slater determinant 28

2.2.4 The Hartree-Fock Method 28

2.2.5 Skyrme models used in this work 33

3 Computational method **34**

3.1 The Uniform Matter EoS 35

3.1.1 The finite temperature EoS 39

3.2 Non-Uniform Matter 42

3.2.1 Implementation of the 3DHFEOS Code 42

3.2.2 The computational domain and grid . . . 43
3.2.3 Boundary conditions . . . 44
3.2.4 Wavefunctions . . . 45
3.2.5 The Hartree-Fock equations . . . 48
3.2.6 Iterations . . . 49
3.2.7 Zero temperature occupation probabilities . . . 51
3.2.8 Finite temperature occupation probabilities . . . 52
3.2.9 The quadrupole constraint . . . 53
3.2.10 The Coulomb interaction . . . 55
3.2.11 Center of mass correction . . . 56
3.3 Composition of matter in CCSN . . . 57
3.3.1 Construction of the EoS . . . 58
3.4 Running of the 3DHFEOS code . . . 62

4 Numerical results **64**
4.1 The pasta phase . . . 64
4.1.1 Transition densities between pasta formations . . . 66
4.2 Transition between the pasta phase and uniform matter . . . 71
4.2.1 First order character of the phase transition . . . 73

5 Conclusions **103**
5.1 Future Work . . . 104

Bibliography **106**

Vita **119**

List of Tables

2.1 The four Skyrme parametrizations used in this Thesis. 33

3.1 Quantum numbers n_x, n_y and n_z for the first few single particle states; lowest energy is at the top. 46

4.1 Total particle number onset densities of homogeneous matter for the interactions and temperatures studied. Results of a QMD calculation (model 2) (Sonoda et al., 2008) (only a range can be given in this case) and of TF and CP approximations to RMF with NL3 and TW Lagrangians (Avancini et al., 2012) are added for comparison. For more discussion see text. 74

4.2 Symmetric nuclear matter properties at saturation density ρ_0 (energy per particle B/A, incompressibility K, symmetry energy E_{sym} and symmetry energy slope L) for the models shown in Tab. 4.1. All the quantities are in MeV, except for ρ_0, given in fm^{-3}. 76

List of Figures

1.1 Nuclear Pasta: (a) spherical (gnocchi); (b) rod (spaghetti);(c) slab (lasagna); (d) tube (penne); (e) bubble (swiss cheese?) → uniform matter. 9

4.1 First row: Pasta phases calculated using the SQMC700 Skyrme interaction, $T = 2$ MeV and $y_{\rm p} = 0.3$. Rows 2, 3, 4: 2D projection of the pasta phases on the (y,x), (x,z) and (y,z) planes, respectively. The neutron density distribution is shown at the density corresponding to the onset of each phase, known with the uncertainty given in brackets. Blue (red) color indicates the bottom (top) of the density scale: 0.001 (dark blue) - 0.02475 (light blue) - 0.0485 (green) - 0.07225 (light orange) - 0.095 (red) fm^{-3}. The pasta formation shown here appears for all the Skyrme models, but the threshold density changes somewhat, see Fig. 4.4. 65

4.2 Evolution of the neutron density distribution $\rho_{\rm N}$ for $y_p = 0.3$ and $T = 2$ MeV with increasing total particle number density ρ for all the Skyrme interactions. Blue indicates low densities and red the high densities. . 67

4.3 Evolution of the neutron density distribution $\rho_{\rm N}$ for $y_p = 0.3$ and $T = 10$ MeV with increasing total particle number density ρ for all the Skyrme interactions. Blue indicates low densities and red the high densities. 68

4.4 Comparison of phase diagrams at $T = 2$ MeV and $y_p = 0.3$ as calculated for the four Skyrme interactions used in the 3DHFEOS model. The sequence of phases from bottom to top is spherical droplets (magenta) - no pasta, rods (yellow), cross-rods (blue), slabs (red), cylindrical holes (tubes) (orange) and spherical holes (bubbles) (green). The white gaps between colored boxes represent transition regions in which calculation is not available. The onset densities of each phase can be compared with results of Sonoda et al. (2008), who found the following regions of densities (all in fm^{-3} rounded to 3 decimal places): 0.017 - 0.029 (spherical droplets), 0.034 (rods), 0.059 - 0.063 (slabs), 0.080 - 0.084 (cylindrical holes) and 0.088 - 0.109 (spherical holes). . . 70

4.5 Pressure versus density for the NRAPR interaction and the Lattimer-Swesty EoS. The transition to uniform matter happens at different densities since they are two different models. 72

4.6 Neutron density distributions for $T = 2$ MeV at the transition from non-uniform to uniform matter for all interactions. 72

4.7 Temperature dependence on the onset density of homogeneous matter, as predicted by the Skyrme, RMF (NL3, TW) and QMD2 models. Values for QMD2 model are given as a range; the arrow shows that the entry is a lower limit. The lines are added to guide the eye. For more details see text. 75

4.8 Baryonic free energy density as a function of the number density for the NRAPR Skyrme interaction and $T = 0, 2, 4$ and 6 MeV. 77

4.9 Top panel: Baryonic pressure as a function of baryon chemical potential; Bottom panel: Baryonic chemical potential as a function of the density for the NL3 model (a) and the NRAPR Skyrme interaction (b), at $T = 2$ MeV. 78

4.10 Baryon pressure as a function of baryon chemical potential for the NRAPR Skyrme interaction and (a) $T = 0$, (b) $T = 2$, (c) $T = 4$, and (d) $T = 6$ MeV. Left branch: uniform matter; Right branch: pasta phase. 80
4.11 Baryon free energy density as a function of baryon chemical potential for the NRAPR Skyrme interaction and (a) $T = 0$, (b) $T = 2$, (c) $T = 4$, and (d) $T = 6$ MeV. Left branch: uniform matter; Right branch: pasta phase. 81
4.12 Total pressure as a function of baryon chemical potential for the NRAPR Skyrme interaction and (a) $T = 0$, (b) $T = 2$, (c) $T = 4$, and (d) $T = 6$ MeV. Left branch: uniform matter; Right branch: pasta phase. 82
4.13 Total free energy density as a function of baryon chemical potential for the NRAPR Skyrme interaction and (a) $T = 0$, (b) $T = 2$, (c) $T = 4$, and (d) $T = 6$ MeV. Left branch: uniform matter; Right branch: pasta phase. 83
4.14 Total pressure as a function of the density for the NRAPR Skyrme interaction and (a) $T = 0$, (b) $T = 2$, (c) $T = 4$, and (d) $T = 6$ MeV. Left branch: pasta phase; Right branch: uniform matter. 85
4.15 Total pressure as a function of baryonic entropy density for the NRAPR Skyrme interaction and (a) $T = 2$, (b) $T = 4$, and (c) $T = 6$ MeV. . . 86
4.16 Baryonic pressure as a function of baryonic entropy density for the NRAPR Skyrme interaction and (a) $T = 2$, (b) $T = 4$, and (c) $T = 6$ MeV. 87
4.17 Total free energy density as a function of baryonic entropy density for the NRAPR Skyrme interaction and (a) $T = 2$, (b) $T = 4$, and (c) $T = 6$ MeV. 88

4.18 Baryonic free energy density as a function of baryonic entropy density for the NRAPR Skyrme interaction and (a) $T = 2$, (b) $T = 4$, and (c) $T = 6$ MeV. 89
4.19 Baryonic chemical potential as a function of number density for the NRAPR Skyrme interaction and (a) $T = 0$, (b) $T = 2$, (c) $T = 4$, and (d) $T = 6$ MeV. Left branch: pasta phase; Right branch: uniform matter. 90
4.20 Baryonic chemical potential as a function of number density for the SLy4 Skyrme interaction and (a) $T = 0$, (b) $T = 2$, (c) $T = 4$, and (d) $T = 6$ MeV. Left branch: pasta phase; Right branch: uniform matter. 91
4.21 Baryonic chemical potential as a function of number density for the QMC Skyrme interaction and (a) $T = 0$, (b) $T = 2$, (c) $T = 4$, and (d) $T = 6$ MeV. Left branch: pasta phase; Right branch: uniform matter. 92
4.22 Baryonic chemical potential as a function of number density for the SkM* Skyrme interaction and (a) $T = 0$, (b) $T = 2$, (c) $T = 4$, and (d) $T = 6$ MeV. Left branch: pasta phase; Right branch: uniform matter. 93
4.23 Baryonic entropy density as a function of number density for the NRAPR Skyrme interaction and (a) $T = 2$, (b) $T = 4$, and (c) $T = 6$ MeV. Left branch: pasta phase; Right branch: uniform matter. 94
4.24 Baryonic entropy density as a function of number density for the SLy4 Skyrme interaction and (a) $T = 2$, (b) $T = 4$, and (c) $T = 6$ MeV. Left branch: pasta phase; Right branch: uniform matter. 95
4.25 Baryonic entropy density as a function of number density for the QMC Skyrme interaction and (a) $T = 2$, (b) $T = 4$, and (c) $T = 6$ MeV. Left branch: pasta phase; Right branch: uniform matter. 96
4.26 Baryonic entropy density as a function of number density for the SkM* Skyrme interaction and (a) $T = 2$, (b) $T = 4$, and (c) $T = 6$ MeV. Left branch: pasta phase; Right branch: uniform matter. 97

4.27 Baryonic entropy density as a function of baryonic chemical potential for the NRAPR Skyrme interaction and (a) $T = 2$, (b) $T = 4$, and (c) $T = 6$ MeV. Left branch: uniform matter; Right branch: pasta phase. 98
4.28 Baryonic entropy density as a function of baryonic chemical potential for the SLy4 Skyrme interaction and (a) $T = 2$, (b) $T = 4$, and (c) $T = 6$ MeV. Left branch: uniform matter; Right branch: pasta phase. 99
4.29 Baryonic entropy density as a function of baryonic chemical potential for the QMC Skyrme interaction and (a) $T = 2$, (b) $T = 4$, and (c) $T = 6$ MeV. Left branch: uniform matter; Right branch: pasta phase. 100
4.30 Baryonic entropy density as a function of baryonic chemical potential for the SkM* Skyrme interaction and (a) $T = 2$, (b) $T = 4$, and (c) $T = 6$ MeV. Left branch: uniform matter; Right branch: pasta phase. 101

Chapter 1

Introduction

The complex structure of nuclear matter in the density region approaching $\rho_s \sim 0.16$ fm^{-3} (central density of heavy nuclei) at finite temperature ($T < 20$ MeV) critically affects many astrophysical and nuclear physics phenomena. These include the physics of neutron stars, the mechanism of core-collapse supernovae (CCSN) and the nucleosynthesis of heavy chemical elements in the Universe. Some nuclear physics properties of nuclear matter can be studied in terrestrial laboratories with new neutron-rich radioactive beams, and in relativistic heavy-ion collisions, in which similar densities and temperatures can be produced, but many aspects have to rely on theoretical models.

A major scientific effort is being carried out at an international level to study the properties of asymmetric nuclear systems experimentally and probe the behavior of the symmetry energy close to and above saturation density (Li et al., 2008). Astrophysical observations of compact objects also provide a window into both the bulk and the microscopic properties of nuclear matter at extreme isospin asymmetries (Steiner et al., 2005). Measurements coming from both laboratory and astrophysical observations are expected to put constraints on the acceptable properties of the Equation of State (EoS) of asymmetric nuclear matter (Lattimer and Prakash, 2007; Baran et al., 2005).

Correlations between different quantities in bulk matter and finite nuclei have been established. Examples are the correlation between the slope of the pressure of neutron matter at $\rho = 0.1$ fm^{-3} and the neutron skin thickness of ^{208}Pb (Brown, 2000; Typel and Brown, 2001) and the correlation between the crust-core transition density and the neutron skin thickness of ^{208}Pb (Horowitz and Piekarewicz, 2001). Both Skyrme forces and relativistic mean-field (RMF) models have been used to describe these correlations. Vidaña et al. (2009) analysed the correlation between the slope L and the curvature K_{sym} of the symmetry energy with the neutron skin thickness and the crust-core transition density in compact stars. It was shown that the parameters characterizing the microscopic Brueckner-Hartree-Fock (BHF) EoS of isospin asymmetric nuclear matter fall within the trends predicted by several Skyrme and relativistic effective models (Vidaña et al., 2009). These models are compatible with recent constraints coming from heavy-ion collisions (Li et al., 2008), giant monopole resonances (Garg et al., 2007), isobaric analogue states (Danielewicz and Lee, 2009) or meson production [pions (Li et al., 2005), kaons (Fuchs, 2006)] in heavy ion collisions.

Recently, Dutra et al. (2012) tested the capabilities of 240 Skyrme interaction parameter sets to provide good neutron-star properties. It was found that only 5 of these forces satisfied a series of criteria derived from macroscopic properties of nuclear matter in the vicinity of nuclear saturation density at zero temperature and their density dependence, from the liquid-drop model, in experiments with giant resonances and heavy-ion collisions, and from additional microscopic constraints on the density dependence of the neutron and proton effective mass β-equilibrium matter, from the Landau parameters of symmetric and pure neutron nuclear matter, and from observational data on high- and low-mass cold neutron stars (Dutra et al., 2012).

Tsang et al. (2012) have summarized the current status of experimental constraints on the symmetry energy below saturation density, its slope at the saturation density and on the neutron skin thickness of ^{208}Pb. They compared results from diverse experiments and claim there is a promising consensus from various experiments

using different experimental probes that shows the acceptable range of values of the symmetry energy and its slope to be centered around $(S_0, L) \sim 32.5, 70$ MeV. The current constraints are applicable to subnormal density, $(0.3\rho_0 \leq \rho \leq \rho_0)$ only and are somewhat dependent on the theoretical models used in the analysis of the experiments (Tsang et al., 2012).

The exploration of the Quantum Chromodynamics (QCD) phase diagram is not only a task for heavy-ion physics as there are strong relations to astrophysics of extremely dense matter and even to cosmology. The conditions in the early universe are similar to those probed by heavy-ion collisions at the Relativistic Heavy Ion Collider (RHIC) and the Large Hadron Collider (LHC); high temperatures and low net baryon densities. Supernova matter and neutron star matter are located in the QCD phase diagram at moderate temperatures and high net baryon densities. In this region of the QCD phase diagram, one expects to have a strong first-order phase transition which is related to the restoration of chiral symmetry (Sagert et al., 2009).

The GSI Facility for Antiproton and Ion Research (FAIR) at Darmstadt will soon allow more constraints for the high-density behavior of nuclear matter. A dedicated experiment for the investigation of the phase transition from hadronic matter to the quark-gluon plasma (QGP) in compressed baryon matter shall be hosted, which will study the phenomena of chiral symmetry restoration and quark (gluon) deconfinement accompanying the transition to the QGP (Klähn et al., 2006).

In this work we concentrate on CCSN, one of the most intriguing phenomena in the Universe. It includes a large variety of physics, from gravity to microscopic properties of atomic and subatomic particles. The key microscopic input into CCSN model simulations is the EoS, connecting the pressure of stellar matter to its energy density and temperature, which are, in turn, determined by its composition and modelling of interactions between its components. The composition of CCSN matter changes with increasing density and temperature. At low densities, an inhomogeneous phase exists, made up of discrete heavy nuclei immersed in a sea of single nucleons (predominantly neutrons), light nuclei (deuterium, tritium, helions, α-particles) and

electrons and potentially a degenerate gas of trapped neutrinos. At higher density and temperature, a homogeneous phase evolves, consisting of nucleons, leptons, heavy baryons, mesons and possibly quarks.

1.1 Core Collapse Supernovae

The most famous old supernova is that of 1054, recorded by the Chinese and Japanese and also mentioned in an Arab document, but not reported anywhere in Europe. Its remnant is the Crab Nebula, a tangle of brilliant filaments easily visible. At the center of the Crab, there is a neutron star, a pulsar, which emits electromagnetic radiation of all frequencies at regular intervals, about 30 pulses per second (Bethe, 1990).

Microscopically, core collapse supernovae result when the iron core of a massive star becomes unstable through a combination of electron capture and iron dissociation. Stars that have masses $M \geq 8M_{\odot}$ will eventually become super red giants. In the central region, the nuclear reactions will burn the composition to the ^{56}Fe end point (where fusion ceases to be exothermic), though the nuclear burning continues in the outer shells of Si, O, etc., causing the iron core to continue to grow. The gravity will crush the core to densities so high that the electrons will become relativistic and the stellar core will reach a limiting mass, the so-called *Chandrasekhar mass*: the maximum mass of an object supported by the pressure of the ultrarelativistic electrons (Chandrasekhar, 1931). The core pressure is initially dominated by electron degeneracy pressure. Once the Chandrasekhar mass is exceeded, the core begins to collapse, and inverse β-decay (e^- capture: $e^- + p \longrightarrow \nu_e + n$) accelerates the collapse. Once the density is larger than $\sim 10^{11}$ gm/cm^3 ($\sim 6.02 \times 10^{-5}$ fm^{-3}), the emitted neutrinos become trapped, because the time scale of the collapse is less than the diffusion time of the neutrinos. The inner part of the core, collapsing subsonically, transitions to bulk nuclear matter and becomes incompressible, substantially raising its pressure. The supersonically infalling material in the outer core rebounds from this stiffened inner core, sending an outward shock wave (Arnett, 1996). The shock

stalls before it can drive off the envelope of the star (see, e.g., Burrows and Lattimer (1985)). It is just at the final stage of the collapse, prior to the uniform nuclear matter, that the pasta phase, which is the focus of this Thesis, will appear. At the time the shock stalls, the core consists of an inner neutrinosphere radiating neutrinos and antineutrinos. The failure of this "prompt" supernova mechanism sets the stage for a delayed mechanism, wherein the intense neutrino flux, which is carrying off the 10^{53} erg binding energy of the newly formed proto-neutron star (PNS), heats matter above the neutrinospheres and reenergizes the shock (Wilson, 1985; Bethe and Wilson, 1985). Under this neutrino reheating paradigm, the shock remains an accretion shock until sufficiently reenergized to overcome the gravity of the PNS and the ram pressure of the infalling matter, whereupon it propagates outward, heating and transmuting the overlying layers and ejecting the envelope. The released binding energy (10^{53} ergs) of the newly formed PNS heats the matter to temperatures up to $T \sim 50$ MeV (Burrows and Lattimer, 1986). This star will cool essentially by neutrino emission. Revival of the stalled shock above the neutrinosphere is mediated by the absorption of electron neutrinos and antineutrinos emerging from the radiating PNS. This heating depends sensitively on the neutrino luminosities, spectra and distribution in the region behind the shock. Ultimately, this supernova shock wave must propagate out of the iron core and through the star's outer layers to disrupt the star in a core collapse supernova explosion (Mezzacappa and Bruenn, 2000; Mezzacappa and Messer, 1999). The process going on in the extremely dense and hot core of the exploding star is accessible to direct measurements only through neutrinos or gravitational waves (Janka et al., 2001).

There is no doubt that the supernova phenomenon exists in nature and is accompanied by an explosion. Models have frequently failed to reproduce this explosion in a credible way. Spherically symmetric models for the neutrino reheating paradigm have generally failed to produce explosions because they do not deliver sufficient energy to the envelope as a result of the stratification imposed by spherical symmetry (see, e.g., Bruenn (1985); Wilson and Mayle (1993); Bruenn et al. (2001)).

Because the neutrino energy deposition behind the shock depends sensitively not only on the neutrino luminosities (Burrows and Goshy, 1993; Janka, 2001) and spectra (Swesty, 1998), but also on the neutrino angular distributions, spherically symmetric simulations implementing spectral Boltzmann neutrino transport were developed (Mezzacappa and Messer, 1999; Liebendörfer et al., 2004). Despite this improvement, these models also fail to explode (Liebendörfer et al., 2001; Rampp and Janka, 2002; Thompson et al., 2003).

Models that break the assumption of spherical symmetry have achieved greater success, either by enhancement of the neutrino luminosity due to fluid instabilities within the PNS (Wilson and Mayle, 1993; Keil et al., 1996), or by enhanced efficiency of the neutrino heating due to large scale convection behind the shock (see, e.g., Herant et al. (1994); Burrows et al. (1995)). PNS instabilities are driven by lepton and entropy gradients, while convection behind the shock originates from gradients in entropy that are born from the stalling of the shock and grow as the matter is heated from below. While some 2D gray transport models, where average neutrino energies are used for computing the transport, do produce explosions (including Herant et al. (1994) and Burrows et al. (1995)), even with such convective enhancements, explosions are not guaranteed (Janka and Müller, 1996; Mezzacappa et al., 1998a,b). Fryer and Warren (2002, 2004) have demonstrated that three-dimensional models exhibit large scale convective behavior similar to these two-dimensional models, a surprising result likely explained by the nature of the hydrodynamic instability of the stalled accretion shock, termed the SASI (Blondin et al., 2003; Blondin and Mezzacappa, 2006). This instability to non-radial perturbations favor low order modes, ultimately leading to gross distortions of the shock. Recent simulations using spectral neutrino transport, including Bruenn et al. (2006, 2009), Marek and Janka (2009) and Mueller et al. (2012), exhibit successful neutrino-driven explosions in 2D for a range of progenitors. The essential difference between the current exploding models (Bruenn et al., 2009; Marek and Janka, 2009) and similar models of earlier in the decade (e.g. Buras et al. (2003, 2006)), which produced at best weak

explosions for low mass progenitors, is the opening of the computational domain from 90° in latitude to 180°, allowing the SASI to excite the lowest order modes which work to push the shock outward gradually over several hundred milliseconds. This allows increased neutrino heating to ultimately re-invigorate the shock and drive an explosion. In contrast, Burrows et al. (2006, 2007) have reported successful explosions in which the shock is revived not by neutrino re-heating, which is insufficient in their simulations, but by acoustic waves excited by the SASI-induced aspherical accretion stream onto the PNS. The existence of competing core-collapse supernova mechanisms highlights the need for deeper investigation and ultimately comparison with observations. However, one common feature of all of these recent models is a several hundred millisecond delay between core bounce and explosion, which directly impacts the nucleosynthesis and other observables (Hix, 2013; Janka, 2012).

Lentz et al. (2012) have conducted a series of numerical experiments using spherically symmetric, general relativistic, neutrino radiation hydrodynamics with the code Agile-BOLTZTRAN to examine the effects of modern neutrino opacities on the development of supernova simulations. They tested the effects of opacities by removing opacities or by undoing opacity improvements for individual opacities and groups of opacities and they found that improvements to electron capture (EC) on nuclei, namely EC on an ensemble of nuclei using modern nuclear structure models rather than the simpler independent-particle approximation (IPA) for EC on a mean nucleus, plays the most important role during core collapse of all tested neutrino opacities.

Another possible solution to the CCSN problem may lay in the improvement of the EoS, since the EoS at subnuclear densities controls the rate of collapse, the amount of de-leptonization and thus the size of the collapsing core and the bounce density. Also, any phase transition of the collapsing matter will absorb heat, disrupt the homology, and so weaken the subsequent shock (Williams and Koonin, 1985). It is therefore very important to determine the EoS as accurately as possible.

During the supernova collapse and the birth of a PNS, modern simulations indicate that matter can reach temperatures up to 20 MeV and the density at bounce of the collapsing core goes up to $1.5-2.0\rho_0$. The timescale for supernova collapse is believed to be of order of seconds and matter does not have enough time to reach β-equilibrium throughout the rapid changes (Stone and Reinhard, 2007). Thus the calculation of the EoS has to be performed for a range in ratio of neutrons and protons, usually $y_p \sim 0.3$, for densities where nuclear matter forms (Mezzacappa, 2005).

1.2 The Pasta Phase

One of the most intriguing phases of CCSN matter is the transitional region between the inhomogeneous and homogeneous phases. In addition to its intrinsic interest, this sub-saturation density regime exists briefly in a collapsing stellar core during the formation of a core-collapse supernova (Brown et al., 1982; Bethe et al., 1980, 1979), and the strength — or even existence — of the subsequent shock wave depends sensitively upon the EoS (Williams and Koonin, 1985). As the density and temperature increase, heavy quasi-nuclei structures are formed which undergo a series of changes from spherical to exotic forms: rods, slabs, cylindrical holes and bubbles, termed "nuclear pasta" (Ravenhall et al., 1983) (see Fig 1.1). This is an extension of the trend toward heavier, more neutron-rich nuclei that occurs during earlier phases of core collapse. This process is mainly caused by the competition between surface tension and the Coulomb repulsion of closely spaced heavy nuclei and occurs not only in CCSN matter but, for example, also at the transitional region between the crust and core of neutron stars (Ravenhall et al., 1983; Horowitz et al., 2004b, 2005; Maruyama et al., 2005; Watanabe et al., 2005; Sonoda et al., 2008, 2010).

The pasta phase appears at densities of the order of $0.001 - 0.1$ fm^{-3} (Sonoda et al., 2008, 2010; Avancini et al., 2008). The ground-state configuration is the one that minimizes the free energy, i.e., the pasta phase is the ground-state configuration

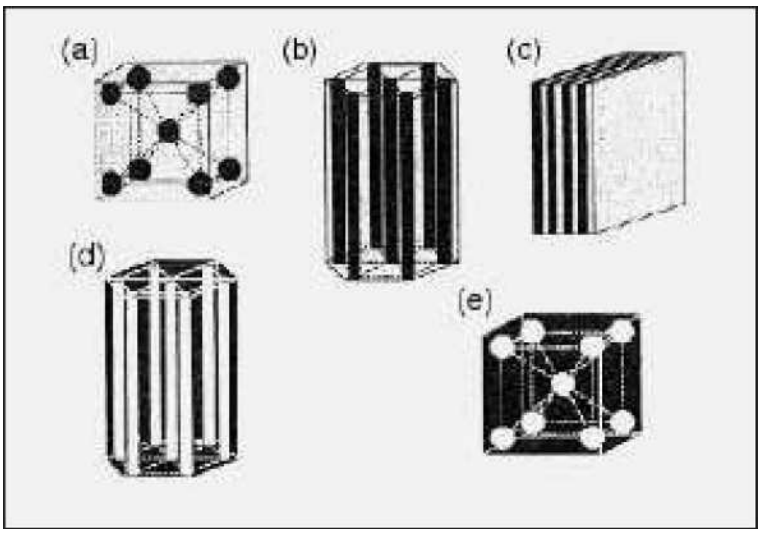

Figure 1.1: Nuclear Pasta: (a) spherical (gnocchi); (b) rod (spaghetti);(c) slab (lasagna); (d) tube (penne); (e) bubble (swiss cheese?) $\rightarrow$ uniform matter.

if its free energy per particle is lower than the one corresponding to the homogeneous phase at the same density (Avancini et al., 2010).

The pasta phase of matter has been studied under different assumptions in order to more precisely describe the physics involved in this phenomenon. There is currently considerable interest in searching for a better description of nuclear matter under exotic conditions (namely of density, temperature and asymmetry). Both spherical (1D) and asymmetric (3D) models were developed to study the pasta phase in hot CCSN and cold neutron star matter.

The basic properties of the pasta phase were first computed by Ravenhall et al. (1983) using semiclassical liquid drop models or Thomas-Fermi methods and later by Lamb et al. (1983); Lattimer and Swesty (1991); Lassaut et al. (1987). The energetically preferred pasta formation was obtained by calculating the energy densities of the separate formations (including that of uniform matter) across the whole density and temperature regime in which pasta was expected to exist, selecting the formation that gave the lowest energy density at a given baryon number density. This required that the nuclear shapes expected to appear had to be specified *a priori* (Newton and Stone, 2009).

Fully microscopic 1D Hartree-Fock (HF) calculations of supernova matter were carried out by Bonche and Vautherin (1981, 1982). They used the spherical Wigner-Seitz (WS) approximation, in which the generally nonspherical unit cell is replaced by a spherical one with the same volume. The WS approximation is good as long as the nuclear structures that form the lattice points are sufficiently widely spaced. This condition is satisfied everywhere except close to the transition density, when their spacing becomes comparable with their individual physical extent (Newton and Stone, 2009). To treat the transition to uniform matter correctly, 3D models are necessary which go beyond the WS approximation and use cubic (or higher order symmetry) unit cells.

The 3D Skyrme-Hartree-Fock (3D-SHF) method in a cubic box with the SLy4 Skyrme parametrization was applied to neutron star matter by Magierski and Heenen (2002) at zero temperature and, using RMF models, by Gögelein et al. (2008) at finite temperature.

Both 3D studies to date calculated nuclear configurations at a limited number of values of densities and number of nucleons in the unit cell, and only for proton fractions expected to be found in neutron star crustal matter. Only Gögelein and Müther performed calculations at finite temperature. To self-consistently probe the energy of various pasta shapes, both independent quadrupole moments (q_{20} and q_{22}) of the nucleon distribution in the unit cell should be constrained. The study of Magierski and Heenen imposed a constraint only on the q_{20} component of the proton quadrupole moment, whereas Gögelein and Müther performed unconstrained calculations (Newton and Stone, 2009).

For completeness, we mention the work of Avancini et al. (2008, 2009, 2010) who explored the creation and forms of the pasta structures in the framework of the non-linear Walecka model with a variety of effective Lagrangians. The calculation was done at zero and finite temperature using the Thomas-Fermi approximation. They found some dependence of the onset of pasta on the choice of the Lagrangian and

details of the models used. Although these results depend on the use of the Thomas-Fermi approximation, it will be interesting to compare them to our findings.

We also mention the work of Williams and Koonin (1985), who took the energy per nucleon to be the Thomas-Fermi approximation to the Skyrme III functional and include the Coulomb energy to study the zero-temperature EoS of isospin-symmetric ($y_p = 0.5$) nuclear matter below saturation density by minimizing the energy of the nucleons in a periodic cubic cell at each mean density. They found several phase transitions between different topologies of matter, going from spheres to rods to slabs to tubes to bubbles with increasing density, and discussed their implications in a CCSN framework (Williams and Koonin, 1985).

To date, in the EoS used in CCSN simulations (Lattimer and Swesty, 1991; Shen et al., 1998), the transition to homogeneous matter has been treated empirically, as the homogeneous and inhomogeneous phases have been described by two different parametrizations of the EoS. The pasta phase is schematically included in the Lattimer-Swesty EoS (Lattimer and Swesty, 1991) and the EoS for CCSN simulations (Shen et al., 2010a,b, 2011a,b) based on RMF models and the virial EoS does not include the pasta phase fully in 3D, even though according to some estimates, it may form up to 20% of the supernova matter at bounce (Sonoda et al., 2007).

An alternative approach to modelling the pasta regime is the techniques of quantum molecular dynamics (QMD) and related methods (Maruyama et al., 1998). This semiclassical microscopic treatment, in which a large number of nucleons is dynamically evolved in a large cubic box with periodic boundary conditions without assumptions on the quasi-nuclear structure produced, offers a computationally manageable model, but lacks important theoretical details of nuclear structure physics. For computationally efficiency, the effective nucleon-nucleon interaction is very schematic and, among other simplifications, the important shell effects are missing. The pasta shapes themselves and their sequence have been studied in detail using QMD at zero and finite temperature (Watanabe et al., 2001; Watanabe and Sonoda, 2005). The dynamical response of the pasta to a neutrino flux through the

matter has also been investigated in this framework (Horowitz et al., 2004b,a), and significant strength at low energies from excitations of the internal degrees of freedom of the pasta has been found.

Dorso et al. (2012) used the classical molecular dynamics (CMD) technique based on the work of Pandharipande (Vicentini et al., 1985; Lenk and Pandharipande, 1986; Lenk et al., 1990), where they found a plethora of nuclear shapes. CMD treats nucleons as classical particles interacting through a two-body potential and solves the coupled equations of motion of the many-body system to obtain the time evolution of all particles. Since the $(\mathbf{r}, \mathbf{p})$ information is known for all particles at all times, it is possible to know the structure of the nuclear medium from a microscopic point of view (Dorso et al., 2012).

In addition to pasta formation, other processes, such as development of light clusters in the vicinity of the phase transition and dynamical instabilities of matter in the region were studied both in the non-relativistic (Chomaz et al., 2004; Kolomietz and Shlomo, 2004) and relativistic (Providência et al., 2006a; Brito et al., 2006) framework. It has been suggested that the existence of an inhomogeneous pasta phase is intrinsically related to the appearance of collective unstable modes in the matter (Providência et al., 2006b).

This work follows the one by Newton and Stone (Newton and Stone, 2009; Newton, 2008), where the pasta phase at the density region below ρ_s, and its transition to the liquid uniform phase has been studied in the framework of the first fully self-consistent, non-relativistic 3D-SHF model of "pasta" phase at finite temperature, allowing for a wide variety of possible nuclear formations, calculated self-consistently without a need for pre-determination of the shape as input. Another advantage of our model is the self-consistent calculation of the transition between inhomogeneous and homogeneous matter without a need for two separate EoS.

The main goals of this work are the self-consistent calculation of the nuclear pasta phase and the determination of the phase transition between pasta and uniform matter and its character. We use a finite temperature 3D-Hartree-Fock method with

several models for the effective density-dependent Skyrme interaction at an extended grid of ρ, T and $y_p = 0.3$ to cover the model space where the pasta phase is expected to appear. The dependence of the outcome of the 3D-SHF model on the choice of the effective nucleon-nucleon interaction has not been studied as yet in 3D-SHF models. We selected four different interactions, SkM* (Bartel et al., 1982), SLy4 (Chabanat et al., 1998), NRAPR (Steiner et al., 2005) and SQMC700 (Guichon et al., 2006), based on their overall performance in modelling of a wide variety of nuclear matter properties (Dutra et al., 2012), to examine the sensitivity of the pasta formation and, in particular, the conditions and nature of the phase transition.

A key interest in the pasta phase in CCSN is that the neutrino opacity, which plays the central role in the development of a shock wave during the supernova collapse, is affected by its presence (Sonoda et al., 2007). Horowitz et al. (2004b,a) studied these effects using the QMD technique but did not get a conclusive answer because they did not reproduce all the classical pasta shapes in their model. Sonoda et al. (2007) showed how pasta phases affect the neutrino transport cross section via weak neutral current using several nuclear models. They calculated neutrino opacity of the phases with rod-like and slab-like nuclei taking into account finite temperature effects, using the QMD approach. They found that pasta phases affect the energy-dependent cross sections for coherent scattering of neutrinos in collapsing cores. Once our study of the shapes and range of occurrence of nuclear pasta is complete, we plan to investigate the impacts of our pasta on neutrino opacities.

1.3 The phase transition

The equilibrium state of a homogeneous body is determined by specifying any two thermodynamic quantities, for example the volume V and the energy E. There is, however, no reason to suppose that for every given pair of values of V and E, the state of the body corresponding to thermal equilibrium will be homogeneous. It may be that for a given volume and energy in thermal equilibrium the body is not homogeneous,

but separates into two homogeneous parts in contact that are in different states. Such states of matter that can exist simultaneously in equilibrium with one another and in contact are described as different phases (Landau and Lifshitz, 1980). Let us write down the conditions for equilibrium between two phases. First of all, as for any bodies in equilibrium, the temperatures T_1 and T_2 of the two phases must be equal:

$$T_1 = T_2.$$

The pressures in the two phases must also be equal:

$$P_1 = P_2,$$

since the forces exerted by the two phases on each other at their surface of contact must be equal and opposite. Finally, the chemical potentials of the two phases must be equal:

$$\mu_1 = \mu_2.$$

If the potentials are expressed as functions of pressure and temperature, and the common temperature and pressure are denoted by T and P, we have

$$\mu_1(P, T) = \mu_2(P, T).$$

Thus two phases can not be in equilibrium with each other at all pressures and temperatures; when one of these is given, the other is completely determined (Landau and Lifshitz, 1980). These thermal, mechanical and chemical equilibrium relations are called the Gibbs conditions. This occurs, for example, in equilibrium between a gas and the liquid, where we have a first order phase transition. It is remarkable that neither the density of the liquid (given by N_l/V_l) nor the density of the gas (given by N_g/V_g) changes during this phase transition (Greiner et al., 1997).

1.3.1 First and second order phase transitions

Phase transitions which are connected with an entropy discontinuity are called discontinuous or phase transitions of first order. On the other hand, phase transitions where the entropy is continuous are called continuous or of second or higher order.

For a first-order phase transition, at least one of the first derivatives of the free energy with respect to one of its variables is discontinuous (Greiner et al., 1997): $S = -\frac{\partial F}{\partial T}|_{N,V,...}$ $P = -\frac{\partial F}{\partial V}|_{N,T,...}$ This discontinuity produces a divergence in the higher derivatives like the specific heat $C_V = T\frac{\partial S}{\partial T}|_V = -T\frac{\partial^2 F}{\partial^2 T}|_V$, or the incompressibility $K(\rho_0) = 9\rho_0^2\frac{\partial^2 E_{SNM}(\rho)}{\partial^2 \rho}|_{\rho=\rho_0}$, where E_{SNM} is the energy per particle of symmetric nuclear matter (Vidaña et al., 2009).

For a phase transition of second (or nth order), the first derivatives of the free energy are continuous; however, second (or nth order) derivatives, like the specific heat or the susceptibility, are discontinuous or divergent. The transition to superconductivity without an external magnetic field is an example of phase transitions of this kind (Greiner et al., 1997).

First-order phase transitions in single-component systems are characterized by discontinuities in certain physical quantities. This occurs because quantities like the density and the entropy are different in the two distinct phases, but the pressure and chemical potential remain constant. This behavior does not occur in a binary system, because the constraints of charge conservation and Gibbs' criteria force the density (and pressure) in each individual phase to change throughout the transition. We might therefore expect the transition in the binary system to be smoother (Müller and Serot, 1995).

Müller and Serot (1995) analysed the liquid-gas phase transition in a system with two conserved charges (baryon number and isospin) using the stability conditions on the free energy, the conservation laws, and Gibbs criteria for phase equilibrium in the framework of a RMF model of nuclear matter with arbitrary proton fraction at finite temperature. They concluded that in general, the pressure, temperature, density, and

concentration of both the gas and liquid phase can vary throughout the transition. Moreover, both the Gibbs free energy and entropy are continuous throughout the transition, showing that it is second order rather than first-order, as in familiar one-component systems. They then applied their model to the liquid-gas phase transition that may occur in the warm, dilute matter produced in energetic heavy-ion collisions and, if such a phase transition actually occurs, then generically it should be smoother than a first-order phase transition.

Raduta and Gulminelli (2010) developed a phenomenological statistical model for dilute star matter, in which free nucleons are treated within a mean-field approximation and nuclei are considered to form a loosely interacting cluster gas, with $T = 1 - 20$ MeV, $y_p = 0 - 0.5$ and $\rho > 10^8$ g/cm^3 ($\rho >\sim 6.02\times^{-8}$ fm $^{-3}$), making it appropriate for CCSN and PNS description. They found that, contrary to the common belief, the crust-core transition is not first order, and for all subsaturation densities matter can be viewed as a continuous fluid mixture between free nucleons and massive nuclei. As a consequence, the equations of state and the associated observables do not present any discontinuity over the whole thermodynamic range.

Our study reveals a discontinuity in the pressure, chemical potential and entropy (see chapter 4), making the phase transition in our system a first-order one.

1.3.2 The critical point

The phase equilibrium curve (in the PT-plane) may terminate at a certain point, called the critical point; the corresponding temperature and pressure are the critical temperature (T_c) and the critical pressure (P_c). At temperatures above T_c and pressures higher than P_c, no difference of phases exists, the substance is always homogeneous, and we can say that at the critical point the two phases become identical (Landau and Lifshitz, 1980; Müller and Serot, 1995). For a binary system with two phases, the phase-separation boundary, is called binodal. Therefore the critical points form a line that divides the binodal surface into different regions

describing either a high density (liquid) or a low density (gas) phase (Müller and Serot, 1995).

1.3.3 Order parameter

To describe quantitatively the change in the structure of the body when it passes through the phase transition point, we can define the order parameter (η) in such a way that it takes non-zero (positive or negative) values in the unsymmetrical phase and is zero in the symmetrical phase (Landau and Lifshitz, 1980). For instance, in transitions where the atoms are displaced from their positions in the symmetrical phase, η may be taken as the amount of this displacement. For transitions with a change in the ordering of the crystal (e.g. in the CuZn alloy), the parameter η may be defined as $\eta = (\omega_{Cu} - \omega_{Zn})/(\omega_{Cu} + \omega_{Zn})$, where ω_{Cu} and ω_{Zn} are the probabilities of finding a copper atom and a zinc atom respectively at any given lattice site (Landau and Lifshitz, 1980). It must again be emphasised that the symmetry of the body is changed only when η becomes exactly zero. Any non-zero value of the order parameter, however small, brings about a lowering of the symmetry. A passage through a phase transition point of the second kind has a continuous change of η to zero. The absence of any discontinuous change of state at a phase transition point of the second kind has the result that the thermodynamic functions of the state of the body (its entropy, energy, volume, etc.) vary continuously as the transition point is passed (Landau and Lifshitz, 1980).

This order parameter should represent the main qualitative difference between the various phases. This means in particular that it should vanish for the liquid-gas phase transition at the critical point, since then a distinction between these phases is no longer possible. In this case, the density difference $\delta\rho = \rho_l - \rho_g \equiv \eta$ would be a suitable order parameter, as well as (for fixed particle number) the volume difference

$V_g - V_l$ or the entropy difference. It is often difficult to find a suitable order parameter for a certain phase transition (Greiner et al., 1997).

In Chapter 2, we briefly describe the formalism used and in Chapter 3, the numerical method is explained. In Chapter 4, we present and discuss the results obtained and, finally, in Chapter 5, some conclusions are drawn.

Chapter 2

Nuclear Forces

The force that binds protons and neutrons together in the nucleus, despite the electrical repulsion of the protons, is an example of the strong interaction. In the context of nuclear structure, this interaction is called the nuclear force. It does not depend on charge: neutrons, as well as protons, are bound, and the binding is the same for both. It has short range, of the order of nuclear dimensions — that is, 10^{-15}m. But within its range, the nuclear force is much stronger than electrical forces; otherwise, the nucleus could never be stable. It would be nice if we could write a simple equation like Newton's law of gravitation or Coulomb's law for this force, but physicists have yet to fully determine its dependence on the separation r. The nearly constant density of nuclear matter and the nearly constant binding energy per nucleon of larger nuclides show that a particular nucleon cannot interact simultaneously with all the other nucleons in a nucleus, but only with those few in its immediate vicinity. This is different from electrical forces; every proton in the nucleus repels every other one. This limited number of interactions is called saturation; it is analogous to covalent bonding in molecules and solids. Finally, the nuclear force favours binding of pairs of protons or neutrons with opposite spins. Hence the α particle (two protons and two neutrons) is an exceptionally stable nucleus for its mass number (Young and Freedman, 2008).

The lack of exact knowledge of the nuclear force makes modelling of properties of infinite nuclear matter and finite nuclei difficult. One of the main challenges is to correctly describe the modification of the bare two-body nucleon-nucleon interaction, extracted from nucleon-nucleon scattering experiments and the properties of the deuteron in nuclear medium. The nuclear many-body problem cannot be solved exactly at present and approximative approaches are needed.

2.1 Microscopic Models

Microscopic models are models that describe the structure of the nucleus in terms of the degrees of freedom of its microscopic constituents — the nucleons. To do this a microscopic Hamiltonian H is needed, which contains some suitable form of nucleon-nucleon interaction. Most of these models start from a nonrelativistic Hamiltonian containing only two-body interactions (Greiner and Maruhn, 1996).

The most natural selection for the degrees of freedom to use in the wave functions is, of course, the nucleonic ones, i.e., the sets of positions r_i, spins s_i, and isospins τ_i, for a nucleus with A nucleons. The wave function then takes the general form

$$\psi(r_1, s_1, \tau_1, r_2, s_2, \tau_2, ..., r_A, s_A, \tau_A), \tag{2.1}$$

while for the Hamiltonian we would try the natural expression

$$\hat{H} = -\sum_{i=1}^{A} \frac{\hbar^2}{2m}\nabla^2 + \frac{1}{2}\sum_{i,j} V(i,j). \tag{2.2}$$

Here $V(i,j)$ is the nucleon-nucleon interaction, which may depend on all the degrees of freedom of a pair of nucleons. It is impractical, even with modern computers, to solve the many-particle Schrödinger equation directly for A larger than of order ten, so that the search for suitable approximations is the overriding concern in this type of model. It is one of the important features of nuclear theory that there is

no *a priori* theory for $V(i,j)$. Instead, various parametrizations are employed that are good for different purposes — one may be adapted for describing nucleon-nucleon scattering while another may be suitable for Hartree-Fock calculations of heavy nuclei. It is not even clear how important three-body forces not included in the Hamiltonian of equation (2.2) might be. Until the nucleon-nucleon interaction can be derived from a more fundamental theory such as quantum chromodynamics, we will have to tolerate this situation. Contrast this with the situation in atomic physics, where the fundamental interaction theory — QED — is very well known and it is only a matter of approximation methods to find solutions to the problem. A typical microscopic model depends on a nucleon-nucleon interaction which necessarily contains parameters fitted to reproduce some experimental data. This justifies the name model even for the microscopic approaches: the absence of knowledge about the fundamental interaction is replaced by the proposal of a reasonable functional form with a limited number of parameters, which cannot be determined from an underlying theory (Greiner and Maruhn, 1996).

All microscopic models of the nucleus are based on some model of the basic interactions between nucleons. Attempts to derive the nucleon-nucleon interaction from the quark model are not sufficiently mature to be used in nuclear models, so that there is still a plethora of model interactions that are used for various purposes (Greiner and Maruhn, 1996).

It seems that in nuclei the interaction is modified by complicated many-body effects to such an extent that it becomes more profitable to employ effective interactions, which do not describe nucleon-nucleon scattering well but are thought to include many of the effects of many-body correlations and should strictly be used only in Hartree-Fock and similar nuclear structure calculations, not for nucleon-nucleon scattering. In principle they may be valid only inside a certain space of shell-model states. Often the functional form of such an interaction is selected with a view to ease of computation (Greiner and Maruhn, 1996).

Bare nuclear forces are not suited for direct use in the nuclear medium, mainly because they are not density-dependent. They show strong repulsion at short distances (hard core). Taking these bare nucleon-nucleon (NN) interactions as input into many-body formalism such as relativistic Dirac-Bruckner-Hartree-Fock approximation (ter Haar and Malfliet, 1987; van Dalen et al., 2004; de Jong and Lenske, 1998) and its non-relativistic counterpart BHF (Cugnon et al., 1987; Zuo et al., 2002; Bombaci and Lombardo, 1991; Day and Wiringa, 1985; Baldo et al., 2000; Vidaña et al., 2000), variational method (Akmal et al., 1998; Mukherjee and Pandharipande, 2007), Correlated Basis Function (Fabricioni and Fantoni, 1993; Bisconti et al., 2006), Self-Consistent Greens Fuction models (SCGF) (Dewulf et al., 2003; Frick and Müther, 2003), Quantum Monte Carlo techniques (Pudliner et al., 1997; Schmidt and Fantoni, 1999; Carlson et al., 2003; Gandolfi et al., 2007, 2008, 2009), and Chiral Effective Field Theory (Hebeler and Schwenk, 2010; Hebeler et al., 2010), an effective NN interaction is derived, which includes the effect of the medium, and the many-body problem approximately solved (Dutra et al., 2012).

2.2 Phenomenological Effective Interactions

To avoid problems with modification of the bare nucleon-nucleon interaction in the nuclear medium, another approach may be advantageous. It is possible to define an effective density-dependent nucleon-nucleon interaction, fit its parameters to ground state observables of finite nuclei and saturation properties of symmetric nuclear matter and use it directly in Hartree-Fock or related techniques to find an approximate solution of the nuclear many-body problem, at least for ground states. The pioneering models of Köhler (1965a,b), Brink and Boeker (1967), Moszkowski (1970), Skyrme (1956), further developed by Vautherin and Brink (1972) (and references therein) and Decharge and Gogny (1980) initiated this approach, which is used today. The basic idea is to parametrize the 2- and 3-body interactions by zero range (Skyrme model), short finite range (Gogny model) and indefinitive range (Separable Monopole model

(SMO) (Stevenson et al., 2001; Stone et al., 2002)) density-dependent functionals to describe the ground state properties of finite nuclei and nuclear matter. In this scenario, the microscopic details of 2- and 3-body forces, such as meson exchange, are not explicitly considered and all the physically relevant information is carried by the parameters of the density-dependent phenomenological forces which include the spin, orbital angular momentum and isospin couplings. The drawback of this approach is that the parametrization of such forces is not unique and there exist, in principle, an infinite number of parameter sets, fitted to ground state properties of (doubly- or semi-magic) stable nuclei, fission barriers, energies of giant resonances and symmetric and asymmetric nuclear matter (Dutra et al., 2012). The most wide-used examples of such effective interactions are the Skyrme and Gogny forces. The Skyrme force has been adopted in this work and will be described in detail below.

2.2.1 The Skyrme Interaction

In 1956 Skyrme (Skyrme, 1956) proposed an effective interaction with a three-body term:

$$V = \sum_{i<j} V(i,j) + \sum_{i<j<k} V(i,j,k). \tag{2.3}$$

To simplify the calculations, he used a short-range expansion for the two-body part:

$$\begin{aligned} V(1,2) &= t_0(1+x_0P^\sigma)\delta(\mathbf{r}_1-\mathbf{r}_2) \\ &+ \frac{1}{2}t_1[\delta(\mathbf{r}_1-\mathbf{r}_2)\mathbf{k}^2+\mathbf{k}^2\delta(\mathbf{r}_1-\mathbf{r}_2)] + t_2\mathbf{k}\delta(\mathbf{r}_1-\mathbf{r}_2)\mathbf{k} \\ &+ iW_0(\sigma^{(1)}+\sigma^{(2)})\mathbf{k}\times\delta(\mathbf{r}_1-\mathbf{r}_2)\mathbf{k}, \end{aligned} \tag{2.4}$$

where $\mathbf{k} = (1/\hbar)\mathbf{p}$ is the operator of the relative momentum

$$\mathbf{k} = \frac{1}{2i}(\nabla_1 - \nabla_2). \tag{2.5}$$

For the three-body force, Skyrme also assumed a zero range force of the form:

$$V(1,2,3) = t_3\delta(\mathbf{r}_1 - \mathbf{r}_2)\delta(\mathbf{r}_2 - \mathbf{r}_3). \tag{2.6}$$

The six constants, t_0, t_1, t_2, t_3, x_0 and W_0 were adjusted to the experimental binding energies and radii of closed shell nuclei. The parameter t_0 describes a pure δ-force with a spin-exchange, t_1 and t_2 simulate an effective range, and t_3 the density-dependent term. The W_0 term in (2.4) represents a two-body spin orbit interaction. For spin saturated even-even nuclei, the three-body term (2.6) turns out to be equivalent to a density-dependent two-body interaction:

$$V_n(1,2) = \frac{1}{6}t_3(1 + P^\sigma)\delta(\mathbf{r}_1 - \mathbf{r}_2)n(\frac{1}{2}(\mathbf{r}_1 + \mathbf{r}_2)). \tag{2.7}$$

Such a density-dependent term can also be regarded as the phenomenological representation of the n-dependence of the microscopic effective interaction (Ring and Schuck, 1980). Therefore, the Skyrme interaction takes the form of an effective two-body potential between particles i and j. Its form is based on an expansion of the matrix elements of a two-body potential in momentum space up to second order and we can rewrite it as:

$$\begin{aligned}
\hat{v}_{skyrme}(\mathbf{r}_i, \mathbf{r}_j) &= t_0(1 + x_0P_\sigma)\delta(\mathbf{r}_i - \mathbf{r}_j) \\
&+ \frac{1}{2}t_1(1 + x_1P_\sigma)[\mathbf{k}_{ij}^2\delta(\mathbf{r}_i - \mathbf{r}_j) + \delta(\mathbf{r}_i - \mathbf{r}_j)\mathbf{k}_{ij}^2] \\
&+ t_2(1 + x_2P_\sigma)\mathbf{k}_{ij}.\delta(\mathbf{r}_i - \mathbf{r}_j)\mathbf{k}_{ij} \\
&+ \frac{1}{6}t_3(1 + x_3P_\sigma)n^\alpha(\bar{\mathbf{r}})\delta(\mathbf{r}_i - \mathbf{r}_j) \\
&+ it_4\mathbf{k}_{ij}\delta(\mathbf{r}_i - \mathbf{r}_j)(\hat{\sigma}_i + \hat{\sigma}_j) \times \mathbf{k}_{ij},
\end{aligned} \tag{2.8}$$

where n is the matter density, $\mathbf{k}_{ij} \equiv -\frac{1}{2}i(\nabla_i - \nabla_j)$ is the relative wavevector, $P_\sigma = \frac{1}{2}(1 + \hat{\sigma}_i.\hat{\sigma}_j)$ is the spin exchange operator, $\hat{\sigma}$ is the vector of Pauli spin matrices and $\bar{\mathbf{r}} = (\mathbf{r}_i + \mathbf{r}_j)/2$. This form of the Skyrme potential is an example of a parametrization

through $t_0, t_1, t_2, t_3, t_4, x_0, x_1, x_2, x_3$ and α, introduced to describe nuclear properties more accurately.

The term $t_0(1 + x_0P_\sigma)\delta(\mathbf{r}_i - \mathbf{r}_j)$ represents a s-wave (zero relative angular momentum) interaction. The x_0 term additionally exchanges the spin of the particles. The second term $\frac{1}{2}t_1(1 + x_1P_\sigma)[\mathbf{k}_{ij}^2\delta(\mathbf{r}_i - \mathbf{r}_j) + \delta(\mathbf{r}_i - \mathbf{r}_j)\mathbf{k}_{ij}^2]$ is also a s-wave, but this interaction includes a dependence on the relative linear momentum of the particles. The third term $t_2(1 + x_2P_\sigma)\mathbf{k}_{ij}.\delta(\mathbf{r}_i - \mathbf{r}_j)\mathbf{k}_{ij}$ is a p-wave (unit relative angular momentum) interaction, including spin exchange as in the first term. The fourth term $\frac{1}{6}t_3(1+x_3P_\sigma)n^\alpha(\bar{\mathbf{r}})\delta(\mathbf{r}_i-\mathbf{r}_j)$ is a density-dependent interaction: this term can be thought of as the three-body force with one of the coordinates integrated out. The parameter α is added to this term to soften the density-dependence which could otherwise lead to too high a compressibility for nuclear matter. Finally, $it_4\mathbf{k}_{ij}\delta(\mathbf{r}_i - \mathbf{r}_j)(\hat{\sigma}_i + \hat{\sigma}_j) \times \mathbf{k}_{ij}$ is the spin-orbit force (Newton, 2008).

There are essentially three reasons why this force has gained so much importance over the years. First, Vautherin and Brink (1972) were able to reproduce the nuclear binding energies over the whole periodic table with a reasonable set of parameters and, at the same time, the nuclear radii. Second, Negele and Vautherin (1973) gave the connection between this force and the more fundamental G-matrix (Brueckner, 1955; Day, 1967). Finally, the mathematical form of the force is extremely simple. The δ-functions simplify all types of calculations enormously (Ring and Schuck, 1980).

The Skyrme potential may be rewritten as an energy-density functional ϵ_{Skyrme} as follows (Chabanat et al., 1997)

$$\varepsilon_{Skyrme}[\Phi] =< \Phi|(\hat{T} + \hat{V}_{Skyrme})|\Phi >= \int d^3r\epsilon_{Skyrme}, \tag{2.9}$$

where $\hat{T} = \sum_{i=1}^{N}\hat{t}_i(\mathbf{r}_i)$ is the total kinetic energy operator, summed over the single particle kinetic energy operators t_i, and $\hat{V}_{Skyrme} = \frac{1}{2}\sum_{i\neq j=1}^{N}\hat{v}_{Skyrme}(\mathbf{r}_i, \mathbf{r}_j)$ is the total potential energy operator obtained by summing the two-body potential energy operator $\hat{v}_{Skyrme}$ over all pairs of particles. ϵ_{Skyrme} breaks down to the following

contributions:

$$\epsilon_{Skyrme} = \epsilon_{kin} + \epsilon_0 + \epsilon_{fin} + \epsilon_3 + \epsilon_{eff} + \epsilon_{so} + \epsilon_{sg}, \tag{2.10}$$

with

$$\begin{aligned}
\epsilon_{kin} &= \frac{\hbar^2}{2m}\tau & (2.11)\\
\epsilon_0 &= \frac{1}{4}t_0[(2+x_0)\rho^2 - (2x_0+1)(\rho_p^2+\rho_n^2)] & (2.12)\\
\epsilon_{fin} &= \frac{1}{32}[3t_1(2+x_1) - t_2(2+x_2)](\nabla\rho)^2 & (2.13)\\
&- \frac{1}{32}[3t_1(2x_1+1) - t_2(2x_2+1)][(\nabla\rho_p)^2 + (\nabla\rho_n)^2] \\
\epsilon_3 &= \frac{1}{24}t_3\rho^\alpha[(2+x_3)\rho^2 - (2x_3+1)(\rho_p^2+\rho_n^2)] & (2.14)\\
\epsilon_{eff} &= \frac{1}{8}[3t_1(2+x_1) - t_2(2+x_2)]\tau\rho & (2.15)\\
&- \frac{1}{8}[3t_1(2x_1+1) - t_2(2x_2+1)](\tau_p\rho_p + \tau_n\rho_n) \\
\epsilon_{so} &= \frac{1}{2}t_4[\mathbf{J}.\nabla\rho + \mathbf{J}_p.\nabla\rho_p + \mathbf{J}_n.\nabla\rho_n] & (2.16)\\
\epsilon_{sg} &= -\frac{1}{16}(t_1x_1 + t_2x_2)\mathbf{J}^2 + \frac{1}{16}(t_1 - t_2)[\mathbf{J}_p^2 + \mathbf{J}_n^2]. & (2.17)
\end{aligned}$$

The number density ρ_q, kinetic energy density τ_q and spin density $\mathbf{J}_q$ for a particular isospin state q are given in terms of the single particle wavefunctions $\phi_{i,q}$ by:

$$\begin{aligned}
\rho_q(\mathbf{r}) &= \sum_{i\in q,s} \omega_i\phi_{i,q}^*(\mathbf{r},s)\phi_{i,q}(\mathbf{r},s) & (2.18)\\
\tau_q(\mathbf{r}) &= \sum_{i\in q,s} \omega_i\nabla\phi_{i,q}^*(\mathbf{r},s).\nabla\phi_{i,q}(\mathbf{r},s) & (2.19)\\
\mathbf{J}_q(\mathbf{r}) &= \sum_{i\in q,s} \omega_i[\phi_{i,q}^*(\mathbf{r},s')\nabla\phi_{i,q}^*(\mathbf{r},s) \times \langle s'|\vec{\sigma}|s\rangle, & (2.20)
\end{aligned}$$

where ω_i is the occupation probability of each single-particle state, s labels the spin components of the wavefunctions and an absence of indices indicates a sum over $q = p, n$, e.g. $\rho = \rho_p + \rho_n$.

The Skyrme energy-density functional in this form is suitable for use in the Hartree-Fock method of the solution of the nuclear many-body problem in the mean field as described in the following sections.

2.2.2 Mean field approximation

In a mean field approximation, two- or more-body interactions are averaged over the whole system, producing an average field in which all the particles move, in order to aid computational tractability (Newton, 2008). A two-body Hamiltonian for N particles may generally be written

$$\hat{H} = \sum_{i=1}^{N} \hat{t}_i(\mathbf{r}_i) + \frac{1}{2} \sum_{i \neq j=1}^{N} \hat{v}_i(\mathbf{r}_i, \mathbf{r}_j). \tag{2.21}$$

Supposing we have found a mean field potential $\hat{u}$ which encodes much of the physics of the two-body potential $\hat{v}$, we can then write equation (2.21) in the form

$$\hat{H} = \sum_{i=1}^{N} \Big\{ \hat{t}_i(\mathbf{r}_i) + \hat{u}_i(\mathbf{r}_i) \Big\} + \Big\{ \frac{1}{2} \sum_{i \neq j=1}^{N} \hat{v}_i(\mathbf{r}_i, \mathbf{r}_j) - \sum_{i=1}^{N} \hat{u}(\mathbf{r}_i) \Big\} = \hat{H}_0 + \hat{H}_1. \tag{2.22}$$

Here $\hat{H}_0$ is the mean field Hamiltonian and $\hat{H}_1$ a residual (perturbative) two-body Hamiltonian that contains any information left out in the process of going from the two-body interaction to the one-body interaction. The mean field basis thus acts as the natural basis from which to conduct perturbation theory. There are many procedures that derive $\hat{u}$ from $\hat{v}$. We use the Hartree-Fock approximation, originally developed for modelling electron motions in atoms but later successfully adopted for calculation of ground state properties of atomic nuclei (Hartree, 1928; Fock, 1930).

2.2.3 The Slater determinant

The Slater determinant (Slater, 1929) is defined as the anti-symmetrised product of the one-particle wavefunctions, written in the occupation number representation as

$$|n_1, n_2, ...\rangle = \hat{a}_1^\dagger \hat{a}_2^\dagger ...|0\rangle, \tag{2.23}$$

where $\hat{a}_i^\dagger$ creates a particle in state i, $|0\rangle$ is the vacuum state and n_i is the number of particles in state i. An eigenstate of a non-interacting (ideal) Fermi gas is given by a single Slater determinant – for example, the ground state will see all the states up to the Fermi surface occupied $\sum_{i \leq i_{Fermi}} \hat{a}_i^\dagger |0>$. For the strongly interacting system of nucleons, scatterings continually remove nucleons from certain states and fill others, so the occupation numbers are not well defined. Then the eigenstates of such a system are given by sums of all possible Slater determinants (with the particles occupying the available states in all possible combinations). The number of ways of arranging the particles amongst all the single particle states is enormous, and such a sum is generally intractable, and we must therefore find an appropriate approximation to reduce the numerical task at hand (Newton, 2008). The approximation made is that the ground eigenstate is given by a single Slater determinant as in the free Fermi gas case. This is called the Hartree-Fock approximation.

2.2.4 The Hartree-Fock Method

In the Hartree-Fock method (Hartree, 1928; Fock, 1930), we approximate the ground state wavefunction by the Slater determinant

$$|\Phi\rangle = |n_1, n_2, ...\rangle = \hat{a}_1^\dagger \hat{a}_2^\dagger ...|0\rangle. \tag{2.24}$$

We proceed via the variational principle, which states that the best approximation to the ground state for the Hamiltonian $\hat{H}$ is obtained for that wave function Φ whose energy expectation value is minimal (Greiner and Maruhn, 1996). Mathematically,

we write

$$\delta\varepsilon_{Skyrme}[\Phi] = \delta\langle\Phi|\hat{H}|\Phi\rangle = 0. \tag{2.25}$$

Carrying out this minimization with respect to the single-particle wavefunctions and Hamiltonian (2.22) yields a set of non-linear single particle Schrödinger equations with the one-body Hartree-Fock potentials:

$$\Big\{ -\nabla\frac{\hbar^2}{2m_q^*}\nabla + u_q(\mathbf{r}) + u_{(so),q}(\mathbf{r})\frac{(\nabla\times\hat{\sigma})}{i}\Big\}\phi_{i,q}(\mathbf{r}) = \epsilon_{i,q}\phi_{i,q}(\mathbf{r}). \tag{2.26}$$

Here $q = p, n$ labels the isospin states, i the single particle states, $u_{(so),q}$ is the spin-orbit potential, u_q is the single particle potential, and m is the effective mass. This set has to be solved self-consistently for the set of single particle wavefunctions which best describe the ground state of the system.

The Hartree-Fock approximation is one realisation of the Landau quasi-particle approximation, in which the 'bare' particle plus the potential energy it possesses, as a result of moving in the mean field, is treated as a quasi-particle, and the occupation numbers are now quasi-particle occupation numbers (Newton, 2008).

The action of the single particle potential upon the single particle wavefunction can be written explicitly in terms of the general two-body potential $\hat{v}$ in coordinate space:

$$u_q(\mathbf{r})\phi_{i,q}(\mathbf{r}) = \Big[\int d^3r'\rho_q(\mathbf{r}')\hat{v}(\mathbf{r},\mathbf{r}')\Big]\phi_{i,q}(\mathbf{r}) - \int d^3r'\rho_q(\mathbf{r},\mathbf{r}')\hat{v}(\mathbf{r},\mathbf{r}')\phi_{i,q}(\mathbf{r}'). \tag{2.27}$$

The first term is the Hartree term and is local. The second term is the Fock (exchange) term and is non-local, in that it depends on the wavefunction being operated on at all points in space. However, the presence of the δ functions in each term of the Skyrme effective potentials, $\hat{v}_{Skyrme}$, will reduce the Fock term to a local term, facilitating calculations (Greiner and Maruhn, 1996).

Using the Skyrme interaction in equation (2.27) we obtain the one-body potentials (derived in a variety of texts, e.g., Greiner and Maruhn (1996), Vautherin and Brink

(1972)):

$$
\begin{aligned}
u_q &= t_0(1+\frac{1}{2}x_0)\rho - t_0(\frac{1}{2}+x_0)\rho_q \qquad (2.28)\\
&+ \frac{1}{12}t_3\rho^\alpha\Big[(2+\alpha)(1+\frac{1}{2}x_3)\rho - 2(\frac{1}{2}+x_3)\rho_q - \alpha(\frac{1}{2}+x_3)\frac{\rho_p^2+\rho_n^2}{\rho}\\
&+ \frac{1}{4}[t_1(1+\frac{1}{2}x_1)+t_2(1+\frac{1}{2}x_2)]\tau - \frac{1}{4}[t_1(\frac{1}{2}+x_1)-t_2(\frac{1}{2}+x_2)]\tau_q\\
&- \frac{1}{8}[3t_1(1+\frac{1}{2}x_1)-t_2(1+\frac{1}{2}x_2)]\nabla^2\rho + -\frac{1}{8}[3t_1(\frac{1}{2}+x_1)+t_2(\frac{1}{2}+x_2)]\nabla^2\rho_q\\
&- \frac{1}{2}t_4(\nabla.J+\nabla.J_q),\\
u_{(so),q} &= \frac{1}{2}t_4(\nabla\rho+\nabla\rho_q)+\frac{1}{8}(t_1-t_2)\mathbf{J}_q, \qquad (2.29)
\end{aligned}
$$

and the effective mass is

$$
\frac{\hbar^2}{2m_q^*} = \frac{\hbar^2}{2m_q} + \frac{1}{4}[t_1(1+\frac{1}{2}x_1)+t_2(1+\frac{1}{2}x_2)]\rho - \frac{1}{4}[t_1(\frac{1}{2}+x_1)-t_2(\frac{1}{2}+x_2)]\rho_q. \quad (2.30)
$$

In the single-particle potential derived above, the pairing force, acting in open shell nuclei, is not included. We adopt the BCS method (Bardeen et al., 1957). The equations are derived in detail in Greiner and Maruhn (1996).

BCS theory introduces correlations between particles into the ground state wave function. It is based upon the ansatz that the ground state wave function including pairing correlations can be written, in the language of second quantisation, as

$$
|BCS\rangle = \sum_{k>0}(u_k + v_k\hat{a}_k^\dagger\hat{a}_{\bar{k}}^\dagger)|0\rangle, \qquad (2.31)
$$

where the states $|k\rangle$ and $|\bar{k}\rangle$ refer to angular momentum states $|ljm\rangle$ and $|lj-m\rangle$, with $m > 0$, and the state $|0\rangle$ is the mean field state, in this work taken to be the Hartree-Fock ground state $|HF\rangle$. This ansatz describes the state $(k,\bar{k})$ as being occupied with a fractional probability v_k^2 and unoccupied with a probability u_k^2, such that $u_k^2+v_k^2=1$. The pairing occupations can be written in terms of the single

particle occupations ω_k by $v_k^2 = \omega_k$ and $u_k^2 = 1 - \omega_k$ (note, though, that the pairing states are occupied by two particles).

To find the pairing energy of the system we use the BCS wavefunction to calculate the matrix elements of the pairing Hamiltonian which consists of a two-body pairing interaction $\hat{V}_{pair} = \frac{1}{2}\sum_{i\neq j=1}^{N} \hat{v}_{pair}(\mathbf{r}_i, \mathbf{r}_j)$ We define the pairing energy functional as

$$\varepsilon_{pair} = \langle BCS|\hat{V}_{pair}|BCS\rangle = 0. \tag{2.32}$$

We implement a simple BCS pairing scheme at zero temperature (Bender et al., 2000; Stone and Reinhard, 2007). The pairing force is approximated as a zero range two-body force between the i^{th} and j^{th} particles (which, in general, is isospin-dependent):

$$\hat{v}_{pair,q}(\mathbf{r}_i, \mathbf{r}_j) = v_{0,q}\delta(\mathbf{r}_i - \mathbf{r}_j). \tag{2.33}$$

With this force, the pairing energy functional can be written

$$\varepsilon_{pair} = \frac{1}{4}\sum_q v_{0,q}\int d^3r \chi_q^2, \tag{2.34}$$

where χ_q is the local pair density

$$\chi_q(\mathbf{r}) = -2\sum_{k\in q} u_k v_k |\phi_{k,q}(\mathbf{r})|^2. \tag{2.35}$$

Since the single particle wavefunctions are normalised, the energy functional reduces to

$$\varepsilon_{pair} = \frac{1}{4}\sum_q v_{0,q}\Big[\sum_{k\in q} u_k v_k\Big]^2. \tag{2.36}$$

The occupation probabilities u_k and v_k are calculated by varying the pairing energy-density functional with respect to them

$$\delta[\varepsilon_{pair}[v_k] - \lambda\langle BCS|\hat{N}|BCS\rangle] = 0, \tag{2.37}$$

where the second term constrains the particle number to the desired value since particle number is not conserved in the BCS scheme. $\hat{N}$ is the particle number operator and λ is the Lagrange multiplier which is equivalent to the Fermi energy of the particles $\lambda \equiv \epsilon_F$. This variational procedure results in the following expression for occupation probabilities:

$$\omega_k^{pair} \equiv v_k^2 = \frac{1}{2}\Big(1 - \frac{\epsilon_k - \epsilon_{F,q}}{\sqrt{(\epsilon_k - \epsilon_{F,q})^2 + \Delta_q^2}}\Big), \tag{2.38}$$

where the quantity Δ_q is called the pairing gap and is given by the equation

$$\Delta_q = v_{0,q} \sum_{k \in q} u_k v_k. \tag{2.39}$$

We have the requirement that

$$A_q = \sum_{k \in q} v_k^2, \tag{2.40}$$

where $A_p = Z$ and $A_n = N$. These equations need to be solved self-consistently. We adopt the simplest approach, the constant gap approach, in which the gap is directly parametrized so that equation (2.39) does not need to be solved. The parametrization taken is (Langanke et al., 1991):

$$\Delta \equiv \Delta_q = (11.2\text{MeV}/\sqrt{A}). \tag{2.41}$$

We note that the BCS method is not self-consistent with the basic mean field approach. The variation with respect to the occupation probabilities is performed only for the pairing energy functional and not the whole mean field energy functional. Conversely, the variation with respect to the single particle wavefunctions is performed only for the basic mean field energy functional, excluding the pairing energy functional (Newton, 2008). The self-consistent approach is called Hartree-Fock-Bogoliubov (Bogoliubov, 1959; Baranger, 1963).

2.2.5 Skyrme models used in this work

The models of the Skyrme force are fitted to reproduce a certain set of observable properties of nuclei in an optimal way.

There are many different sets of the Skyrme parametrization resulting from different fits by various authors (Dutra et al., 2012). We chose two traditional forces, SkM* and SLy4, and two forces, NRAPR and SQMC700, which successfully satisfied up-to-date experimental and observational constraints on properties of nuclear matter (Dutra et al., 2012). Their parameters are given in table 2.1.

Table 2.1: The four Skyrme parametrizations used in this Thesis.

Parameter	SkM*	SLy4	NRAPR	SQMC700
t_0 [MeVfm^3]	-2645.0	-2488.9	-2719.7	-2429.1323
t_1 [MeVfm^5]	410.0	486.8	417.64	370.9804
t_2 [MeVfm^5]	-135.0	-546.4	-66.687	-96.6917
t_3 [MeVfm$^{3+3\alpha}$]	15595.0	13777.0	15042.0	13773.6340
x_0	0.09	0.83	0.16154	0.100
x_1	0.0	-0.34	-0.047986	0.0
x_2	0.0	-1.0	0.027170	0.0
x_3	0.0	1.35	0.13611	0.0
α	0.16667	0.16667	0.14416	0.16667

Chapter 3

Computational method

As stated in chapter 1, we use a 3D-SHF approximation with a phenomenological Skyrme model for the nuclear force with BCS pairing. In the calculation, it is assumed that, at a given density and temperature, matter is arranged in a periodic structure throughout a sufficiently large region of space for a unit cell to be identified. This single unit cell needs to be calculated to obtain the bulk and microscopic properties of the matter. The calculation is performed in cubic cells with periodic boundary conditions and assuming reflection symmetry across the three Cartesian axes. Only shapes with cubic symmetry are allowed. The required reflection symmetry allows us to get solutions only in one octant of the unit cell, which reduces significantly the computer time. The only effect of confining ourselves to 1/8 of the cell is that we can only consider triaxial shapes. If we would consider the whole cell, we would get the same results, with additional asymmetric shapes, which we are currently omitting.

It is expected that the absolute minimum of the free energy of a cell containing A nucleons is not going to be particularly pronounced and there will be a host of local minima separated by relatively small energy differences. In order to systematically survey the "shape space" of all nuclear configurations of interest, the quadrupole moment of the neutron density distributions has been parametrized, and those

parameters constrained. It is expected that the proton distribution follows closely that of the neutrons.

The minimum of the free energy in a cell at a given particle number density, temperature and a proton fraction is sought as a function of 3 free parameters, the number of particles in the cell (determining the cell size) and the parameters of the quadrupole moment of the neutron distribution β, γ. Each minimization takes approximately 12 hours on a single CPU core in computers like the National Center for Computational Sciences (NCCS) Cray XT5/XK6 machine at ORNL and is performed in a trivially parallel mode, typically using 45,000 processors in one run to perform separate minimizations over a range of densities $0.02-0.12$ fm^{-3}, temperatures $0-10$ MeV and a fixed proton fraction of $y_p = 0.3$, where we have spent approximately 2.3×10^6 CPU hours. We also performed calculations over a range of proton fractions $y_p = 0.01 - 0.35$, though that results are not presented in this Thesis. The total amount of CPU time spent was then $\sim 23 \times 10^6$ hours.

This chapter provides a description of the essential physics which forms the basis of the numerical method used to obtain the results presented in this Thesis. The main sources are Ring and Schuck (1980), Greiner and Maruhn (1996) and Newton (2008). The Oxford DPhil Thesis by William Newton (Newton, 2008), who developed the 3DHFEOS code, used in this Thesis, contains details of the numerical background and basic implementation of the code for calculation of the pasta phase of supernova matter. The code had to be adapted for efficient use on the ORNL supercomputer.

3.1 The Uniform Matter EoS

In this section we include the physical basis for the construction of an EoS of uniform nuclear matter. This approach follows the development in Bonche and Vautherin (1981) and Pandharipande and Ravenhall (1989).

The system is described by a quantum mechanical Hamiltonian $\hat{H}$, with eigenstates $|\Phi_I\rangle$ (where I labels the many body states; those states made up of different

permutations of the constituent particles in the available single particle energy levels) and an energy spectrum E_I given by

$$\hat{H}|\Phi_I\rangle = E_I|\Phi_I\rangle. \tag{3.1}$$

Operating in the grand canonical ensemble, in which the average energy and average particle number of the system are fixed, the probability of finding a particle in a state $|\Phi_I\rangle$ at temperature T is given by

$$\mathcal{P}_I = \frac{1}{\mathcal{Z}} e^{-\beta(E_I - N_I\mu)}, \tag{3.2}$$

where N_I is the number of particles in state I, μ is the chemical potential of a particle, $\beta = 1/k_B T$, k_B is the Boltzmann's constant and the grand partition function $\mathcal{Z}$ is defined

$$\mathcal{Z} = \sum_I e^{-\beta(E_I - N_I\mu)}. \tag{3.3}$$

From equation (3.2) we can define all the necessary thermodynamic quantities: the average value of an observable represented by the operator $\hat{O}$ is given by

$$\langle\hat{O}\rangle = \sum_I \mathcal{P}_I \langle\Phi_I|\hat{O}|\Phi_I\rangle. \tag{3.4}$$

The grand potential Ω_G and entropy S can be defined

$$\Omega_G = -k_B T \ln \mathcal{Z} \tag{3.5}$$

$$S = -k_B \sum_I \mathcal{P}_I \ln \mathcal{P}_I = -\frac{\partial \Omega_G}{\partial T}\Big|_{V,\mu}, \tag{3.6}$$

such that the expression for the average energy of the system U is given by

$$U = \langle\hat{H}\rangle = \sum_I \mathcal{P}_I E_I = \frac{T^2}{\mathcal{Z}} \frac{\partial \Omega_G}{\partial T}\Big|_{V,\mu} = -T^2 \frac{\partial}{\partial T}\Big(\frac{\Omega_G}{T}\Big)_{V,\mu} = \Omega_G + TS, \tag{3.7}$$

and finally the pressure is given by

$$P = -\frac{\partial U}{\partial V}\Big|_{S,N_I} = -\frac{\partial \Omega_G}{\partial V}\Big|_{T,\mu}. \tag{3.8}$$

The system of nucleons is uniform and isotropic so the single particle states can be represented by plane waves.

In the Hartree-Fock approximation, the eigenstates of the many body Hamiltonian are written as

$$|\Phi_I\rangle = |n_1(I), n_2(I), ...\rangle. \tag{3.9}$$

The sums over the many body states I in the partition function can then be replaced by sums over the single particle states $n_i(I)$ and we can write the partition function as

$$\begin{aligned} \mathcal{Z} &= \sum_{n_i(I)=0,1} \exp\Big\{-\beta\Big[\sum_i n_i(e_i-\mu)\Big]\Big\} \\ &= \prod (1+e^{-\beta n_i(e_i-\mu)}). \end{aligned} \tag{3.10}$$

Then, from equation (3.4), the average occupation of a state i (the occupation probability) at a temperature T is given by

$$\begin{aligned} \langle n_i\rangle &= \frac{1}{\mathcal{Z}} \sum_{n_i(I)=0,1} n_i(I) \exp\Big\{-\beta\Big[\sum_j n_j(e_j-\mu)\Big]/k_BT\Big\} \\ &= (1+e^{-\beta(e_i-\mu)})^{-1} \equiv \omega_i^{FD}, \end{aligned} \tag{3.11}$$

which is the Fermi-Dirac distribution function.

Since each Fermion state is characterised by a wavenumber k and has a spin degeneracy $g = 2$, we have the following expressions for the number, entropy and

energy densities:

$$\rho = \frac{\langle N\rangle}{V} = \frac{g}{h^3}\int d^3p\omega(p) = \frac{g}{(2\pi)^3}\int d^3k\omega(k) \tag{3.12}$$

$$s = \frac{S}{V} = -k_B\frac{g}{(2\pi)^3}\int d^3k[\omega(k)\ln\omega(k) + (1-\omega(k))\ln(1-\omega(k))] \tag{3.13}$$

$$e = \frac{U}{V} = \frac{g}{(2\pi)^3}\int d^3ke(k)\omega(k). \tag{3.14}$$

Here the volume of an element of quantum mechanical phase space is given by h^3 and we have written $\omega_i \to g\omega(k)$, $e_i \to e(k)$, i.e. the states are distinguished (up to the spin quantum number) by their momentum $p = \hbar k$.

For uniform, isotropic, nuclear matter, the wavefunctions of particles must be translationally invariant, and hence take the form of plane waves. In addition, a spin 1/2 and isospin 1/2 eigenstate (represented by the spinors $\chi_s^{(1/2)}$ and $\chi_t^{(1/2)}$) must be included. We thus have, in a volume of space V,

$$\phi_i(r) = \phi_{kst}(r) = \frac{1}{V^{1/2}}e^{i\vec{k}.\vec{r}}\chi_s^{1/2}\chi_t^{1/2}. \tag{3.15}$$

The densities and currents are constant throughout uniform matter, so their derivatives disappear. Writing the single particle potential and effective masses (2.28), (2.29), (2.30) in terms of the baryon number density ρ and the proton and neutron fractions $y_p = \rho_p/\rho$, $y_n = \rho_n/\rho$, we get

$$\begin{aligned} u_q &= t_0\rho[(1+\frac{1}{2}x_0) - (\frac{1}{2}+x_0)y_q] \\ &+ \frac{1}{12}t_3\rho^{\alpha+1}[(2+\alpha)(1+\frac{1}{2}x_3) - 2(\frac{1}{2}+x_3)y_q - \alpha(\frac{1}{2}+x_3)(y_p^2+y_n^2)] \\ &+ \frac{1}{4}[t_1(1+\frac{1}{2}x_1) + t_2(1+\frac{1}{2}x_2)]\tau - \frac{1}{4}[t_1(\frac{1}{2}+x_1) - t_2(\frac{1}{2}+x_2)]\tau_q, \end{aligned} \tag{3.16}$$

$$\frac{\hbar^2}{2m_q^*} = \frac{\hbar^2}{2m_q} + \rho\frac{1}{4}[t_1(1+\frac{1}{2}x_1) + t_2(1+\frac{1}{2}x_2)] - \rho\frac{1}{4}[t_1(\frac{1}{2}+x_1) - t_2(\frac{1}{2}+x_2)]y_q. \tag{3.17}$$

The kinetic energy of a single particle state is given by

$$e_{KE} = \langle \phi_{kst} \Big| \Big(- \frac{\hbar \nabla^2}{2m^*} \Big) \Big| \phi_{kst} \rangle = - \frac{\hbar k^2}{2m^*}, \tag{3.18}$$

where the effective mass, m^*, is constant in uniform matter at a given density. We are now in a position to write down the single particle energies of all particle species present. The nucleon and lepton single particle energies are given by:

$$e_q = \frac{\hbar^2 k^2}{2m_q^*} + u_q + m_q c^2 \tag{3.19}$$

$$e_i = (\hbar^2 k^2 c^2 + m_i^2 c^4)^{1/2}, \tag{3.20}$$

where $q = p, n$ labels the nucleon species and $i = e^{-/+}, \mu, \nu$, the lepton species (electrons, positrons, muons and neutrinos). We have used the fully relativistic expression for the single particle energies of leptons, assumed to be free particles. Note that we include the rest masses of the particles. The single particle potential energies must be included. We neglect contributions to the energies from the Coulomb potential; the direct term in this energy is zero because of the charge neutrality of the matter, and at densities above nuclear saturation the exchange term is negligible (Shapiro and Teukolsky, 1986).

Inserting the single particle energies into the integrals (3.12),(3.13),(3.14) we can obtain expressions for the chemical potentials μ, number densities ρ, total kinetic energy densities τ and entropy densities s of each particle species, as we shall see next.

3.1.1 The finite temperature EoS

To derive the number, kinetic energy and entropy densities for all particle species present in matter, we need the Fermi-Dirac integrals, which are written as

$$G_k(\eta) = \int_0^\infty \frac{x^k dk}{e^{(x-\eta)} + 1}, \tag{3.21}$$

for integer $k > -1$ and

$$F_k(\eta;\lambda) = \int_0^\infty \frac{x^k(1+\lambda x/2)^{1/2}dx}{e^{(x-\eta)}+1}, \tag{3.22}$$

for half-integer $k > -1$.

In the limit $\lambda \to \infty$, the above two integrals are related by

$$F_k(\eta;\lambda) = \sqrt{\frac{\lambda}{2}} G_{k+1/2}(\eta). \tag{3.23}$$

To produce an accurate EoS, the Fermi-Dirac integrals must be evaluated as precisely as possible. We use the program developed in Miralles and Riper (1996), in which the integrals are evaluated using expansions in the limits of degeneracy and relativity, and direct numerical integration for intermediate regions.

Full derivations of the main quantities involved in the finite temperature EoS have been derived in Newton (2008), so we give only final expressions here.

We write the single particle energies of the nucleons, including their rest mass, as

$$e_q = \frac{\hbar^2 k^2}{2m_q^*} + u_q + m_q c^2, \tag{3.24}$$

where $q = n, p$ and u_q is the single particle potential defined in equation (2.28).

The number and kinetic energy densities are given by

$$\rho_q = \frac{1}{2\pi^2}\left(\frac{2m_q^*}{\beta\hbar^2}\right)^{3/2} F_{1/2}(\eta_q;0) \tag{3.25}$$

and

$$\tau_q = \frac{1}{2\pi^2}\left(\frac{2m_q^*}{\beta\hbar^2}\right)^{5/2} F_{3/2}(\eta_q;0), \tag{3.26}$$

where we have included the spin degeneracy factor $g = 2$, and integrated over the angular part assuming the matter to be isotropic. $\eta_q = \beta(\mu_q - u_q - m_q c^2)$ is the degeneracy parameter.

For the entropy density, we get

$$\frac{s_q}{k_B} = \frac{1}{2\pi^2}\Big(\frac{2m_q k_B T}{\hbar^2}\Big)^{3/2}\Big[\frac{5}{3}F_{3/2}(\eta_q;0) - \eta_q F_{1/2}(\eta_q;0)\Big]. \tag{3.27}$$

For the leptons, $i = e, \mu$, we use the fully relativistic expression for the single particle energies:

$$e_i(k) = m_i c^2[\sqrt{1+(\hbar k/mc^2)^2} - 1], \tag{3.28}$$

excluding the rest mass.

For the number density, we introduce the relativity parameter $\lambda_i = k_B T/m_i c^2$, the degeneracy parameter $\eta_i = (\mu - m_i c^2)/k_B T$, and we can write

$$\rho_i \;\; = \tfrac{1}{\pi^2}\Big(\tfrac{m_i c}{\hbar}\Big)^3 \lambda_i^{3/2}\sqrt{2}[F_{1/2}(\eta_i;\lambda_i) + \lambda F_{3/2}(\eta_i;\lambda_i)]. \tag{3.29}$$

Similarly, the energy density is given by

$$\epsilon_i \;\; = \tfrac{1}{\pi^2}\Big(\tfrac{(m_i c)^4}{\hbar^3}\Big)^3 \lambda_i^{5/2}\sqrt{2}[F_{3/2}(\eta_i;\lambda_i) + \lambda F_{5/2}(\eta_i;\lambda_i)] + n_i m_i c^2, \tag{3.30}$$

and the entropy density is given by

$$\begin{aligned}\frac{s_i}{k_B} &= \frac{1}{\pi^2}\Big(\frac{m_i c}{\hbar}\Big)^3 \lambda_i^{3/2} 2^{1/2}\Big[\frac{5}{3}F_{3/2}(\eta_i;\lambda_i) + \frac{4}{3}\lambda_i F_{5/2}(\eta_i;\lambda_i) \\ &- \eta_i F_{1/2}(\eta_i;\lambda_i) - \eta_i\lambda_i F_{3/2}(\eta_i;\lambda_i)\Big].\end{aligned} \tag{3.31}$$

Neutrinos are treated as a massless ultra-relativistic Fermi gas with single particle energies:

$$e_\nu = \hbar k c. \tag{3.32}$$

The number and energy densities are given by

$$\rho_\nu = \frac{1}{\beta^3\hbar^3c^3\pi^2}G_2(\eta) \tag{3.33}$$

$$e_\nu = \frac{1}{\beta^4\hbar^3c^3\pi^2}G_3(\eta), \tag{3.34}$$

and the entropy density is given by

$$\frac{s_\nu}{k_B} = -\frac{1}{\beta^3\hbar^3\pi^2}[\eta G_2(\eta) - G_3(\eta)]. \tag{3.35}$$

For an ideal photon gas at temperature T, we use the standard expressions for the energy density ϵ_γ and entropy density s_γ:

$$\epsilon_\gamma = \frac{3\pi^2(k_BT)^4}{45\hbar^3c^3} \tag{3.36}$$

$$s_\gamma = \frac{4\epsilon_\gamma}{3k_BT}. \tag{3.37}$$

3.2 Non-Uniform Matter

In this section we outline the main features of the 3DHFEOS. Detailed description can be again found in Newton (2008).

3.2.1 Implementation of the 3DHFEOS Code

For infinite uniform matter, the Hartree-Fock equations have an analytic solution since the eigenfunctions are plane waves and the energy spectrum is continuous. However, for inhomogeneous matter, we do not know a priori what the eigenfunctions will be — other than that they will not be pure plane waves. Thus the Hartree-Fock equations must be solved with the added complication that the terms in the Hamiltonian that depend on the derivatives of the wavefunctions will not be zero. Since the eigenfunctions we are solving for also form the densities and currents in the

one-body potential, this is a self-consistency problem. In order to solve the Hartree-Fock equations, first the initial wavefunctions are guessed, then the densities, currents and potentials are calculated, and then new wavefunctions are formed by operating on the old ones with the Hamiltonian. The process is iterated until a measure of the discrepancy between old and new wavefunctions becomes sufficiently small. This algorithm can be either performed in a coordinate space, in which all functions and operations are represented on a spatial grid, or in some basis space, in which the wavefunctions are expanded in terms of a set of basis functions (for example in terms of harmonic oscillator functions) and their expansion coefficients determined from the resulting matrix equation. We choose the former of these two representations, since a single basis is insufficient for describing all the states that make up the matter we are interested in. Some nucleons will occupy bound states, in which case their wavefunctions can be related to a harmonic oscillator basis, and some will occupy continuum states, in which case their wavefunctions will look similar to plane waves.

3.2.2 The computational domain and grid

In three-dimensions, the simplest periodic cell is a rectangular one. We will take such a cell to be our computational domain and use Cartesian coordinates. Let us denote the coordinates by $x_\alpha, 1 \leq \alpha \leq 3$, such that $x_1 \equiv x, x_2 \equiv y, x_3 \equiv z$. We take the origin to be the centre of the cell, and each coordinate to run over $-l_\alpha \leq x_\alpha \leq l_\alpha$ so that the length of the cell in each direction is $2l_\alpha$. Note that the exact choice of Cartesian axes is arbitrary; there is as yet no external constraint on the orientation of the cell. Our computational domain is discretised to form a grid of collocation points x_α (the points in space at which we assign values to our functions) with even spacings in each direction δx_α. Reflection symmetry implies that we can either arrange the grid so that the origin is a collocation point:

$$x_\alpha = i\delta x_\alpha, \quad i = -i_\alpha, -i_\alpha + 1, ..., i_\alpha - 1, i_\alpha, \tag{3.38}$$

or we can arrange the grid so that each collocation point is placed halfway between those points in equation (3.38):

$$x_\alpha = (i + \frac{1}{2})\delta x_\alpha, \quad i = -i_\alpha, -i_\alpha + 1, ..., i_\alpha - 1, i_\alpha. \tag{3.39}$$

Here $i_\alpha = l_\alpha/\delta x_\alpha$ is the number of positive grid points (including the origin).

Since we want our computational domain to represent one cell in an effectively infinite periodic array, choosing the second option guarantees that each point is unique to our cell. Then a function at a given collocation point $\{i, j, k\}$ is denoted by

$$f(x, y, z) \Rightarrow f(x_i, y_j, z_k) \equiv f_{ijk}. \tag{3.40}$$

The discretisation in coordinate space corresponds to a truncation in momentum state in the sense that the maximum momentum that can be represented on a grid of spacing δx corresponds to a maximum wavenumber $k_{max} = 1/\delta x$. We must make sure, therefore that our choice of δx allows us to represent the full momentum spectrum of states.

In order to reduce the numerical task, we assume that parity in all three Cartesian directions is a good quantum number. For a given direction x, the parity operator in that direction $\hat{P}$ and a function on the grid $f(x)$ must hence satisfy

$$\hat{P}f(x) = f(-x) = pf(x), \tag{3.41}$$

where $p = \pm 1$ is the parity quantum number in that direction. Imposing parity conservation means that we only need to compute functions in the positive octant of the grid $x, y, z \geq 0$, and, like this, we are only considering triaxial shapes.

3.2.3 Boundary conditions

At a given temperature and density, matter is arranged locally in a periodic structure.

Bloch's theorem states that the most general form of any solution to the Schrödinger equation in a periodic potential must obey the relation:

$$\Psi_{k,q}(\mathbf{r}+\mathbf{T}) = e^{i\mathbf{K}.\mathbf{T}}\Psi_{k,q}(\mathbf{r}), \tag{3.42}$$

where $\mathbf{T}$ is the translation from the position $\mathbf{r}$ to the equivalent positions in the adjacent cells, and $\mathbf{K}$ is the Bloch momentum covector. This implies that the wavefunctions must be of the form

$$\Psi_{k,q}(\mathbf{r}) = e^{i\mathbf{K}.\mathbf{r}}\phi_{k,q}(\mathbf{r}), \tag{3.43}$$

where $\phi_{k,q}$ obeys the simple periodic condition

$$\phi_{k,q}(\mathbf{r}+\mathbf{T}) = \phi_{k,q}(\mathbf{r}). \tag{3.44}$$

We will be working in terms of the wavefunctions $\phi_{k,q}(\mathbf{r})$ so it is the simple periodic boundary conditions that we must enforce. In this Thesis we take a Bloch wavevector $\mathbf{K} = 0$ with the understanding that we can move to full Bloch boundary conditions within the same framework.

3.2.4 Wavefunctions

In three dimensions, the wavefunctions take the form

$$\phi_{n_x,n_y,n_z}(x,y,z) = u_{n_x}(x)u_{n_y}(y)u_{n_z}(z) \times \chi_{s,m_s}, \tag{3.45}$$

where χ_{s,m_s} is a spinor for a spin state labelled by spin quantum numbers s, m_s. As we explain in the next section, we omit the spin-orbit force from the Hartree-Fock Hamiltonian, so that the spinor part of the wavefunction will be neglected from now on. We are left with three quantum numbers associated with the three spatial degrees of freedom $n_\alpha \equiv n_x, n_y, n_z$. Before we begin to solve the Hartree-Fock equations,

we must choose the initial wavefunctions. We have two options: Gaussian times polynomial (GP),

$$u_{n_\alpha} = N P_{n_\alpha}(x_\alpha) e^{-(x_\alpha/\omega_\alpha)^2}, \tag{3.46}$$

or Fermi-Dirac (plane wave) (FD)

$$u_{n_\alpha, p_\alpha} = N \cos(k_\alpha x_\alpha + \pi p_\alpha/2), \tag{3.47}$$

where N is a normalisation constant, $P_n(x)$ is an nth order polynomial in x which contains only terms of parity $(1)^{n_\alpha}$, and p_α the parity of the state in the direction α and the wavevector $k_\alpha = n_\alpha \pi/(2l_\alpha)$ (where $2l_\alpha$ is the length of the grid).

The wavefunctions are initially ordered according to their quantum numbers n_x, n_y and n_z (see Table 3.1).

Table 3.1: Quantum numbers n_x, n_y and n_z for the first few single particle states; lowest energy is at the top.

0	0	0
1	0	0
0	1	0
0	0	1
1	1	0
1	0	1
0	1	1
1	1	1
2	0	0
0	2	0
0	0	2

For the GP wavefunctions, the parity is given by $p_\alpha = (1)^{n_\alpha}$ and for the FD wavefunctions, the three parities are additional independent quantum numbers. Therefore, for the FD wavefunctions, there are eight possible combinations of the parity quantum numbers in three dimensions for each value of n_x, n_y and n_z.

It is important to note that the total number of wavefunctions available to us is limited by the number of grid points. The quantum numbers n_x, n_y and n_z can only

take values up to the number of grid points plus one in the given direction, since that is the total number of wavefunction nodes that our grid can accommodate when the collocation points are placed half way in between the grid points. Thus the total number of GP wavefunctions available is equal to the total number of grid points. For FD wavefunctions, the number available is a factor of 8 greater. For these reasons, we use the GP wavefunctions. FD wavefunctions have been previously tested (Newton, 2008) and give the same results when one does constrained calculations.

To reduce further the computational time, we take advantage of the fact that, under the action of time reversal,

$$\mathbf{r} \rightarrow \mathbf{r}; \mathbf{p} \rightarrow -\mathbf{p}; t \rightarrow -t, \tag{3.48}$$

single particle states with opposite values of total angular momentum projection are degenerate. This is called the Kramers Degeneracy (Greiner and Maruhn, 1996). We can use this, provided we have an even number of nucleons in our system, to associate two nucleons with each single particle state, thus cutting the computational workload. We enforce this degeneracy in the code but we note that we are restricted to systems of even N and Z (Newton, 2008). We note that it would be unlikely for the lowest ground state to be a neighboring odd Z, N sate due to pairing, which tends to lower the energy of even-even nuclear shapes.

3.2.5 The Hartree-Fock equations

The Hartree-Fock equations in Cartesian coordinates are written as:

$$
\begin{aligned}
&-\frac{\hbar^2}{2m_q^*}(x,y,z)\Big[\frac{d^2}{dx^2}\frac{d^2}{dy^2}\frac{d^2}{dz^2}\Big]\phi_{(n_x,n_y,n_z),q}(x,y,z) \\
&-\Big(\frac{d}{dx}\frac{\hbar^2}{2m_q^*}(x,y,z)\Big)\Big(\frac{d}{dx}\phi_{(n_x,n_y,n_z),q}(x,y,z)\Big) \\
&-\Big(\frac{d}{dy}\frac{\hbar^2}{2m_q^*}(x,y,z)\Big)\Big(\frac{d}{dy}\phi_{(n_x,n_y,n_z),q}(x,y,z)\Big) \\
&-\Big(\frac{d}{dz}\frac{\hbar^2}{2m_q^*}(x,y,z)\Big)\Big(\frac{d}{dz}\phi_{(n_x,n_y,n_z),q}(x,y,z)\Big) \\
&+u_q(x,y,z))\phi_{(n_x,n_y,n_z),q}(x,y,z) = \epsilon_{n_x,n_y,n_z}\phi_{(n_x,n_y,n_z),q}(x,y,z).
\end{aligned}
\tag{3.49}
$$

The densities are given by

$$
\rho_q(x,y,z) = \sum_{(n_x,n_y,n_z)\in q} \omega_{n_x,n_y,n_z}\phi^2_{(n_x,n_y,n_z),q}(x,y,z) \tag{3.50}
$$

$$
\tau_q(x,y,z) = \sum_{n_x,n_y,n_z} \omega_{n_x,n_y,n_z}(\nabla\phi_{(n_x,n_y,n_z),q}(x,y,z))^2, \tag{3.51}
$$

where $u_q(x,y,z)$ is the single particle Hartree-Fock potential given by (2.28).

The Hartree-Fock equations form a self-consistent problem in the sense that the wave functions determine the mean field, while the mean field in turn determines the wave functions. In practice this leads to iterative solutions in which one starts from an initial guess for the wavefunctions, such as those for the harmonic-oscillator and determines the mean field from them. Solving the Schrödinger equations then yields a new set of wave functions, and this process is repeated until, hopefully, convergence is achieved (Greiner and Maruhn, 1996).

We note that in order to reduce the computational task further, we leave out the whole spin-orbit part of the Hartree-Fock Hamiltonian: this allows us to omit the spinor part of the wavefunction, thus cutting the computation time by roughly two.

It also allows us to use purely real wavefunctions, which reduces the computation time by another factor of roughly two (Newton, 2008).

The spin-orbit interaction is an important factor in determining the correct shell energy. It has been shown by Negele and Vautherin (1973) that in matter nearing homogeneity, the spin-orbit force for neutrons does not play a large role. The proton density will be less homogeneous, so the spin-orbit interaction will be important in determining the correct level ordering for them.

Also, matter in supernova configurations is very much less homogeneous than for neutron star configurations (the density of the external neutron gas is much smaller), and so the spin-orbit interaction will be important there. However, we feel that it is more important to obtain the results which contain the bulk properties of the supernova matter. We also note that the spin-orbit force will not be important for the overall energy and pressure of the cell, as it will not significantly change the ground-state, and will not alter the ordering of shapes. It will, though, have a big effect on the single particle spectrum, which might be important when calculating, for example, neutrino cross-sections, which goes beyond the purpose of this Thesis.

3.2.6 Iterations

The principle of an iterative solution to the Hartree-Fock equations is to start with an initial guess of the wavefunctions (single particle states) and construct a successive set of wavefunctions through an operation on the previous set, with the single particle Hartree-Fock Hamiltonian $\hat{h}_{HF}$. Repeating this process, the wavefunctions will converge to a solution of the Hartree-Fock equations. However, since we are interested in the ground state, we need to guarantee that our choice of the iterative process will converge to that. For example, if one takes the prescription that the wavefunctions of the $(n+1)^{\text{th}}$ iteration are formed from those of the n^{th} by

$$\phi_i^{(n+1)} = \hat{h}_{HF}\phi_i^{(n)}, \tag{3.52}$$

then the wavefunctions will converge to the highest eigenvalue of $\hat{h}_{HF}$ (Reinhard and Cusson, 1982).

Instead, we choose a set of trial wavefunctions ϕ_i, which may be expanded in the basis of the Hartree-Fock states which we are trying to find:

$$\phi_i = \sum_j a_{ji}\phi_{HF,j}. \tag{3.53}$$

Then, if we operate on these wavefunctions with the operator $e^{-\lambda(\hat{h}_{HF}-\epsilon_i)}$, we obtain

$$e^{-\lambda(\hat{h}_{HF}-\epsilon_i)}\sum_j a_{ji}\phi_{HF,j} = \sum_j a_{ji}e^{-\lambda(\epsilon_j-\epsilon_i)}\phi_{HF,j}. \tag{3.54}$$

Then those states with large energies will be removed from the trial wavefunction, because of the exponential operator, leaving the lowest energy states. As the iteration proceeds, the energy of the trial wavefunction will converge to ϵ_j.

We employ two different criteria to determine if a solution has converged at any given iteration: the difference in energy in consecutive iteration steps and the variances.

The current difference in energy at the n^{th} iteration is given by

$$\delta E = E^n - E^{n-1}. \tag{3.55}$$

When this falls below a certain value, we can consider that the wavefunctions have converged, and we impose $\delta E < 10^{-10}$ MeV.

The total variance of the proton or neutron single particle energies at iteration n is given by

$$\langle \delta h^2 \rangle_q = \sum_i \omega_{i,q}\Big\{\langle\phi_{i,q}|(h^n_{HF})^2|\phi_{i,q}\rangle - (\langle\phi_{i,q}|h^n_{HF}|\phi_{i,q}\rangle)^2\Big\}, \tag{3.56}$$

where the sum is over all occupied states. Again, once both the proton and neutron total variances drop below a certain value, we can consider that the calculation converged, and we impose $\langle \delta h^2 \rangle_q < 1.0$ MeV^2.

The variances provide a more robust indication that the iteration has converged. When the criterion given above for the variance is fulfilled, we find that the energy difference criterion is automatically fulfilled.

3.2.7 Zero temperature occupation probabilities

At zero temperature, we employ the pairing scheme set out in section 2.2.4. We shall denote the pairing occupation probabilities by ω_k^{pair} which are related to the standard pairing notation for occupation (v_k) and non-occupation (u_k) probabilities by $v_k^2 = \omega_k^{pair}$ and $u_k^2 = 1 - \omega_k^{pair}$.

The basic pairing equations to be solved in the constant gap approach are those for the occupation probabilities, equation (2.38), under the constraint (2.40) with the gap parameter Δ given by equation (2.41).

One problem with using a zero range pairing interaction is that it tends to overestimate the coupling to high-energy (continuum) states. To simulate the effect of finite range forces and inhibit the high-energy coupling, Bender et al. (2000) introduced smooth energy dependent cutoff weights

$$f_{k,q} = \frac{1}{1 + exp[(\epsilon_{k,q} - \epsilon_{F,q} - \delta E_q)/\omega_{\epsilon,q}]}, \tag{3.57}$$

where $\epsilon_{F,q}$ is the Fermi energy of isospin state q. This acts to confine the active pairing space to the vicinity of the Fermi surface. The quantity δE_q, which determines the range of energy around the Fermi energy that pairing is active, is determined from the condition

$$A_q + 1.65 A_q^{2/3} = \sum_{k \in q} f_{k,q}, \tag{3.58}$$

which is chosen such that the sum of the cutoff weights includes approximately one additional shell of single particle states above the Fermi surface (which contains approximately $1.65A_q^{2/3}$ states). For zero temperature, the quantity $\omega_{\epsilon,q}$ is taken to be 10 MeV to give acceptable results in finite nuclei (Bonche et al., 1985).

With this addition, we make the change $\Delta \to f_{k,q}\Delta$ in the gap and occupation number equations, resulting in

$$\omega_{k,q}^{pair} = \frac{1}{2}\Big(1 - \frac{\epsilon_{k,q} - \epsilon_{F,q}}{\sqrt{(\epsilon_{k,q} - \epsilon_{F,q})^2 + f_{k,q}^2\Delta_q^2}}\Big) \tag{3.59}$$

$$A_q = \sum_{k\in q} \omega_{k,q}^{pair}. \tag{3.60}$$

The scheme with which we calculate the above quantities at any given iteration follows the one in Bender et al. (2000).

3.2.8 Finite temperature occupation probabilities

At finite temperatures, the occupation probabilities are given by the FD distribution

$$\omega_{k,q}^{FD} = \frac{1}{1 + e^{-(\epsilon_{k,q} - \mu_q)/k_BT}}, \tag{3.61}$$

where the chemical potential μ_q is again given by the particle number requirement (3.59). To solve for this distribution at a given iteration, we evolve the single particle wavefunctions according to our iterative scheme. With the new single particle wavefunctions $\phi_{k,q}^{(n)}$, we calculate the new Hamiltonian $\hat{h}^{(n)}$, using the occupation probabilities $\omega_{k,q}^{FD,(n-1)}$ and the new single particle energies $\epsilon_{k,q}^{(n)}$. We obtain the new Fermi energy $\epsilon_q^{F,(n)}$ of the particles, by solving equation (3.59) with the occupation probabilities $\omega_{k,q}^{(n-1)}$, using a secant iteration (Press et al., 2007). Finally, the new occupation probabilities $\omega_{k,q}^{FD,(n)}$ are formed from equation (3.61).

3.2.9 The quadrupole constraint

The basic Hartree-Fock iteration converges to a final configuration whose shape depends on the initial configuration, which itself depends on the number of nucleons in the cell, and hence the cell size.

In order to control the deformation of our nuclear configuration, we need to impose a constraint on the nuclear shape. This will allow us to systematically search over the deformation space (the energy surface with respect to the shape of the nuclear configuration) by performing calculations at relevant values of the parameters we choose to describe the deformation. In this way, we will be able to self-consistently find all the local minima in the energy, as a function of the deformation, that result from different nuclear shapes.

Since we have imposed reflection symmetry across the three Cartesian axes, there will be no asymmetric deformations such as dipole or octupole. We thus impose a constraint on the quadrupole moment of the proton and neutron densities, neglecting the next order of deformation consistent with our boundary conditions, hexadecapole, since it is expected to give energy variations at least an order of magnitude smaller than that of the quadrupole deformation (Newton, 2008).

In Cartesian coordinates, the quadrupole operator is given by

$$\hat{Q} = \{Q_{ab}\} = \begin{pmatrix} 2x^2 - y^2 - z^2 & 3xy & 3xz \\ 3xy & 2y^2 - z^2 - x^2 & 3yz \\ 3xz & 3yz & 2z^2 - x^2 - y^2 \end{pmatrix} \tag{3.62}$$

and the matrix elements of the operator and its square are defined as

$$q_{ab} = \langle \hat{Q}_{ab} \rangle = \sum_{i=1}^{N} \langle \phi_i | Q_{ab} | \phi_i \rangle = \int \rho Q_{ab} dV \tag{3.63}$$

$$q_{ab}^2 = \langle \hat{Q}_{ab}^2 \rangle = \sum_{i=1}^{N} \langle \phi_i | Q_{ab}^2 | \phi_i \rangle = \int \rho Q_{ab}^2 dV, \tag{3.64}$$

The matrix elements of a triaxial shape may be put in diagonal form: $q_{ab} = 0$ for $a \neq b$, $q_{ab} = q_a$ for $a \in x, y, z$. The quadrupole operator itself can then be taken to be diagonal. The three non-zero quadrupole moments must also fulfil $q_x + q_y + q_z = 0$, so only two of them are independent.

The nuclear shape $R(x, y, z)$ is usually parametrized by the dimensionless quadrupole moments α_a defined by $q_a = R_0\alpha_a$ such that

$$R(x, y, z) = R_0(1 + \alpha_x\xi^2 + \alpha_y\eta^2 + \alpha_z\zeta^2), \tag{3.65}$$

where $\xi = x/R_0, \eta = y/R_0, \zeta = z/R_0$ and R_0 is the root mean square nuclear radius. One can also write equation (3.65) in spherical polar coordinates:

$$R(x, y, z) = R_0(1 + \alpha_{20}Y_{20}(\theta, \phi) + \alpha_{22}Y_{22}(\theta, \phi) + \alpha_{2-2}Y_{2-2}(\theta, \phi)), \tag{3.66}$$

which defines the dimensionless spherical polar quadrupole moments. We can relate them to their Cartesian counterparts via

$$\alpha_{2\pm2} = \sqrt{\frac{2\pi}{15}}(\alpha_x - \alpha_y) \equiv \alpha_2 \tag{3.67}$$

$$\alpha_{20} = \sqrt{\frac{8\pi}{90}}(2\alpha_z - \alpha_x - \alpha_y) \equiv \alpha_0, \tag{3.68}$$

where α_0 is the relative stretch along the z axis of the nucleus with respect to the x and y axes and α_2 is the relative difference in length between the x and y axes.

We are using an alternative parametrization, that involves the parameters β and γ (Greiner and Maruhn, 1996):

$$\alpha_0 = \beta\cos\gamma \qquad \alpha_2 = \frac{1}{\sqrt{2}}\beta\sin\gamma, \tag{3.69}$$

that are analogous to the polar coordinates parameters. β represents the deformation of the configuration, and γ the direction of the deformation: $\gamma = 0°$ gives prolate deformations and $\gamma = 60°$ gives oblate deformations.

In order to constrain the nuclear configuration to particular values of the quadrupole moments, we add to the Hartree-Fock Hamiltonian a constraining force:

$$\hat{h}_{HF} \rightarrow \hat{h}_{HF} + \lambda_c.\hat{Q}, \tag{3.70}$$

where $\hat{Q}$ is the quadrupole operator given in equation (3.62) and λ_c is the strength of the constraining force. When the quadrupole matrix is diagonal, $Q = \{Q_a\}$, then the strength is a vector with three components $\lambda_c = \{\lambda_{c,a}\}$ for each component.

We specify our desired quadrupole moments through the polar coordinates α, β given in equation (3.69). These are then turned into the moments q_a through equations (3.67), the requirement that $\alpha_x + \alpha_y + \alpha_z = 0$ and the definition $q_a = R_0\alpha_a$.

The force strength needs to be updated iteration by iteration as it drives the quadrupole moments towards the desired values. This is implemented via the scheme presented in Cusson et al. (1985).

We apply the constraint only to the neutrons. Since matter is neutron rich, the proton distribution will follow the neutron distribution to a good degree of accuracy.

3.2.10 The Coulomb interaction

The Coulomb potential arising from the electrostatic interaction between protons and electrons comprises a direct term and an exchange term. The direct term is obtained from Poisson's equation

$$\nabla^2\Phi = 4\pi\varrho_p, \tag{3.71}$$

where ϱ_p is the charge density of protons, which we approximate as the charge times the spatial density of the species $e\rho_p$, which neglects the finite size of the particles. This is a good approximation on the distance scales of the size of the cell considered.

One can solve it by writing the electrostatic potential as a Fourier series:

$$\Phi(x,y,z) = \sum_{l,m,n=0}^{\infty} \tilde{\Phi}(k_x,k_y,k_z) \cos\left(\frac{l\pi x}{l_x} + \varphi_x\right) \cos\left(\frac{m\pi y}{l_y} + \varphi_y\right) \cos\left(\frac{n\pi z}{l_z} + \varphi_z\right). \tag{3.72}$$

Substituting in equation (3.71), we get

$$\tilde{\Phi}(k_x,k_y,k_z) = 4\pi\varrho_p\left(\frac{l^2\pi^2}{l_x^2} + \frac{m^2\pi^2}{l_y^2} + \frac{n^2\pi^2}{l_z^2}\right)^{-1}. \tag{3.73}$$

An inverse Fourier transform recovers $\Phi(x,y,z)$. The Coulomb solver is implemented using the FFTW software package (Frigo and Johnson, 2005).

The exchange term is evaluated via the Slater approximation (Slater, 1951) which gives the expression:

$$\Phi_{exch} = -\left(\frac{3}{\pi}\right)^{1/3} \rho_p^{1/3}. \tag{3.74}$$

3.2.11 Center of mass correction

The mean field localises the nucleus and breaks translational invariance. The result is a spurious oscillation of the nucleus in the mean field, and a corresponding addition to the total energy. A simple way of correcting for this is to subtract the zero point energy of harmonic oscillations about the centre of mass:

$$E_{cm} = \frac{P_{cm}^2}{2Am}, \tag{3.75}$$

where $P_{cm} = \sum_{i=1}^{A} \hat{p}_i$ is the total momentum operator, A is the nucleon number and m the average nucleon mass. An approximate treatment takes $P_{cm}^2 \approx \sum_{i=1}^{A} \hat{p}_i^2$ and the energy correction becomes a correction in the nucleon mass:

$$\frac{h^2}{2m} \to \frac{h^2}{2m}(1 - 1/A), \tag{3.76}$$

making this correction very small for large number of nucleons.

3.3 Composition of matter in CCSN

In the situation relevant to the core-collapse stage of a supernova and shortly after in the hot PNS, we expect the following species of particles to be present at densities around nuclear saturation: nucleons n, p, electrons e, positrons e^+, electron neutrinos ν_e, anti-electron neutrinos $\bar{\nu}_e$ and photons γ.

Baryon conservation requires

$$y_p + y_n = 1. \tag{3.77}$$

Charge conservation requires

$$y_p = y_{e^-} + y_{e^+}. \tag{3.78}$$

Chemical equilibrium with respect to the weak interaction is achieved through the following interactions:

$$e^- + p \leftrightarrow n + \nu_e \tag{3.79}$$

$$e^+ + n \leftrightarrow p + \bar{\nu}_e, \tag{3.80}$$

which results in the following relation between the chemical potentials μ of the participating species:

$$\mu_{e^-} + \mu_p = \mu_n + \mu_{\nu_e} \tag{3.81}$$

$$\mu_{e^+} + \mu_n = \mu_p + \mu_{\bar{\nu_e}}. \tag{3.82}$$

Combining the two relations above, we obtain

$$\mu_n - \mu_p = \mu_{e^-} - \mu_{\nu_e} = \mu_{\bar{\nu_e}} - \mu_{e^+}. \tag{3.83}$$

Finally, the chemical potential of a particle is the symmetric of its anti-particle, and so we have the relations

$$\mu_{e^+} = -\mu_{e^-} \tag{3.84}$$

$$\mu_{\nu_e} = -\mu_{\bar{\nu_e}}. \tag{3.85}$$

If neutrinos are trapped, the electron flavour fraction Y_e defined by

$$Y_e = y_{e^-} - y_{e^+} + y_{\nu_e} - y_{\bar{\nu_e}} \tag{3.86}$$

is conserved. Combined with equation (3.78), we get the relation

$$Y_e = y_p + y_{\nu_e} - y_{\bar{\nu_e}}. \tag{3.87}$$

At a given temperature T and density ρ, we wish to solve the above equations for a given fixed electron-lepton fraction Y_e. We employ a secant algorithm based on that given in Press et al. (2007).

3.3.1 Construction of the EoS

Having found the composition of the matter, one can now calculate the energy density and pressure. The kinetic energy densities and the entropy densities of the various particle species are derived in section 3.1.1. The total energy density for the baryon part is then written as

$$\epsilon_b = \frac{\hbar^2(\tau_p + \tau_n)}{2m_q} + \rho m_q c^2 + \epsilon_{Skyrme}, \tag{3.88}$$

where ϵ_{Skyrme} is the total energy density of matter from the nuclear interaction and is given by equation (2.10). Then, the total energy density of the system can be written:

$$\begin{aligned}\epsilon(\rho_p, \rho_n, \rho_{e^-}, \rho_{e^+}, \rho_\mu, \rho_{\nu_e}, n\rho_{\bar{\nu}_e}, \epsilon_\gamma) &= \epsilon_b(\rho_p, \rho_n) + \rho_n m_n c^2 + \rho_p m_p c^2 \\ &+ \epsilon_{e^-}(\rho_{e^-}) + \rho_{e^-} m_{e^-} c^2 + \epsilon_{e^+}(\rho_{e^+}) + \rho_{e^+} m_{e^+} c^2 + \epsilon_\mu(\rho_\mu) + \rho_\mu m_\mu c^2 \\ &+ \epsilon_{\nu_e}(\rho_{\nu_e}) + \epsilon_{\bar{\nu}_e}(\rho_{\bar{\nu}_e}) + \epsilon_\gamma. \end{aligned} \tag{3.89}$$

The total entropy density can then be calculated:

$$\begin{aligned}s(\rho_p, \rho_n, \rho_{e^-}, \rho_{e^+}, \rho_\mu, \rho_{\nu_e}, \rho_{\bar{\nu}_e}, s_\gamma) &= s_p(\rho_p) + s_n(\rho_n) \\ &+ s_{e^-}(\rho_{e^-}) + s_{e^+}(\rho_{e^+}) + s_\mu(\rho_\mu) + s_{\nu_e}(\rho_{\nu_e}) + s_{\bar{\nu}_e}(\rho_{\bar{\nu}_e}) + s_\gamma, \end{aligned} \tag{3.90}$$

and the Helmholtz free energy density, which is the total energy of the system available to be converted into mechanical work at a constant temperature, is then given by

$$f = \epsilon - Ts. \tag{3.91}$$

The pressure P is finally computed using the thermodynamic relation for the total internal energy

$$E = TS - PV + \sum_i N_i \mu_i, \tag{3.92}$$

which, on dividing through by volume and rearranging, gives

$$P = -f + \mu_p \rho_p + \mu_n \rho_n + \mu_{e^-} \rho_{e^-} + \mu_{e^+} \rho_{e^+} + \mu_\mu \rho_\mu + \mu_{\nu_e} \rho_{\nu_e} + \mu_{\bar{\nu}_e} \rho_{\bar{\nu}_e}. \tag{3.93}$$

By calculating the pressure P in this way, at each value of density ρ and temperature T, the EoS is built.

For uniform matter, the gradient terms in ϵ_{Skyrme} are zero and (2.10) becomes

$$\epsilon_{Skyrme} = \frac{1}{4}t_0\rho^2[(2+x_0) - (2x_0+1)(y_p^2+y_n^2)]$$
$$+ \frac{1}{24}t_3\rho^{\alpha+2}[(2+x_3) - (2x_3+1)(y_p^2+y_n^2)]$$
$$+ \frac{1}{8}[t_1(2+x_1) + t_2(2+x_2)]\tau\rho + \frac{1}{8}[t_2(2x_2+1) - t_1(2x_1+1)]\rho(\tau_p y_p + \tau_n y_n). \quad (3.94)$$

For the non-uniform matter case, the total energy of the nuclear configuration including the contribution to the Coulomb force from the electrons and protons is given by (Langanke et al., 1991):

$$\varepsilon_{skyrme} + \varepsilon_{coul} = \frac{1}{2}\Big(\varepsilon_{kin} + \sum_{\beta}\omega_\beta\epsilon_\beta\Big) + \varepsilon_{rearr} + \varepsilon_{quad} + \varepsilon_{pair} + \varepsilon_{rearr,coul} + \varepsilon_{e,coul} + \varepsilon_{lattice}. \quad (3.95)$$

The kinetic energy is given by

$$\varepsilon_{kin} = \sum_q \int_V \frac{\hbar^2}{2m_q}\tau_q dx\, dy\, dz. \quad (3.96)$$

The rearrangement energy, which results from the density dependent term ($\propto t_3$) in the Skyrme interaction, is given by

$$\varepsilon_{rearr} = -\int_V \frac{\alpha}{24}t_3\rho^\alpha\{(1+\frac{1}{2}x_3)\rho^2 - (\frac{1}{2}+x_3)(\rho_p^2+\rho_n^2)\}dx\, dy\, dz. \quad (3.97)$$

The quadrupole constraint has an associated artificial energy that must be subtracted off from the total energy. It is given by

$$\varepsilon_{quad} = -\sum_{\alpha\in x,y,z}\int_V \lambda_{c,a}\rho_q Q_a dx\, dy\, dz. \quad (3.98)$$

The energy due to the pairing interaction is given by

$$\varepsilon_{pair} = -\sum_q v_{0,q}\Big\{\sum_{k\in q}\Delta_q f_k\sqrt{\omega_k(1-\omega_k)}\Big\}^2. \tag{3.99}$$

The Coulomb rearrangement energy, which comes from the Slater term in the Coulomb potential, is given by

$$\varepsilon_{rearr,coul} = -\frac{3}{4}\Big(\frac{3}{\pi}\Big)^{1/3}\int_V \rho_p^{4/3}dx\,dy\,dz. \tag{3.100}$$

We will have an energy due to the Coulomb interaction of the protons with electrons. This is referred as the lattice energy:

$$\varepsilon_{lattice} = e\int_V \rho_p\Phi_e dx\,dy\,dz. \tag{3.101}$$

and the contribution to the electron energy from the interaction of the electrons with the protons and with themselves is given by:

$$\varepsilon_{e,coul} = e\int_V \rho_e\Big(\frac{1}{2}\Phi_e + \Phi_p\Big)dx\,dy\,dz. \tag{3.102}$$

For the nucleon entropy density, s_q, we can no longer use (3.27), since we have a discrete energy spectrum of the nucleons in non-uniform matter. The expression then becomes

$$Vs_q = -2k_B\sum_i\{\omega_{i,q}\ln\omega_{i,q} - (1-\omega_{i,q})\ln(1-\omega_{i,q})\}, \tag{3.103}$$

where the factor 2 comes from the Kramers degeneracy and V is the volume of the computational cell.

There will also be non-nucleonic components to the matter. For this study, we shall assume that electrons are the only other charged particles present (i.e. the only particles whose interactions with nucleons we have to take into account) and have a uniform density. Other particles present are treated exactly as they are in the uniform matter case. The electrons will generate their own Coulomb potential, Φ_e, which is

solved in the same way as for the proton Coulomb potential. We need to take this into account now because the protons are not distributed homogeneously in the electron gas.

The expressions for the energy and entropy of the electrons are the same as those in section 3.1.1, equations (3.30) and (3.31), except that in the inhomogeneous medium, we must take into account the electrostatic interaction between the electrons and the inhomogeneous proton distribution. This is done by adding to the single particle kinetic energies of the electrons an electrostatic potential term, Φ:

$$e_e = (\hbar^2 k^2 c^2 + m_i^2 c^4)^{1/2} + e_{Coul}, \tag{3.104}$$

where

$$e_{Coul} = \frac{e}{Z} \int_V \Big(\frac{1}{2} \Phi_e \rho_e + \Phi_p \rho_p \Big) dx\, dy\, dz. \tag{3.105}$$

3.4 Running of the 3DHFEOS code

Each run of 3DHFEOS, at a given temperature T, contains a specified number of neutrons N and protons Z, with total nucleon number $A = N + Z$. The proton fraction is fixed at $y_p = Z/A$. Given the volume of the computational cell, V, the baryon number density is fixed at $\rho = A/V$. One can adjust the nucleon number and the box size so that the baryon number density stays the same. Thus, a calculation at a given value of ρ does not correspond to a unique value of A. One must perform calculations over many values of A to obtain all possible configurations at a given density. A, or equivalently the cell size, is thus a free parameter over which we must search.

The other free parameters are β and γ, the neutron quadrupole moments deformation parameters. Once again, we must search over the deformation space to see how the energy varies with the nuclear shape. We note that we can have physically identical shape configurations, that will have the same energy, but are

characterized by different β, γ values. It is therefore difficult to use the neutron quadrupole moments parameters to track changes in shape.

The above constitute three free parameters. One must perform one calculation for each point in the three-dimensional phase space at each EoS point, or, in other words, at each triplet of density, temperature and proton fraction in which we are interested. Then we need to minimize the free energy density with respect to these free parameters in order to find the minimum energy configuration state. In this Thesis, we cover the range of densities $0.02 - 0.12$ fm^{-3} and temperatures $0 - 10$ MeV.

Chapter 4

Numerical results

We have fully described the physical basis of the 3D-SHF model and the numerical techniques implemented in the 3DHFEOS code used to obtain part of the results in this Thesis in Pais and Stone (2012). The results concerning the pasta-uniform phase transition will be submitted for publication.

4.1 The pasta phase

We present here the evolution of the pasta formation from its onset to its dissolution into uniform matter, obtained fully self-consistently, without any preconceptions. Possible shapes were limited by technical constraints on the calculation, as we assumed parity conservation (reflection symmetry) and a cubic shape of the unit cell. All classical pasta formations, starting from spherical droplets through rods, slabs, tubes (cylindrical holes) and bubbles (spherical holes) were observed for all Skyrme force models. The shapes are illustrated in Fig. 4.1 for the SMC700 Skyrme force as an example at threshold densities for each shape.

We show the 3D image in the top row and the yx, xz and yz projections in the 2nd, 3rd and 4th rows, respectively. In the tube and bubble regions we found the cylindrical (spherical) holes appearing exactly in the edges (corners) of the unit cell and not in the center as expected in the bcc or fcc symmetries, which are in principle

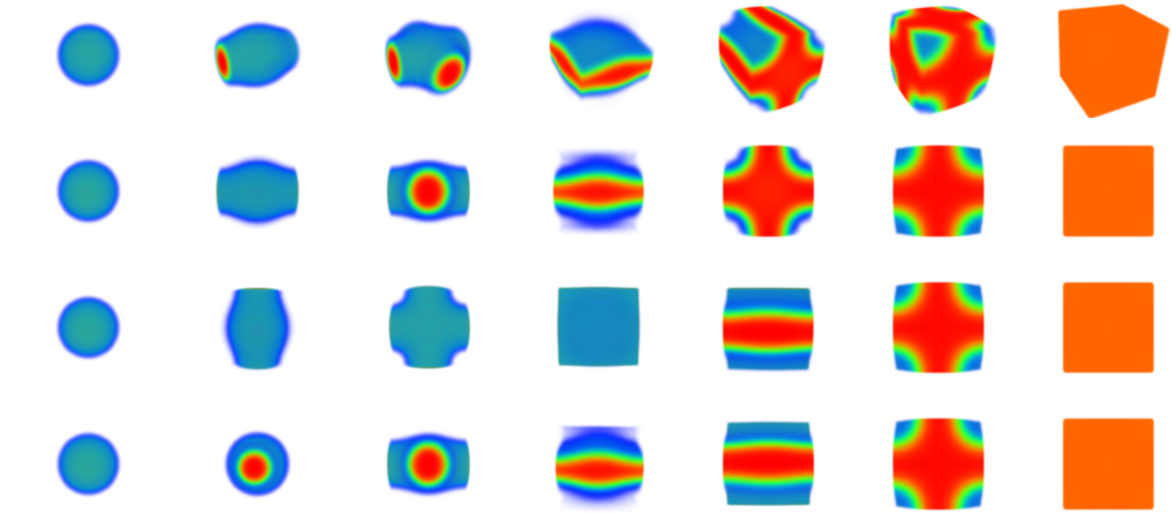

Figure 4.1: First row: Pasta phases calculated using the SQMC700 Skyrme interaction, $T = 2$ MeV and $y_p = 0.3$. Rows 2, 3, 4: 2D projection of the pasta phases on the (y,x), (x,z) and (y,z) planes, respectively. The neutron density distribution is shown at the density corresponding to the onset of each phase, known with the uncertainty given in brackets. Blue (red) color indicates the bottom (top) of the density scale: 0.001 (dark blue) - 0.02475 (light blue) - 0.0485 (green) - 0.07225 (light orange) - 0.095 (red) fm^{-3}. The pasta formation shown here appears for all the Skyrme models, but the threshold density changes somewhat, see Fig. 4.4.

allowed in a cubic box. The reason for this effect is likely to be that in our model we calculate the density distribution only in one octant of the cell and assemble the whole cell using reflection symmetry. This procedure reduces the higher order bcc and fcc symmetries to a simple cubic symmetry. The use of reflection symmetry makes the 3DHFEOS code manageable. Removal of that symmetry would increase the demand on computational time by a factor of 8 which is not realistic at this time.

It is well known that the pasta formation is not only density dependent but also changes with temperature. A typical global picture of the development of pasta formations as a function of increasing number density is shown in Figures 4.2 and 4.3, for all the interactions and temperatures of 2 and 10 MeV. We find that the range of densities for which the pasta phase is fully developed is rather wide (0.04 - 0.11 fm^{-3}) at low temperatures and gets narrower with increasing temperature (0.04 - 0.07 fm^{-3}), as expected. Interestingly, the lower density transition remains the same for all temperatures. Avancini et al. (2012) obtained a similar result with the TF approximation — the transition to the rods phase does not seem to depend on temperature. Also, in Sonoda et al. (2008), within a QMD calculation, it is seen that the onset of the pasta, i.e., the rodlike nuclei, occurs at $\sim 0.2\rho_0$ for $T < 4$ MeV.

4.1.1 Transition densities between pasta formations

In addition to the qualitative studies of the pasta shapes as a function of number density and temperature, we were able to obtain quantitative information on transition densities between individual phases as shown in Fig. 4.4.

For comparison, we give the results for QMD model 2 (QMD2) (Sonoda et al., 2008) in the figure caption. Our transitions appear to be rather sharp and occur within 0.002 fm^{-3} or less density change without any obvious intermediate regions. However, we observe a stable shape, occurring for all four Skyrme models, between the rods and slabs (a cross-rod) in the low density region between 0.03 - 0.05 fm^{-3}. This formation may be akin to the "spongelike" intermediate phase reported in Sonoda

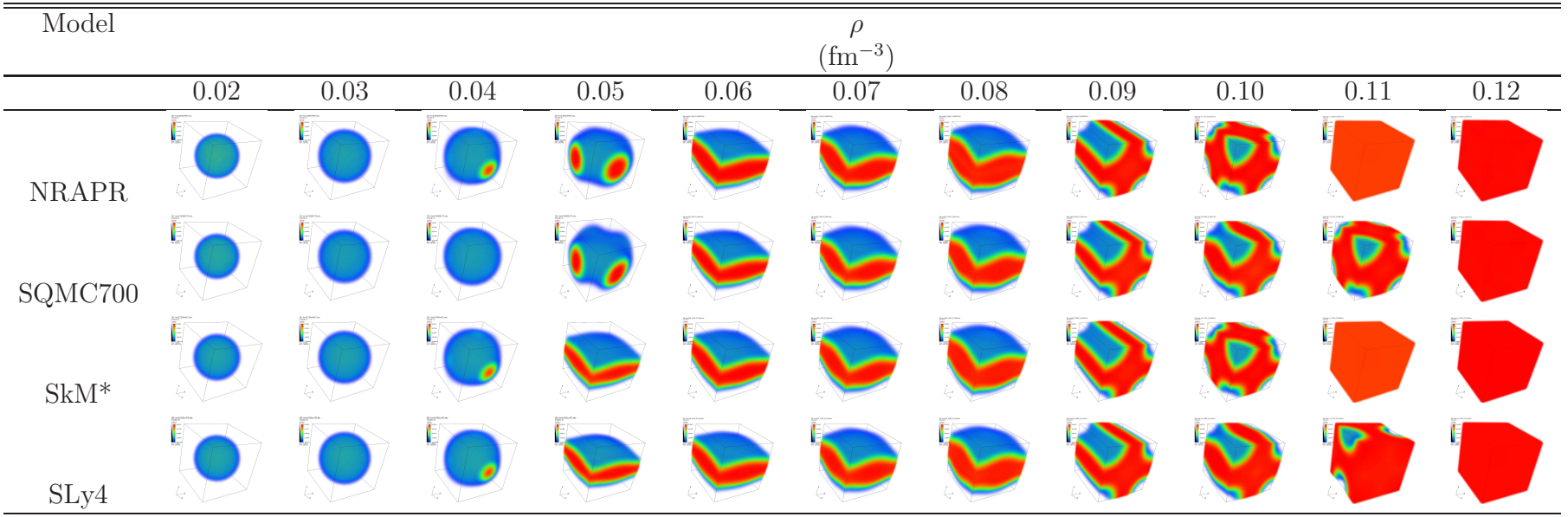

Figure 4.2: Evolution of the neutron density distribution ρ_{N} for $y_p = 0.3$ and $T = 2$ MeV with increasing total particle number density ρ for all the Skyrme interactions. Blue indicates low densities and red the high densities.

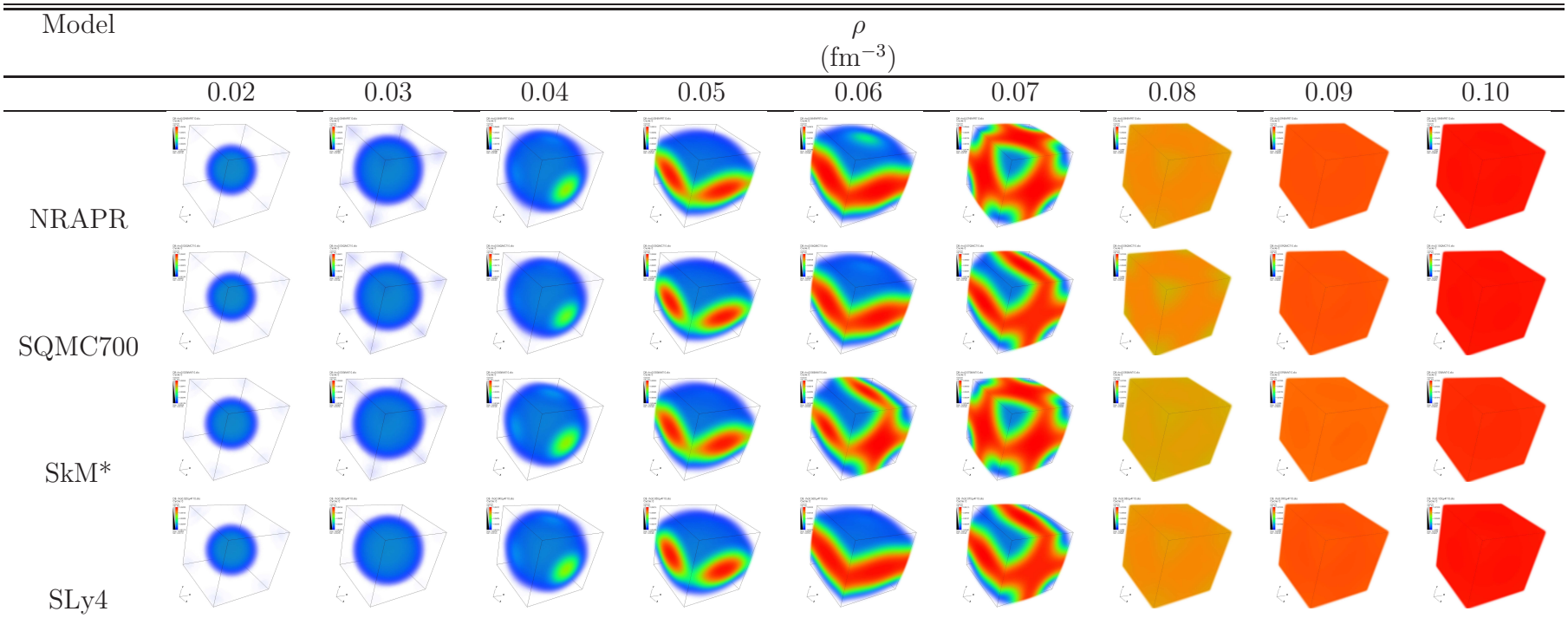

Figure 4.3: Evolution of the neutron density distribution ρ_{N} for $y_p = 0.3$ and $T = 10$ MeV with increasing total particle number density ρ for all the Skyrme interactions. Blue indicates low densities and red the high densities.

et al. (2008) and denoted (C,S). We, however, do not have an equivalent to their (S,CH) structure between slabs and cylindrical holes.

Williams and Koonin (1985) also found a shape between rods and slabs (they called it "cross") that might be quite similar to our cross-rod shape, although their calculations were performed at $y_p = 0.5$ and $T = 0$ MeV.

Comparison with the most recent work of Avancini et al. (2012) who used TF and CP approximations to RMF with NL3 and TW Lagrangians reveals more similarities in the phase diagrams, although the cross-rod formation has not been reported in Avancini et al. (2012). Unfortunately detailed comparison of threshold densities for individual pasta phases cannot be made as we do not have results at temperatures used in Avancini et al. (2012).

As can be seen from these results, the change in particle number density between individual formations is of the order 0.002 fm^{-3} or smaller. This corresponds to a quite fast reorganization of matter. Similar effect was observed by Ravenhall et al. (1983). Comparison with other calculations does not allow one to draw further conclusions: either the formalism is too restrictive (Avancini et al., 2012) or the calculation was not performed with the same precision (Sonoda et al., 2008).

In the TF calculations done (Avancini et al., 2010, 2012), the transition between configurations is not continuous and occurs when the free energy density of one of the configurations is smaller than the free energy density of the other configurations.

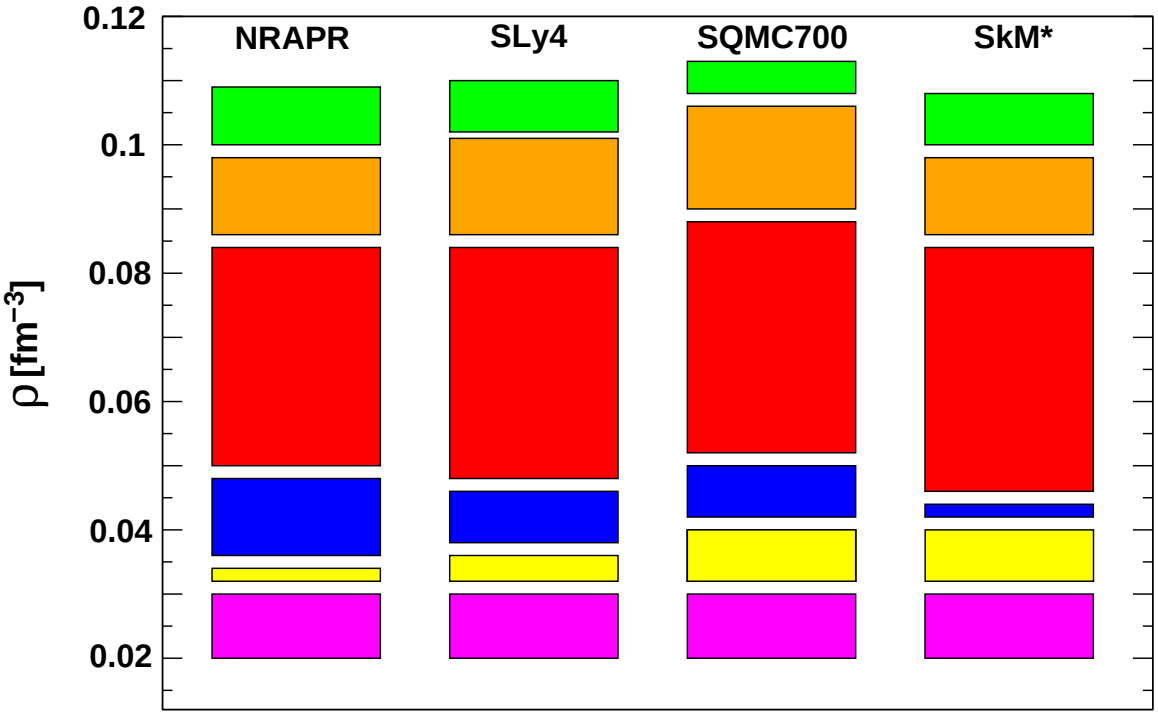

Figure 4.4: Comparison of phase diagrams at $T = 2$ MeV and $y_p = 0.3$ as calculated for the four Skyrme interactions used in the 3DHFEOS model. The sequence of phases from bottom to top is spherical droplets (magenta) - no pasta, rods (yellow), cross-rods (blue), slabs (red), cylindrical holes (tubes) (orange) and spherical holes (bubbles) (green). The white gaps between colored boxes represent transition regions in which calculation is not available. The onset densities of each phase can be compared with results of Sonoda et al. (2008), who found the following regions of densities (all in fm^{-3} rounded to 3 decimal places): 0.017 - 0.029 (spherical droplets), 0.034 (rods), 0.059 - 0.063 (slabs), 0.080 - 0.084 (cylindrical holes) and 0.088 - 0.109 (spherical holes).

4.2 Transition between the pasta phase and uniform matter

The transition between the pasta phase and uniform matter has been a focus of attention for some time. It was usually determined by a comparison of the density dependence of some observable (free energy density, pressure or entropy), as calculated for uniform matter and, as in a separate calculation, for inhomogeneous matter including the pasta phase (Newton and Stone, 2009; Bonche and Vautherin, 1981; Negele and Vautherin, 1973).

Previously, when the EoS of supernova matter has been assembled which included both the inhomogeneous and homogeneous phase, the Maxwell or Gibbs construction would need to be employed to connect the two phases in a thermodynamically consistent way. We illustrate this technique in Fig. 4.5 where the density dependence of pressure at $T = 2$ MeV is plotted as derived from the Lattimer and Swesty (1991) model in comparison with the EoS calculated in the 3DHFEOS model for the NRAPR interaction, where no connection is needed to make the transition. Since the Lattimer-Swesty model employs a Maxwell construction, they obtain a range of densities where the pressure is constant, removing, as a result, the first order phase transition. In our model, we see a jump in the pressure, indicating the first order phase transition. Since these are two different models, we should not expect an exact match for the uniform part.

Figs. 4.1, 4.2 and 4.3 in the previous section have demonstrated the transition between pasta and homogeneous matter in a general way. In Figure 4.6, we show in more detail the accuracy with which the graphical analysis revealed this transition for all four Skyrme parametrizations.

In Table 4.1 we compare our results for the temperature dependence of the onset density of homogeneous matter with those obtained by Sonoda et al. (2008) and Avancini et al. (2012). Our model and that of Avancini et al. (2012) predict a slower

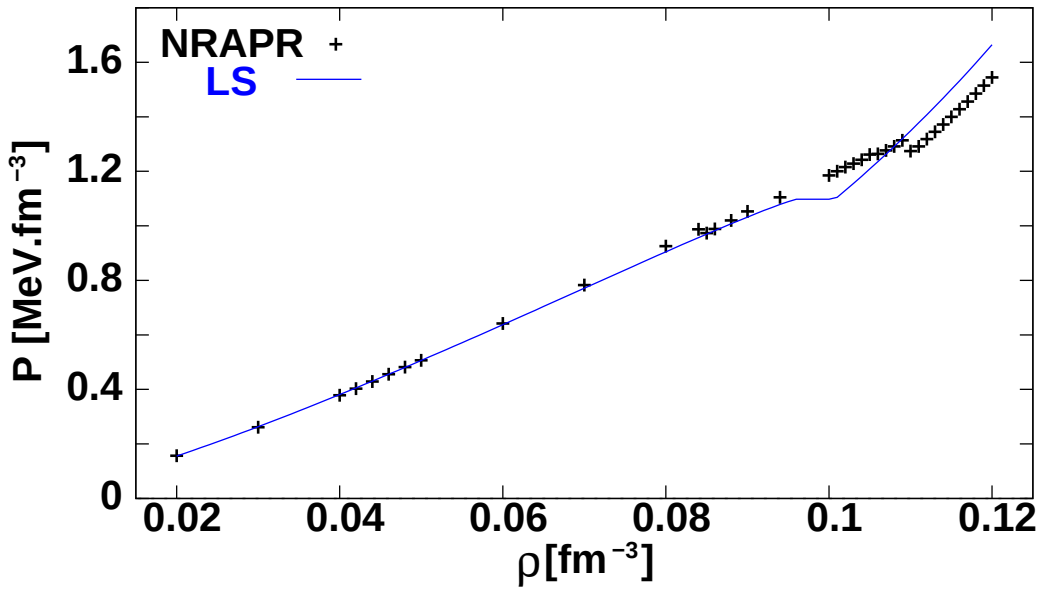

Figure 4.5: Pressure versus density for the NRAPR interaction and the Lattimer-Swesty EoS. The transition to uniform matter happens at different densities since they are two different models.

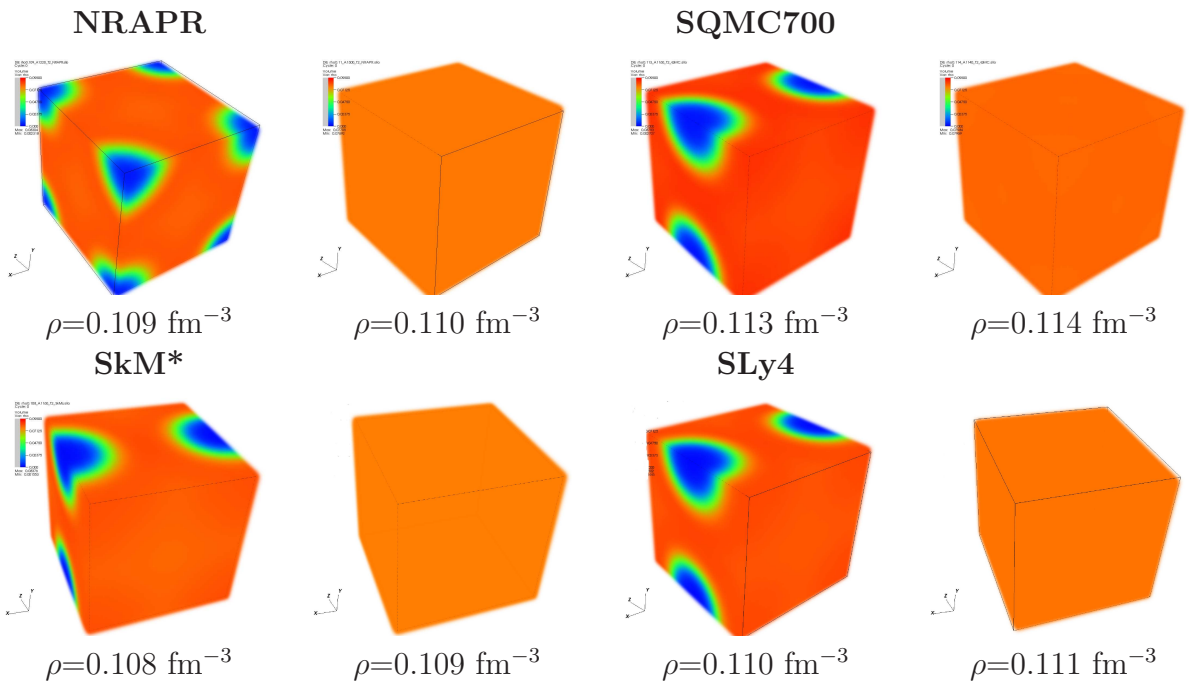

Figure 4.6: Neutron density distributions for $T = 2$ MeV at the transition from non-uniform to uniform matter for all interactions.

decrease of the threshold density with temperature in comparison with Sonoda et al. (2008), who do not observe pasta phase at all at $T = 10$ MeV.

This is illustrated in Fig. 4.7 where the average for the four Skyrme interactions, the TF and CP approximations for NL3 and TW interactions and the QMD2 model results are plotted against temperature.

It has been suggested on the basis of QMD models (Sonoda et al., 2008; Watanabe et al., 2009) that the slope $L(\rho_0) = 3\rho_0 \frac{\partial E_{sym}(\rho)}{\partial \rho}|_{\rho=\rho_0}$ of the symmetry energy E_{sym}, calculated at nuclear saturation density ρ_0, is inversely related to the critical temperature T_c at which pasta disappears, i.e., the higher the value of L, the lower would be the critical temperature. However, as seen in Table 4.2, the NL3 model has a significantly higher value of L than the QMD2 and yet, both it, and the present calculation, which have the lowest L values, predict T_c well above that of QMD2. Thus the proposed relation between L and T_c does not appear to hold universally. However, T_c could be influenced by other quantities such as the incompressibility (Avancini et al., 2006).

4.2.1 First order character of the phase transition

The first order nature of the transition to uniform nuclear matter has been predicted in the past (Lamb et al., 1983; Williams and Koonin, 1985). We are in a unique position to determine the nature of the transition between the inhomogeneous and homogeneous phase of the supernova matter, self-consistently. As demonstrated in Fig. 4.5, the 3DHFEOS model allows one to move through the transition naturally, without any need for a thermodynamic construction. Thus we can explore the fingerprints of the transition.

We start by showing in Fig. 4.8 the baryonic free energy density as a function of the density for the NRAPR model and we can see that it smoothly decreases as expected. The curvature is slightly negative, which indicates a region of instability

Table 4.1: Total particle number onset densities of homogeneous matter for the interactions and temperatures studied. Results of a QMD calculation (model 2) (Sonoda et al., 2008) (only a range can be given in this case) and of TF and CP approximations to RMF with NL3 and TW Lagrangians (Avancini et al., 2012) are added for comparison. For more discussion see text.

Model	NRAPR	SQMC700	SkM*	SLy4	QMD2	NL3(TF)	NL3(CP)	TW(TF)	TW(CP)
T [MeV]					ρ[fm^{-3}]				
0	0.108	0.112	0.107	0.109	0.118-0.122	0.099	0.097	0.109	0.100
1					>0.118				
2	0.110	0.114	0.109	0.111	0.109-0.113				
3					0.101-0.105				
4	0.108	0.113	0.107	0.110	0.092-0.097				
5					0.084-0.088	0.092	0.091	0.103	0.094
6	0.100	0.105	0.100	0.102	0.080-0.084				
7					0.063-0.067	0.084	0.084	0.096	0.087
8	0.091	0.099	0.089	0.094	0.050-0.055	0.078	0.079	0.091	0.082
9					0.034-0.038				
10	0.075	0.079	0.074	0.077					

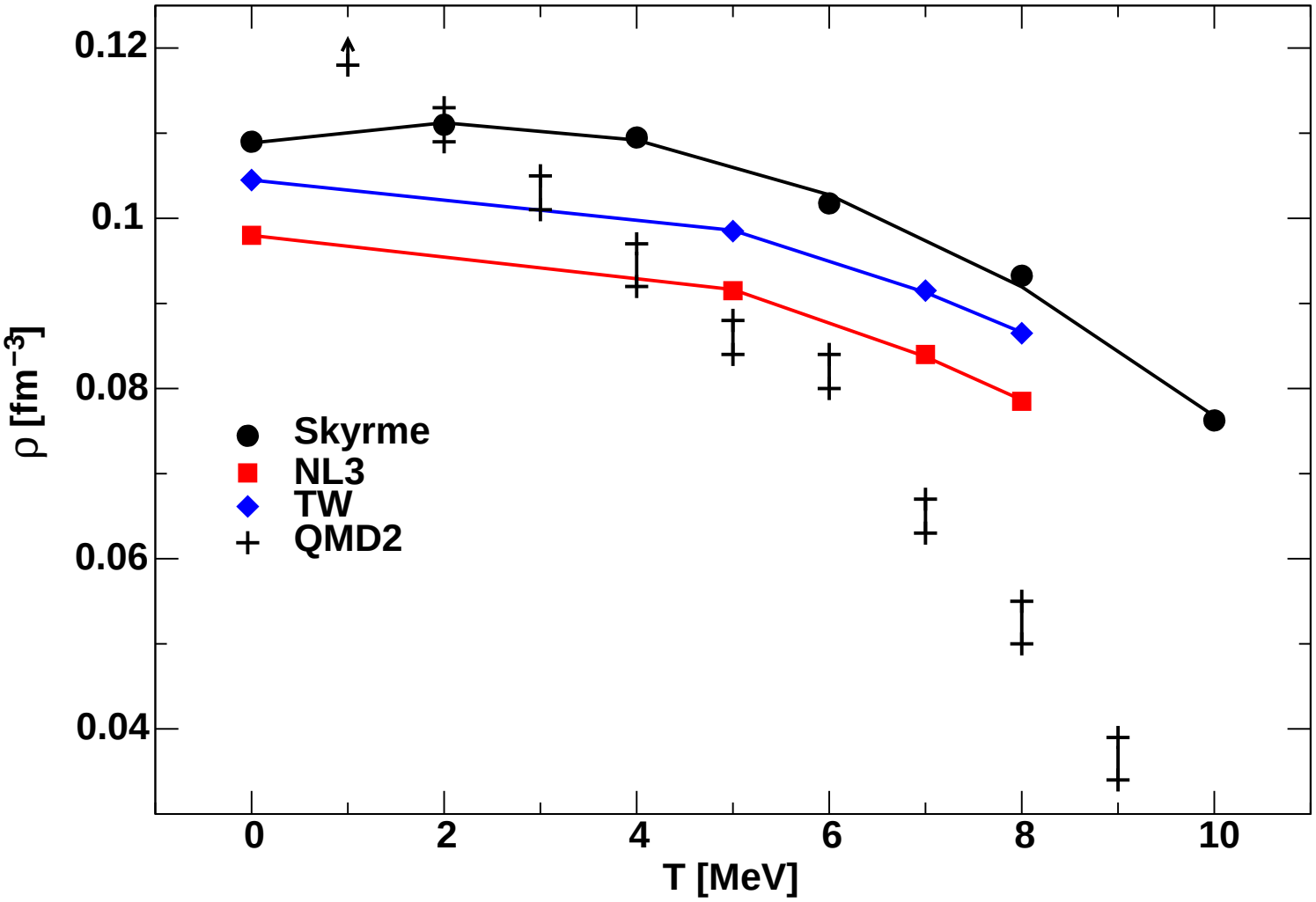

Figure 4.7: Temperature dependence on the onset density of homogeneous matter, as predicted by the Skyrme, RMF (NL3, TW) and QMD2 models. Values for QMD2 model are given as a range; the arrow shows that the entry is a lower limit. The lines are added to guide the eye. For more details see text.

Table 4.2: Symmetric nuclear matter properties at saturation density ρ_0 (energy per particle B/A, incompressibility K, symmetry energy E_{sym} and symmetry energy slope L) for the models shown in Tab. 4.1. All the quantities are in MeV, except for ρ_0, given in fm^{-3}.

Model	ρ_0	B/A	K	E_{sym}	L
NRAPR	0.16	-15.85	226	33	60
SQMC700	0.17	-15.49	222	33	59
SkM*	0.16	-15.77	217	30	46
SLy4	0.16	-15.97	230	32	46
QMD2	0.17	-16	280	33	80
NL3	0.15	-16.3	272	37	118
TW	0.15	-16.3	240	33	55

below ~ 0.11 fm^{-3}, i.e., where the pasta appears (Müller and Serot, 1995). The other interactions follow the same trend.

To determine the phase transition and the densities at which it occurs, let us employ a Gibbs construction to illustrate the method. We start by considering the pressure as a function of the baryonic chemical potential, and we show that construction for a RMF model, NL3 (Lalazissis et al., 1997), for homogeneous matter (see top panel of Fig. 4.9) as well. For a constant temperature, and according to the Gibbs conditions, the transition occurs when $P_1(\mu_{b_1}) = P_2(\mu_{b_2})$.

For NL3, the chemical potential at which the transition occurs corresponds to the crossing of the dashed line and full line at $\sim$ 1836 MeV. For the NRAPR Skyrme interaction, we show our pasta calculations and conclude that the critical chemical potential is probably close to minimum for $\mu_b = 1831.82$ MeV. We should recall that contrary to the phase transition built from the homogeneous EOS, with a first order phase transition between a low density gas and a high density liquid, the pasta calculation takes into account both finite effects and the Coulomb interaction. It is seen that negative baryonic pressures are obtained. However, when the total pressure, including the electron contribution, is considered there are no negative pressures (see Fig. 4.12). Similar conclusions have been discussed in Tatsumi et al. (2011), however for a calculation done for symmetric matter within a TF calculation.

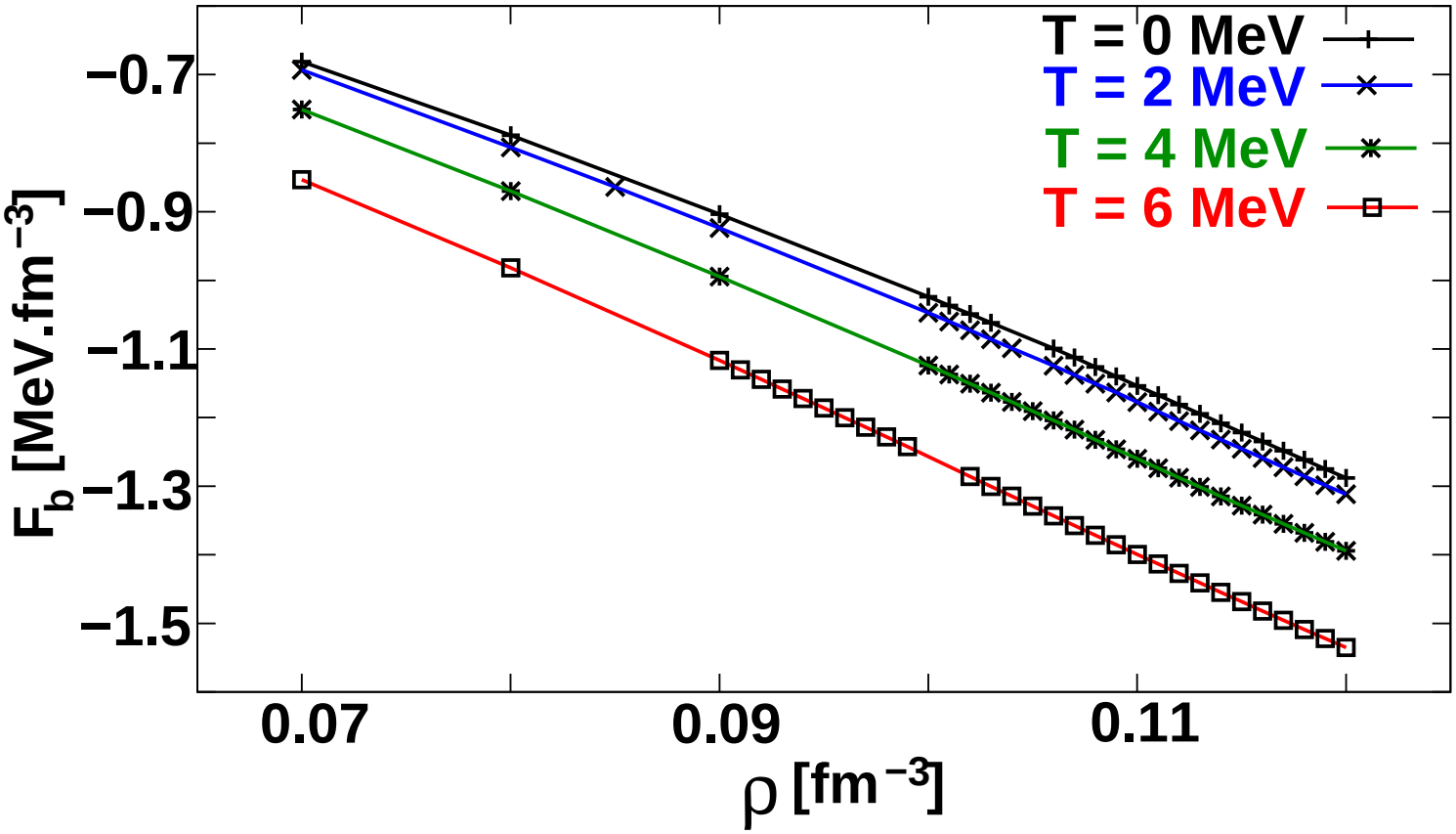

Figure 4.8: Baryonic free energy density as a function of the number density for the NRAPR Skyrme interaction and $T = 0, 2, 4$ and 6 MeV.

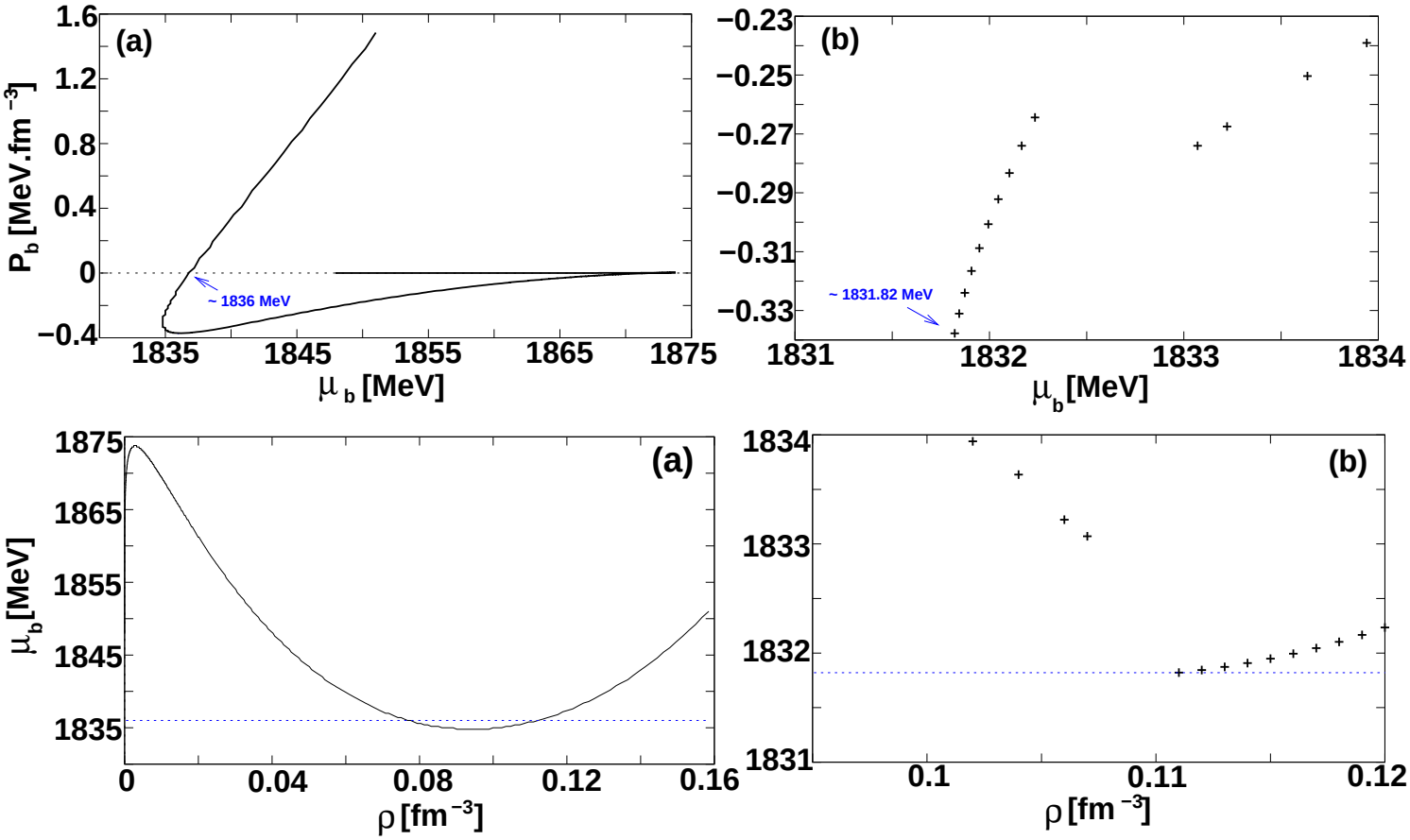

Figure 4.9: Top panel: Baryonic pressure as a function of baryon chemical potential; Bottom panel: Baryonic chemical potential as a function of the density for the NL3 model (a) and the NRAPR Skyrme interaction (b), at $T = 2$ MeV.

To determine the densities at which the transition occurs, we plot the baryonic chemical potential as a function of the density — see lower panel of Fig. 4.9. The horizontal lines shown indicate the baryonic chemical potential at which the transition occurs, limiting a region of densities where an instability phase appears (for the NL3 model), and a point where the transition happens, for the NRAPR model. For this model, the pasta phase region of densities corresponds to the left branch, and for the NL3 model it should occur within the transition density, in the $\mu_b(\rho)$ plot. For NRAPR, the right branch corresponds to the uniform matter phase.

We illustrate this discontinuity for the NRAPR Skyrme interaction in Figs. 4.10, 4.11, 4.12 and 4.13 for the baryonic chemical potential and in Figs. 4.15, 4.17, 4.16 and 4.18 for the baryonic entropy density. The same pattern is seen for all the other three Skyrme models.

In Figs. 4.10 and 4.11, we show the baryonic pressure and the baryonic free energy density as a function of the baryonic chemical potential for the other temperatures, $T = 0, 2, 4$ and 6 MeV. The baryonic chemical potential for the transition to uniform matter corresponds to the minimum (local maximum) of the P_b (F_b) curves.

In Figs. 4.12 and 4.13, we plot the total pressure and free energy density as a function of the baryonic chemical potential. The transition is once more shown, this time corresponding to the minimum of both curves.

We can see in Figures 4.12 and 4.13 that both the total pressure and free energy density increase with μ_B in the uniform matter phase, whereas for the pasta phase the opposite happens. When we compare with the baryonic pressure and free energy density (see Figures 4.10 and 4.11), we find that P_b also increases after the transition, but for the pasta phase, P_b increases with μ_b as well. F_b decreases in the uniform matter and increases in the pasta phase. These are all expected results for stable matter (positive incompressibility, or positive derivative of P with respect to ρ): for uniform matter at high densities, P should increase with the density. In a similar way, for the pasta phase (lower densities), P should decrease with decreasing densities, as it can be seen in Fig. 4.14. A comment on the difference between P_b and P_t should

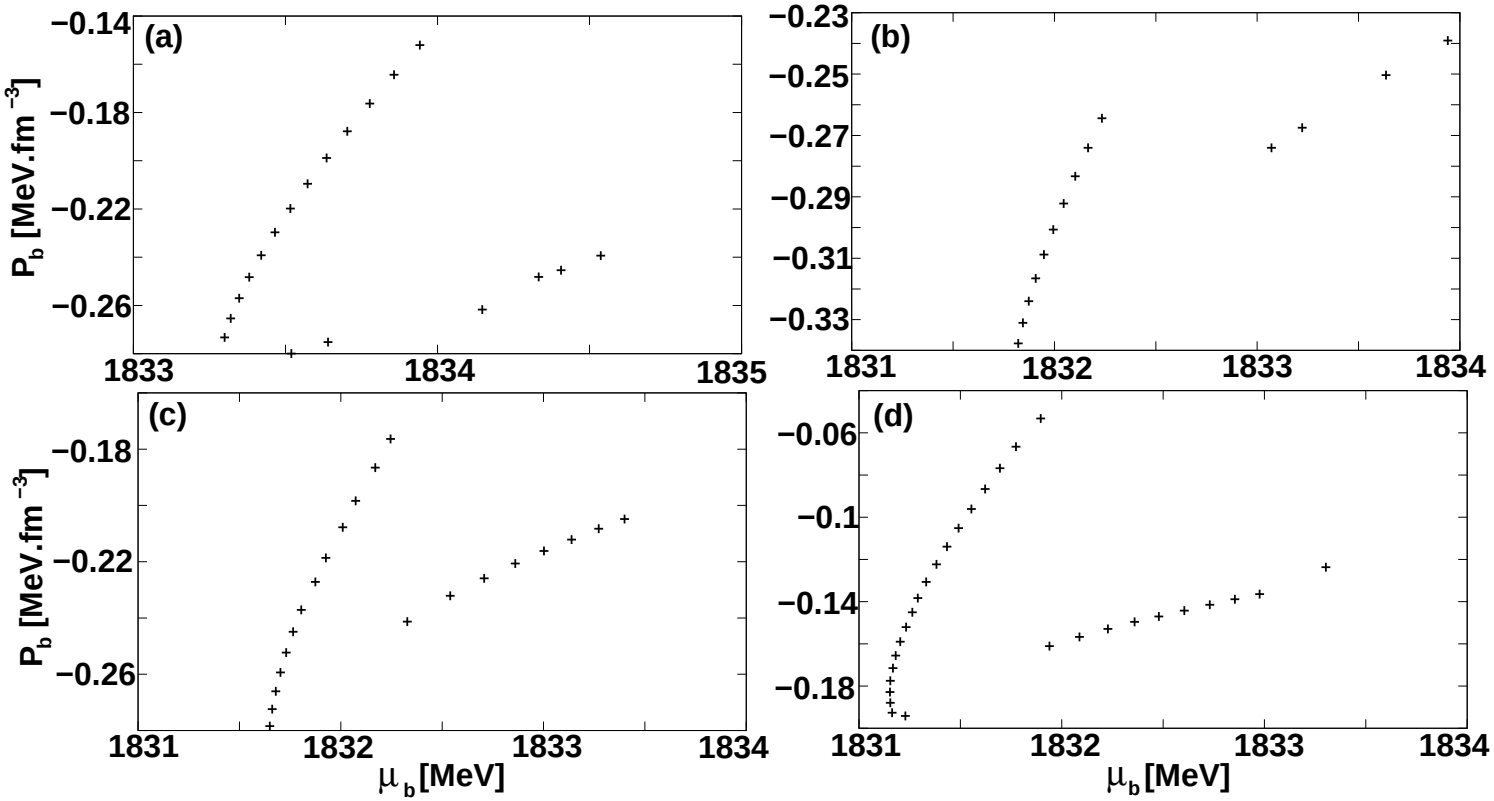

Figure 4.10: Baryon pressure as a function of baryon chemical potential for the NRAPR Skyrme interaction and (a) $T = 0$, (b) $T = 2$, (c) $T = 4$, and (d) $T = 6$ MeV. Left branch: uniform matter; Right branch: pasta phase.

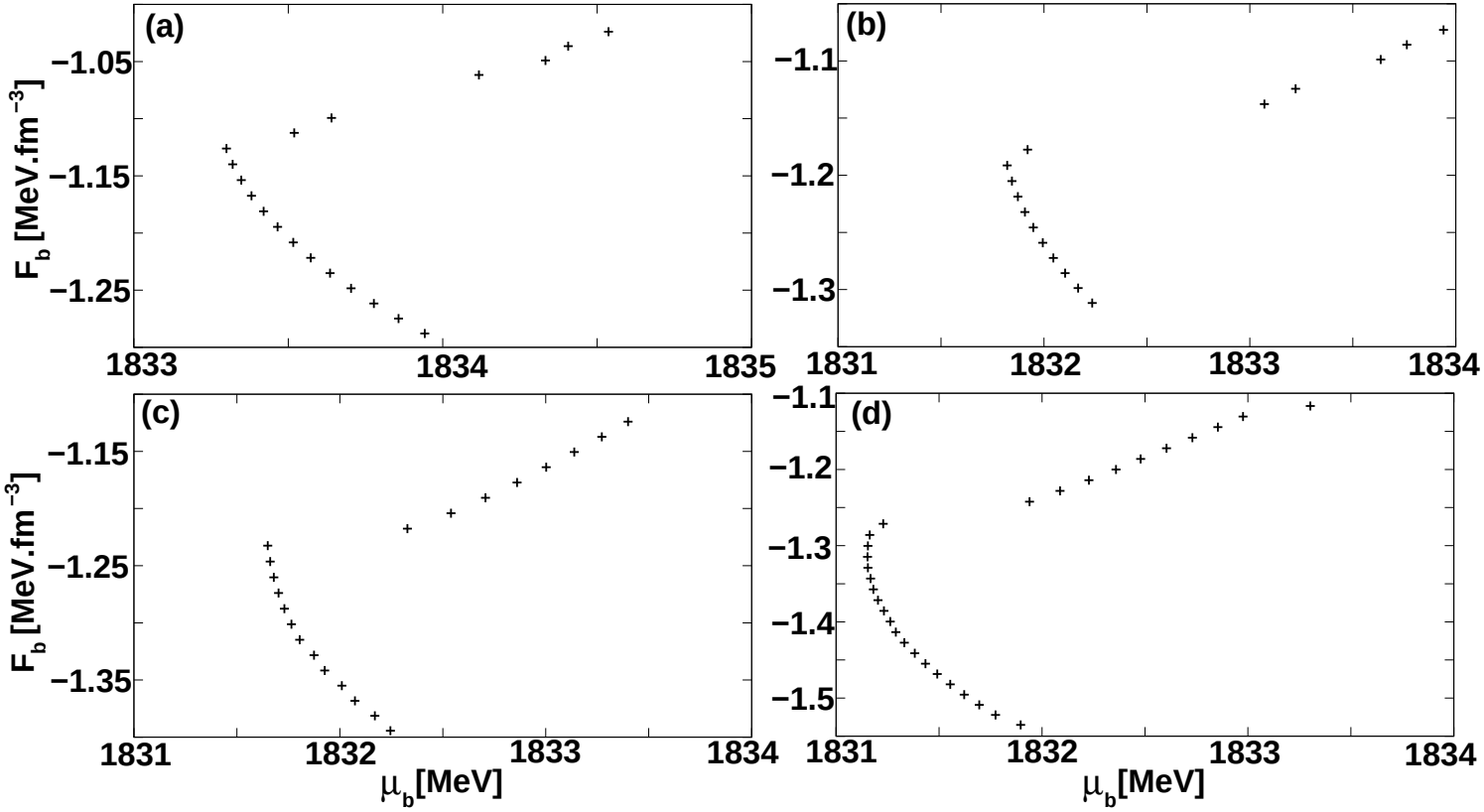

Figure 4.11: Baryon free energy density as a function of baryon chemical potential for the NRAPR Skyrme interaction and (a) $T = 0$, (b) $T = 2$, (c) $T = 4$, and (d) $T = 6$ MeV. Left branch: uniform matter; Right branch: pasta phase.

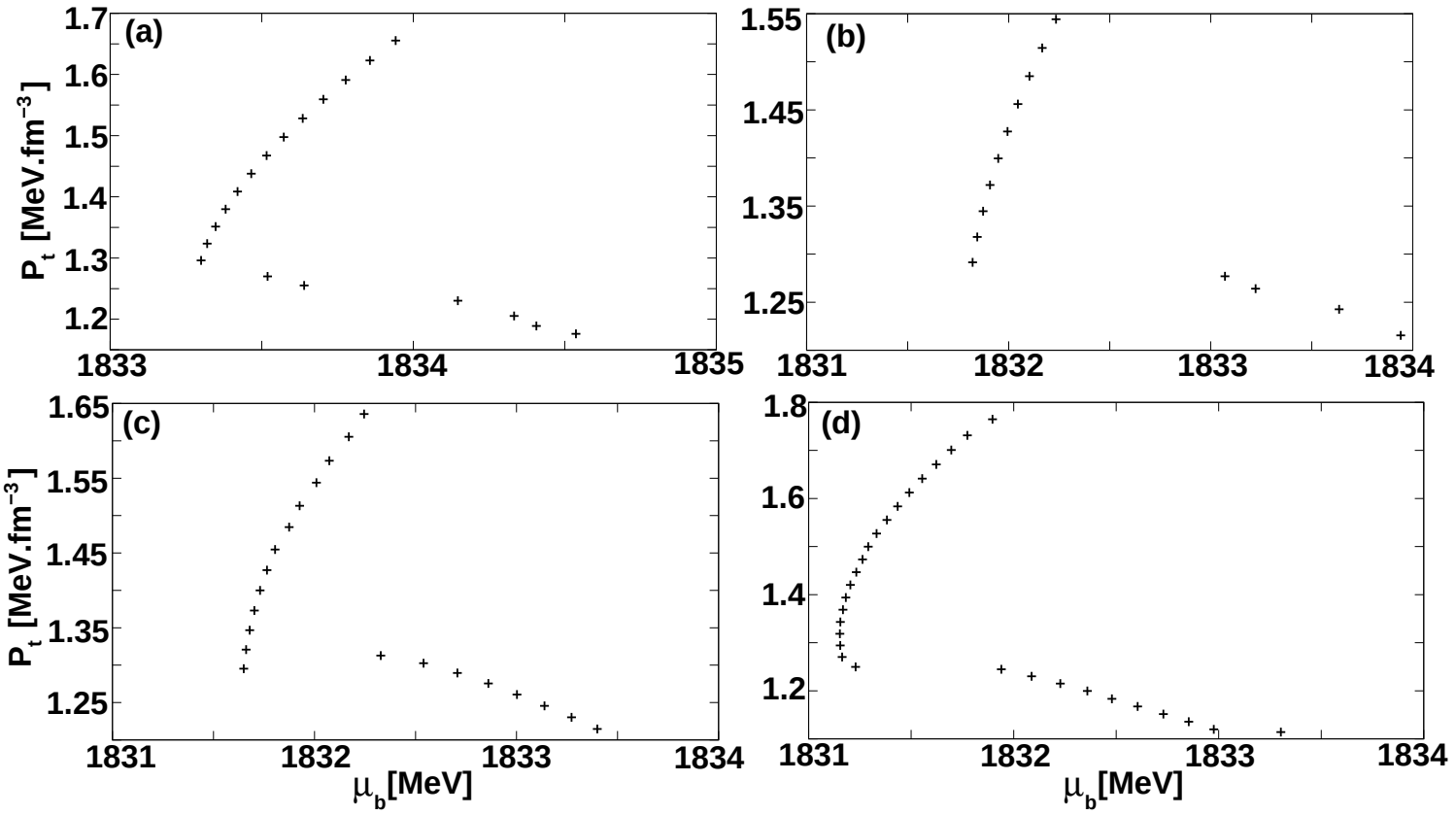

Figure 4.12: Total pressure as a function of baryon chemical potential for the NRAPR Skyrme interaction and (a) $T = 0$, (b) $T = 2$, (c) $T = 4$, and (d) $T = 6$ MeV. Left branch: uniform matter; Right branch: pasta phase.

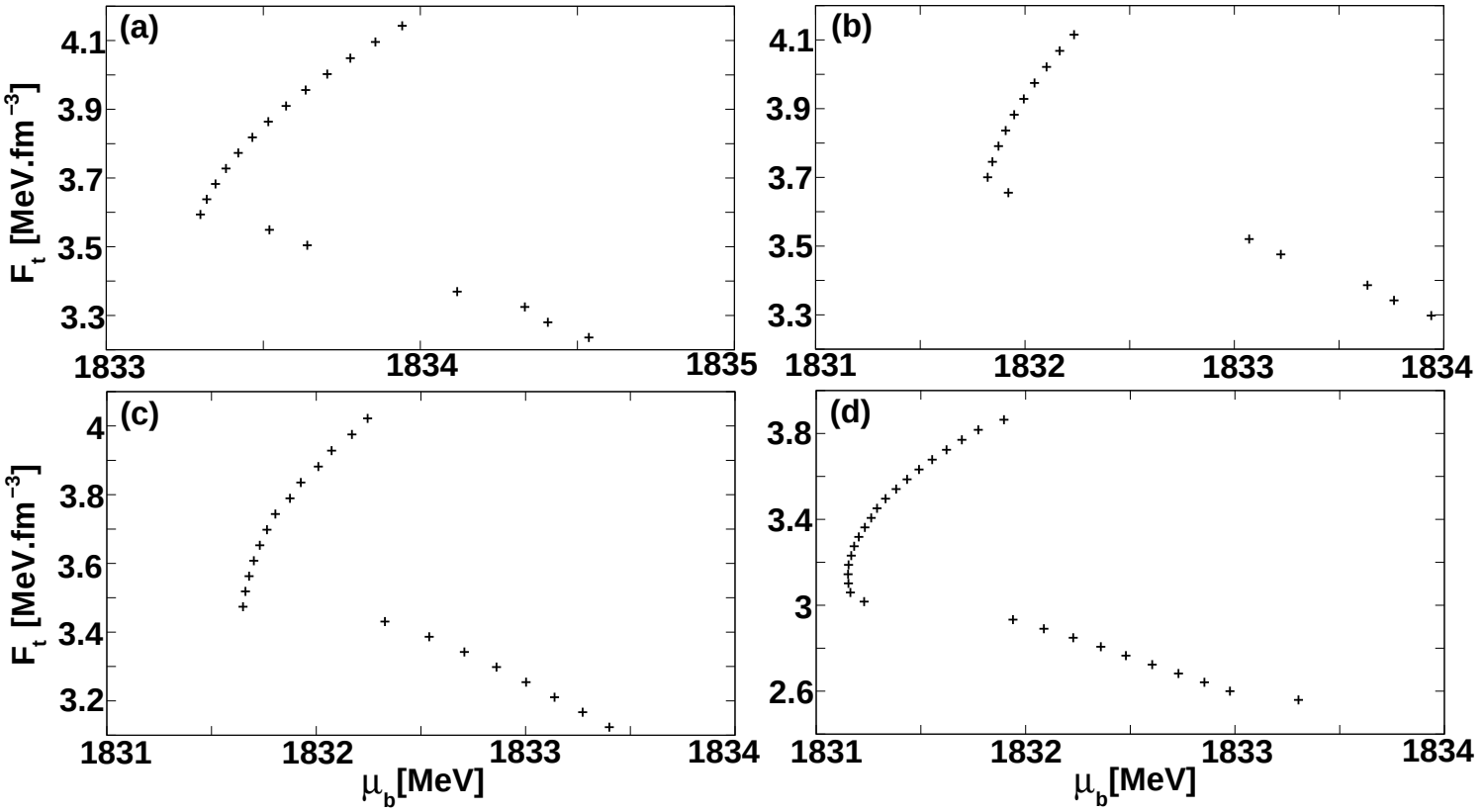

Figure 4.13: Total free energy density as a function of baryon chemical potential for the NRAPR Skyrme interaction and (a) $T = 0$, (b) $T = 2$, (c) $T = 4$, and (d) $T = 6$ MeV. Left branch: uniform matter; Right branch: pasta phase.

also be made: electrons are much more incompressible, which explains the difference in behaviour in the pasta phase: P_t decreases and P_b increases.

In Fig. 4.14, we plot the total pressure as a function of the density. The transition to uniform matter is marked by the discontinuity in the density, as we saw before in Fig. 4.5.

In Figures 4.15 and 4.17, P_t and F_t increase with S_b, in both phases, whereas for P_b and F_b the opposite happens: they both decrease with increasing S_b, as we can observe in Figs. 4.16 and 4.18. This behaviour is also expected as the entropy increases with increasing density and temperature.

In Fig 4.19, 4.20, 4.21 and 4.22 we plot the baryonic chemical potential and in Figs. 4.23, 4.24, 4.25 and 4.26, we plot the baryonic entropy density as a function of the density, where the transition densities for all the interactions and temperatures are clearly shown. We are using the same procedure as above and the transition densities correspond to the minimum (local maximum) of the chemical potential (entropy) curves.

In Figs. 4.27, 4.28, 4.29, and 4.30, this discontinuity is again seen when we plot the baryonic entropy density as a function of the baryonic chemical potential, for all the interactions and temperatures considered.

We see that there is a prominent discontinuity in pressure, chemical potential and entropy, indicating unambiguously that the transition between the pasta phase and homogeneous (uniform) matter is a first order phase transition.

Williams and Koonin (1985) also found first-order phase transitions between shapes and to uniform matter marked by discontinuities in the pressure and chemical potential. In our model, the discontinuities in the first derivatives of the free energy density at lower densities are too small to be identified and probably go beyond the numerical capability of the code, not allowing us to clearly identify the character of the transition between shapes. Lamb et al. (1983) also found a first-order phase transition to uniform matter but they note that if the Coulomb energy would be turned off, the transition would be second order.

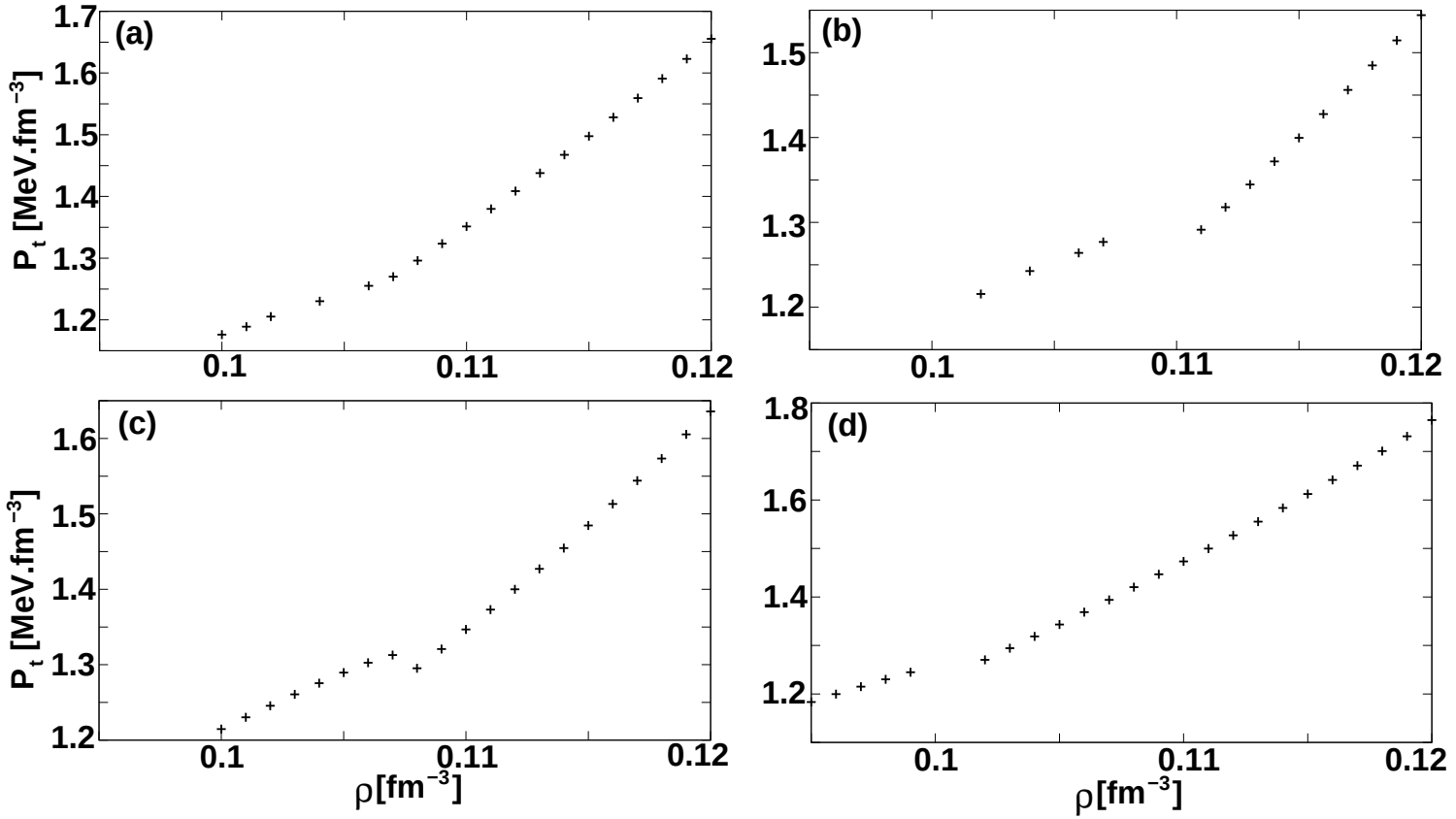

Figure 4.14: Total pressure as a function of the density for the NRAPR Skyrme interaction and (a) $T = 0$, (b) $T = 2$, (c) $T = 4$, and (d) $T = 6$ MeV. Left branch: pasta phase; Right branch: uniform matter.

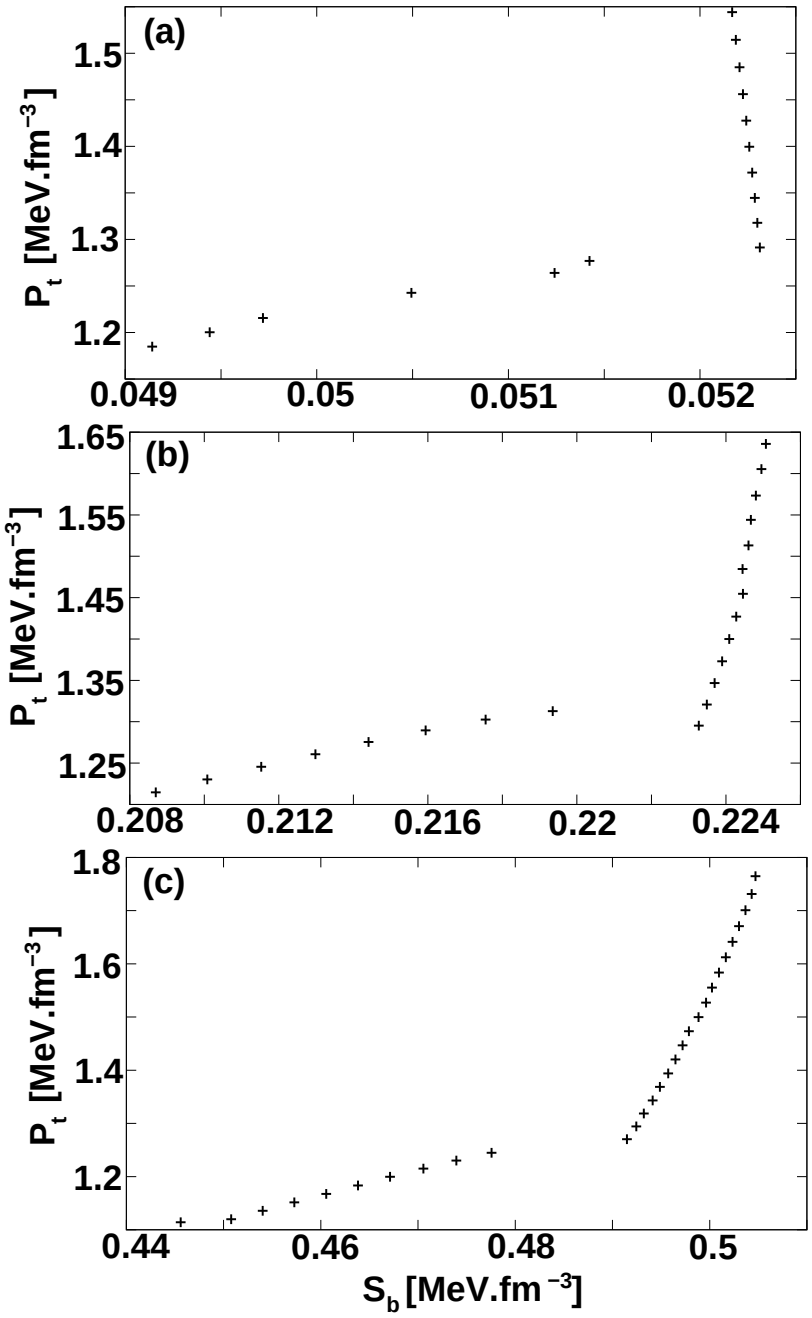

Figure 4.15: Total pressure as a function of baryonic entropy density for the NRAPR Skyrme interaction and (a) $T = 2$, (b) $T = 4$, and (c) $T = 6$ MeV.

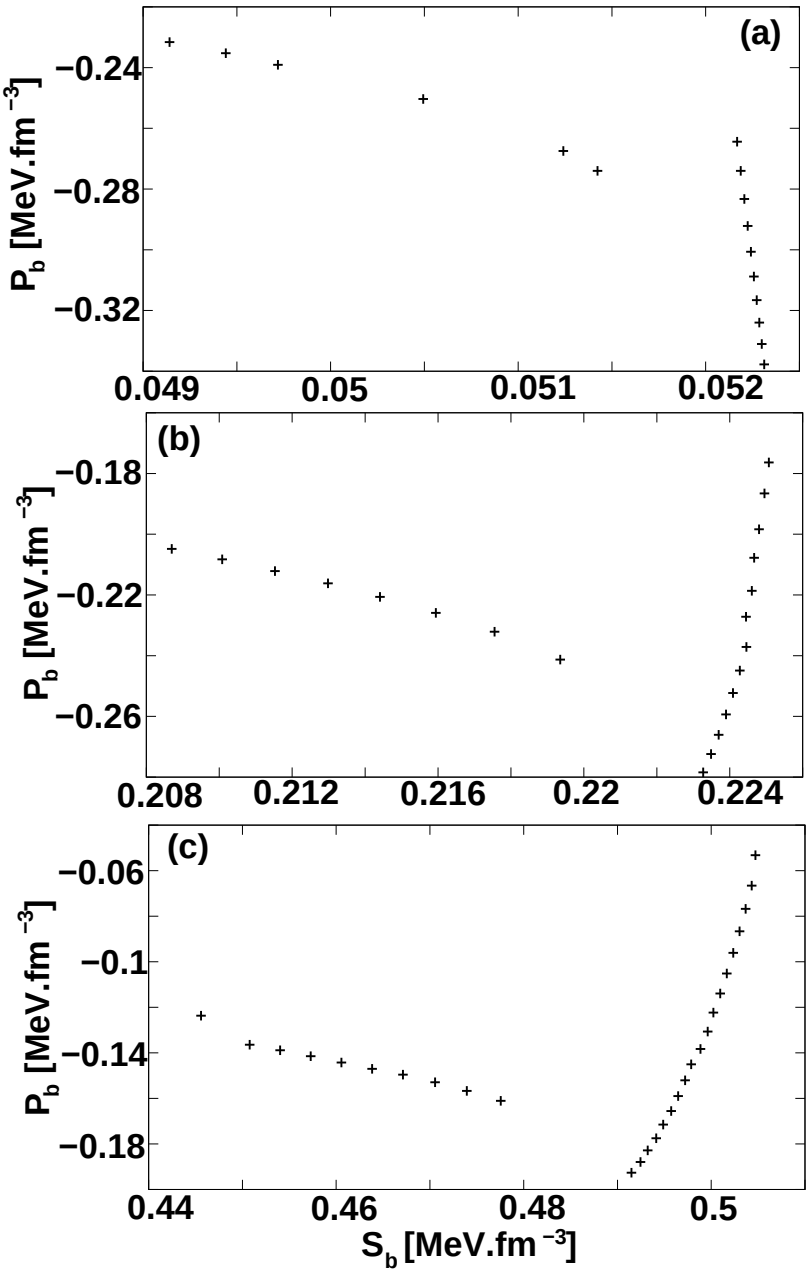

Figure 4.16: Baryonic pressure as a function of baryonic entropy density for the NRAPR Skyrme interaction and (a) $T = 2$, (b) $T = 4$, and (c) $T = 6$ MeV.

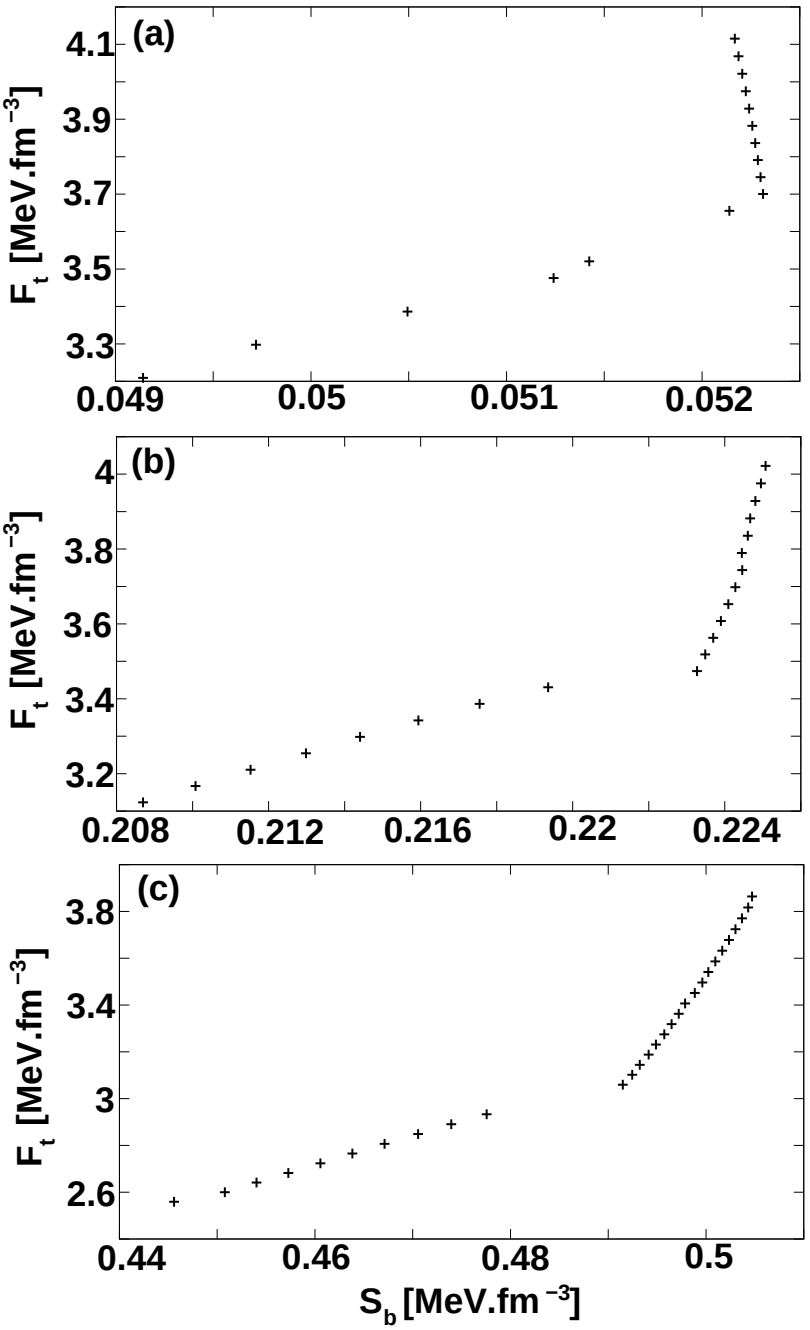

Figure 4.17: Total free energy density as a function of baryonic entropy density for the NRAPR Skyrme interaction and (a) $T = 2$, (b) $T = 4$, and (c) $T = 6$ MeV.

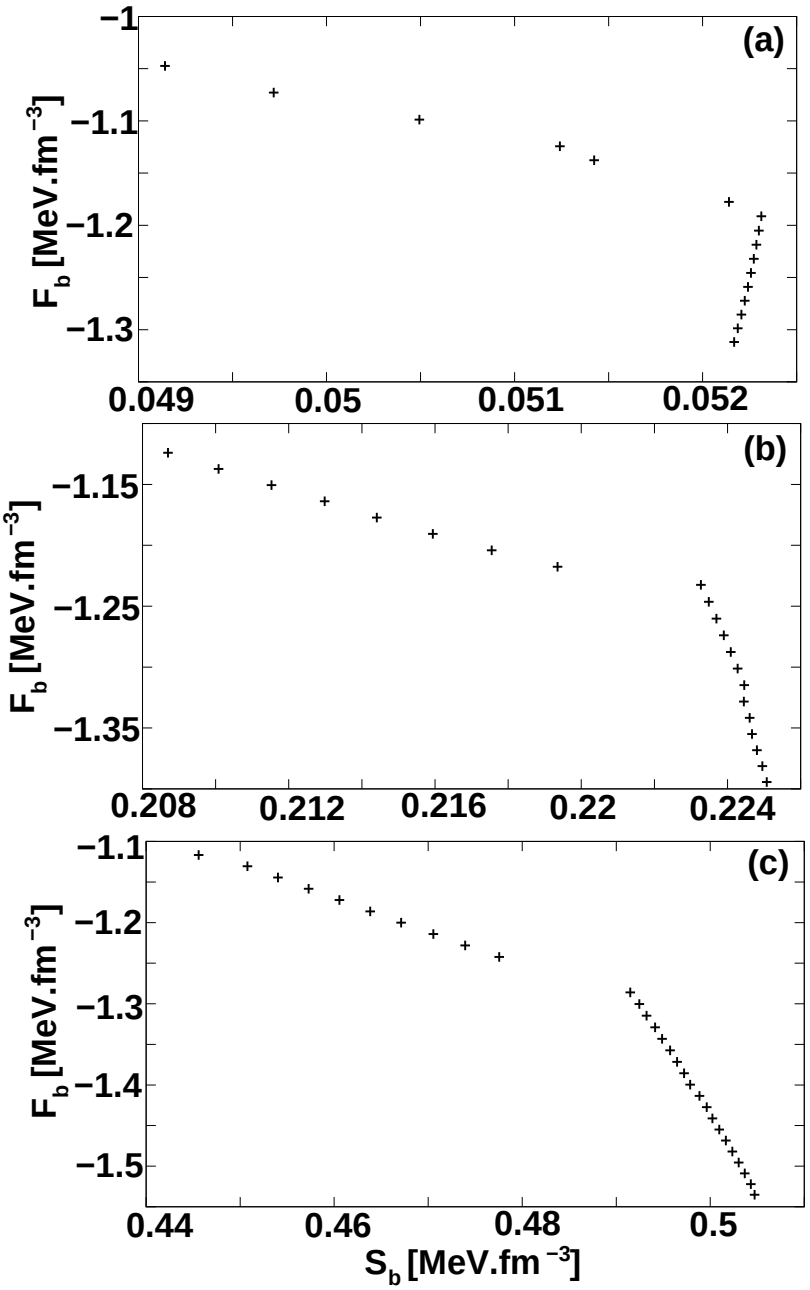

Figure 4.18: Baryonic free energy density as a function of baryonic entropy density for the NRAPR Skyrme interaction and (a) $T = 2$, (b) $T = 4$, and (c) $T = 6$ MeV.

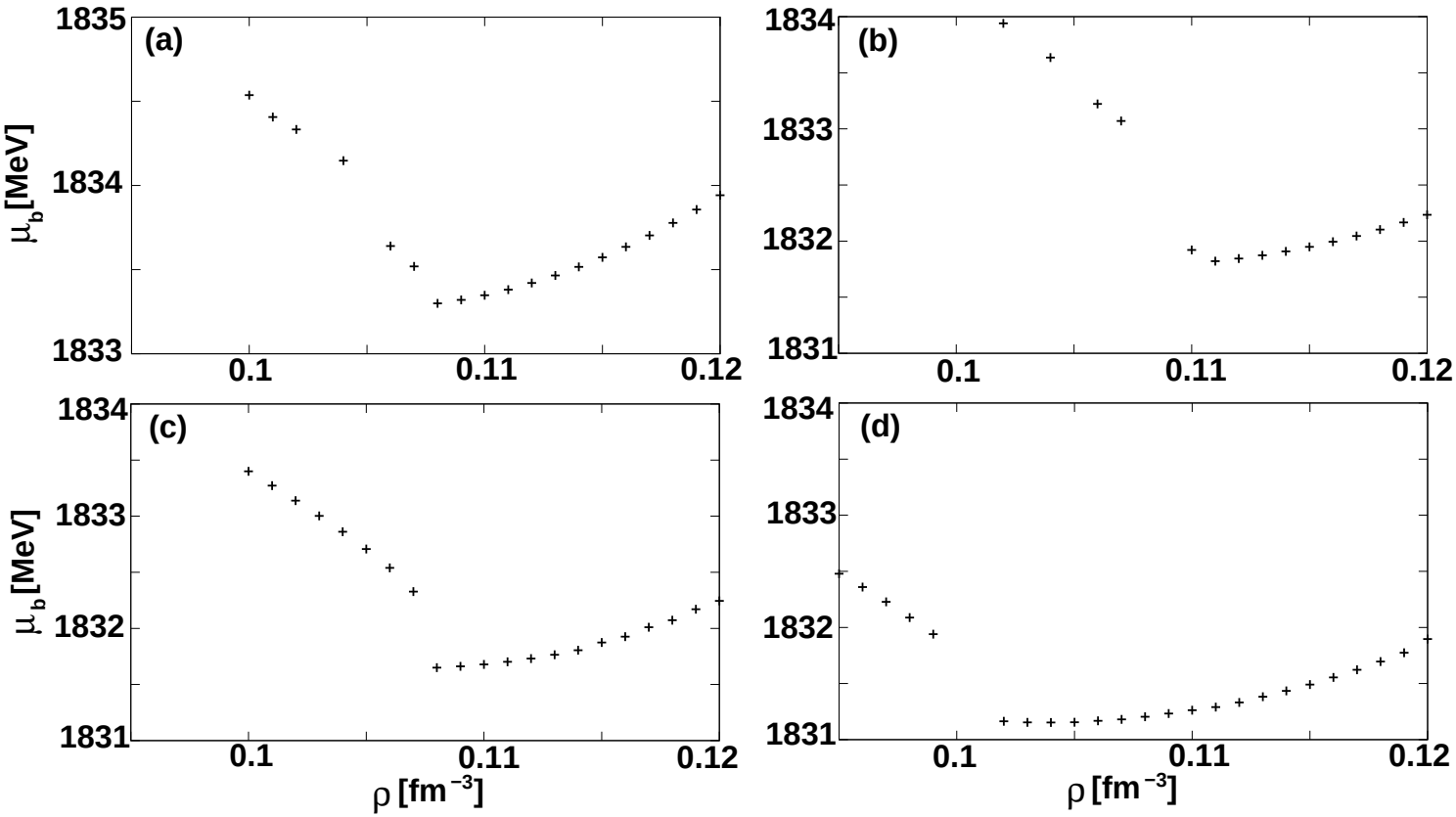

Figure 4.19: Baryonic chemical potential as a function of number density for the NRAPR Skyrme interaction and (a) $T = 0$, (b) $T = 2$, (c) $T = 4$, and (d) $T = 6$ MeV. Left branch: pasta phase; Right branch: uniform matter.

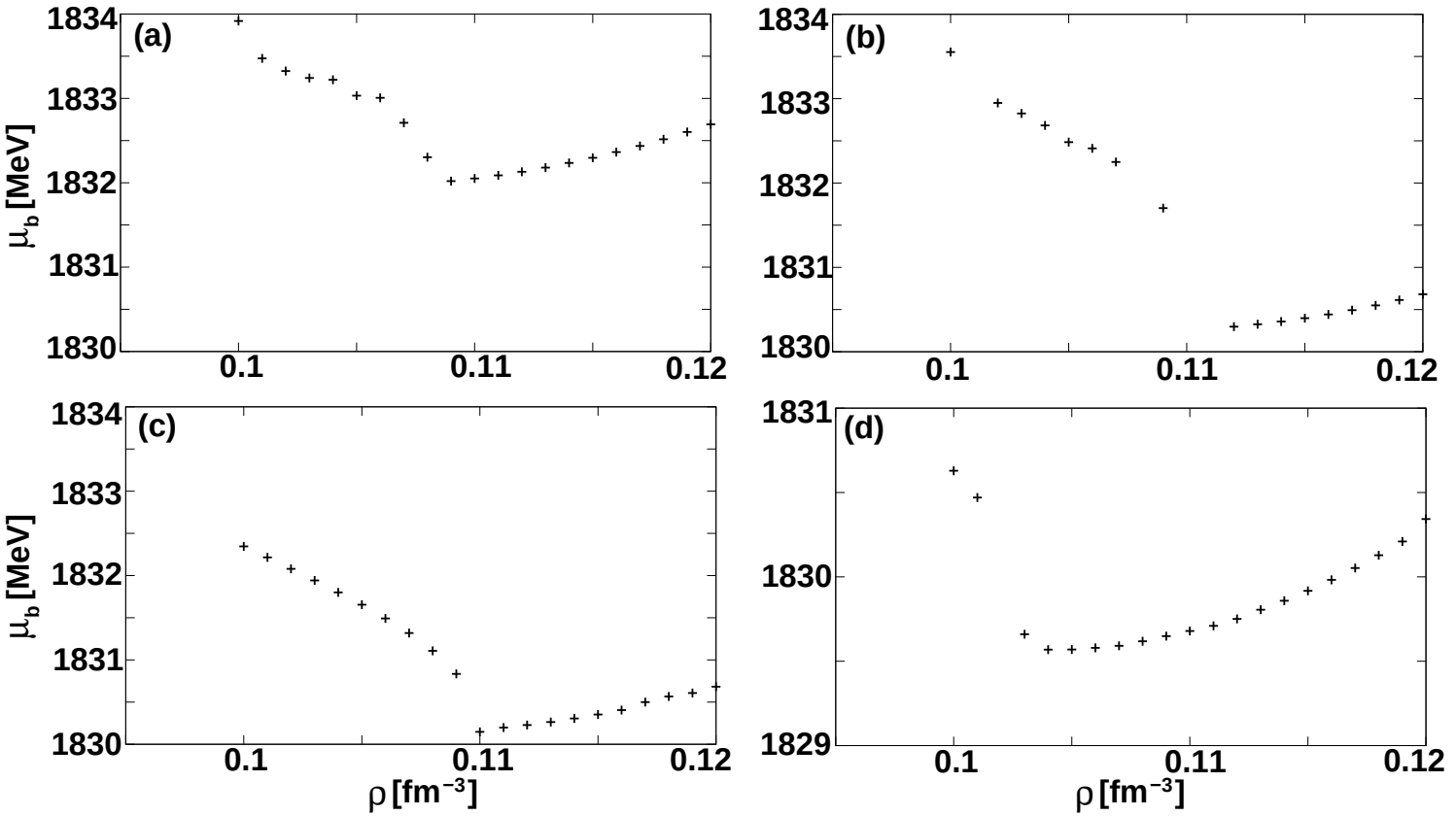

Figure 4.20: Baryonic chemical potential as a function of number density for the SLy4 Skyrme interaction and (a) $T = 0$, (b) $T = 2$, (c) $T = 4$, and (d) $T = 6$ MeV. Left branch: pasta phase; Right branch: uniform matter.

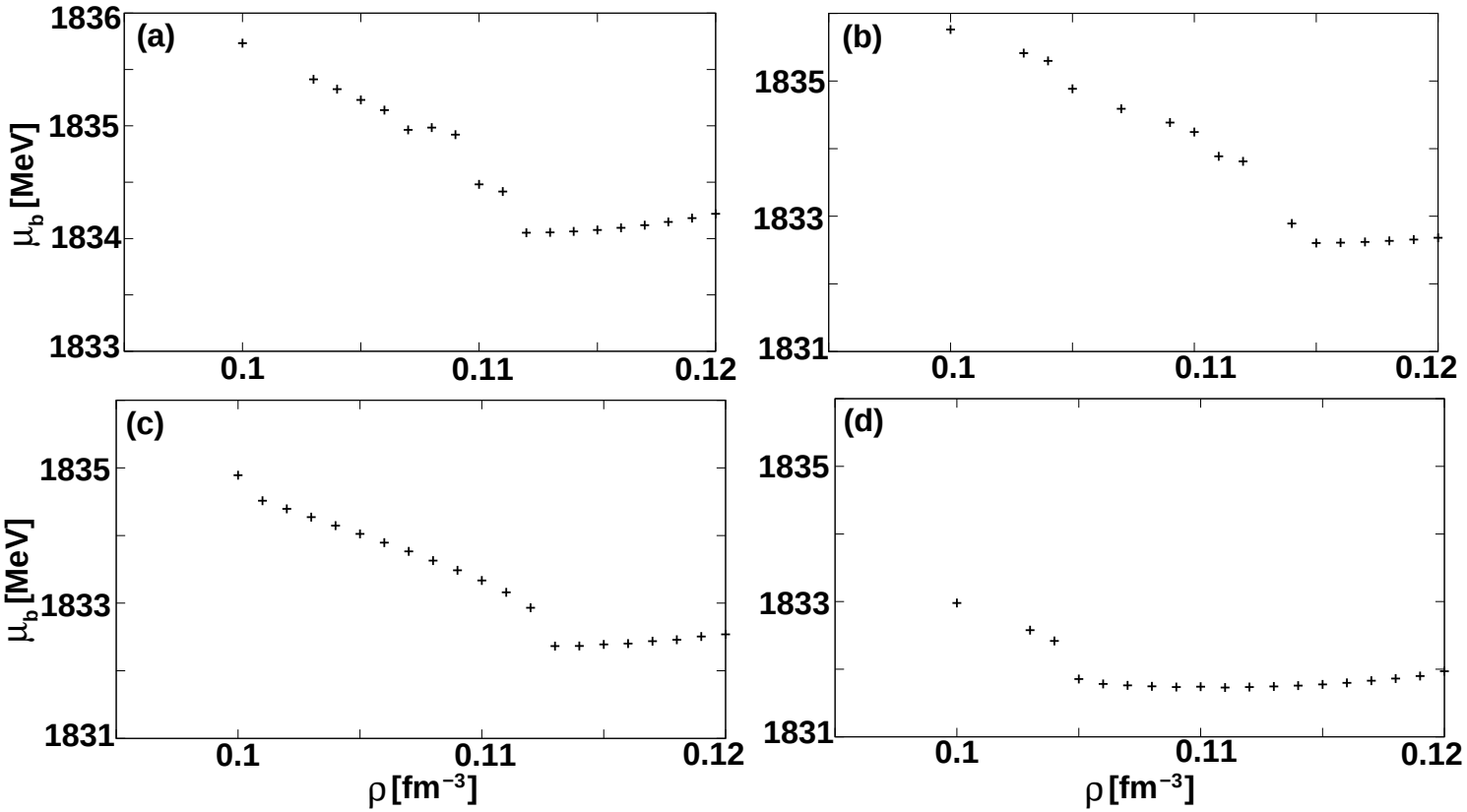

Figure 4.21: Baryonic chemical potential as a function of number density for the QMC Skyrme interaction and (a) $T = 0$, (b) $T = 2$, (c) $T = 4$, and (d) $T = 6$ MeV. Left branch: pasta phase; Right branch: uniform matter.

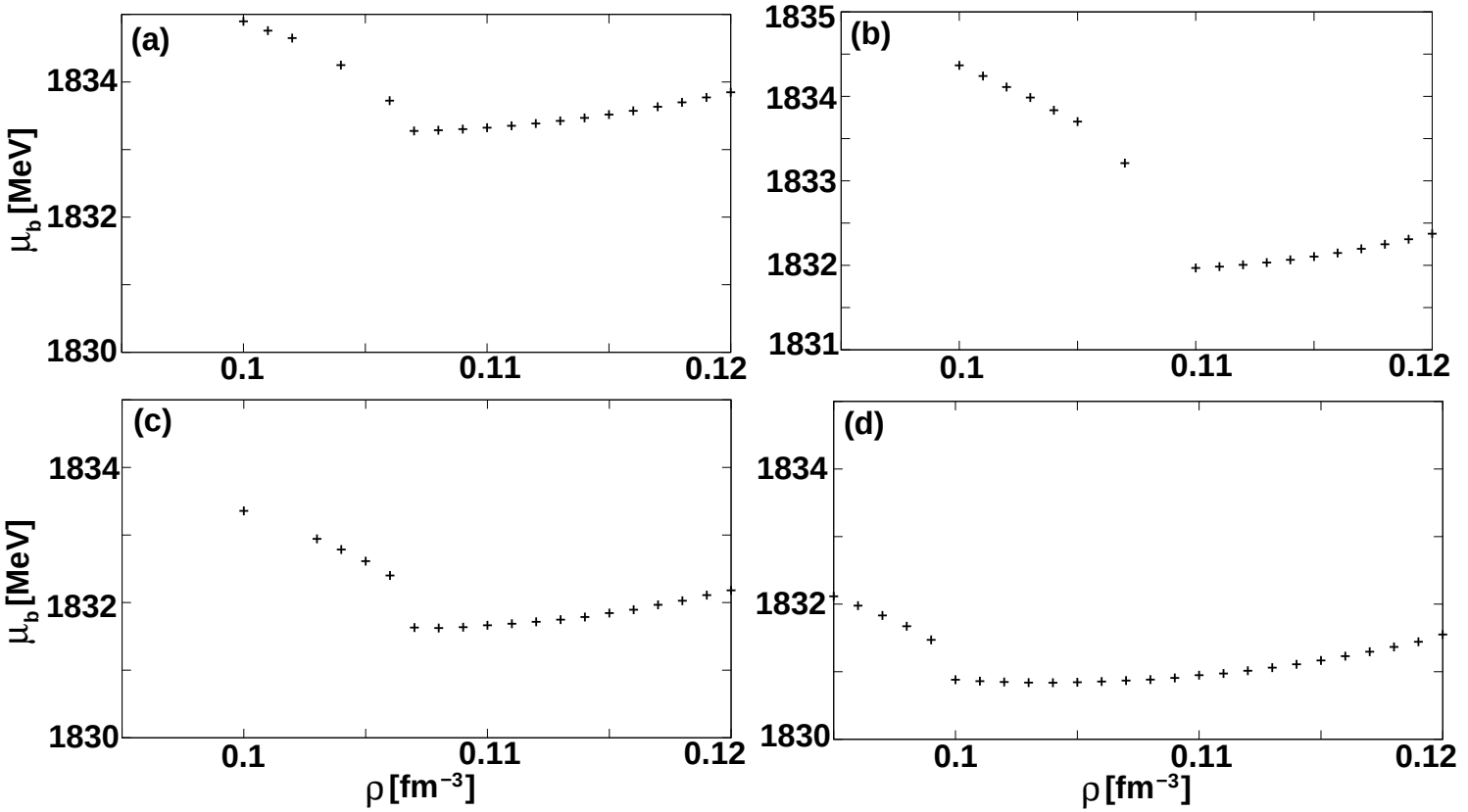

Figure 4.22: Baryonic chemical potential as a function of number density for the SkM* Skyrme interaction and (a) $T = 0$, (b) $T = 2$, (c) $T = 4$, and (d) $T = 6$ MeV. Left branch: pasta phase; Right branch: uniform matter.

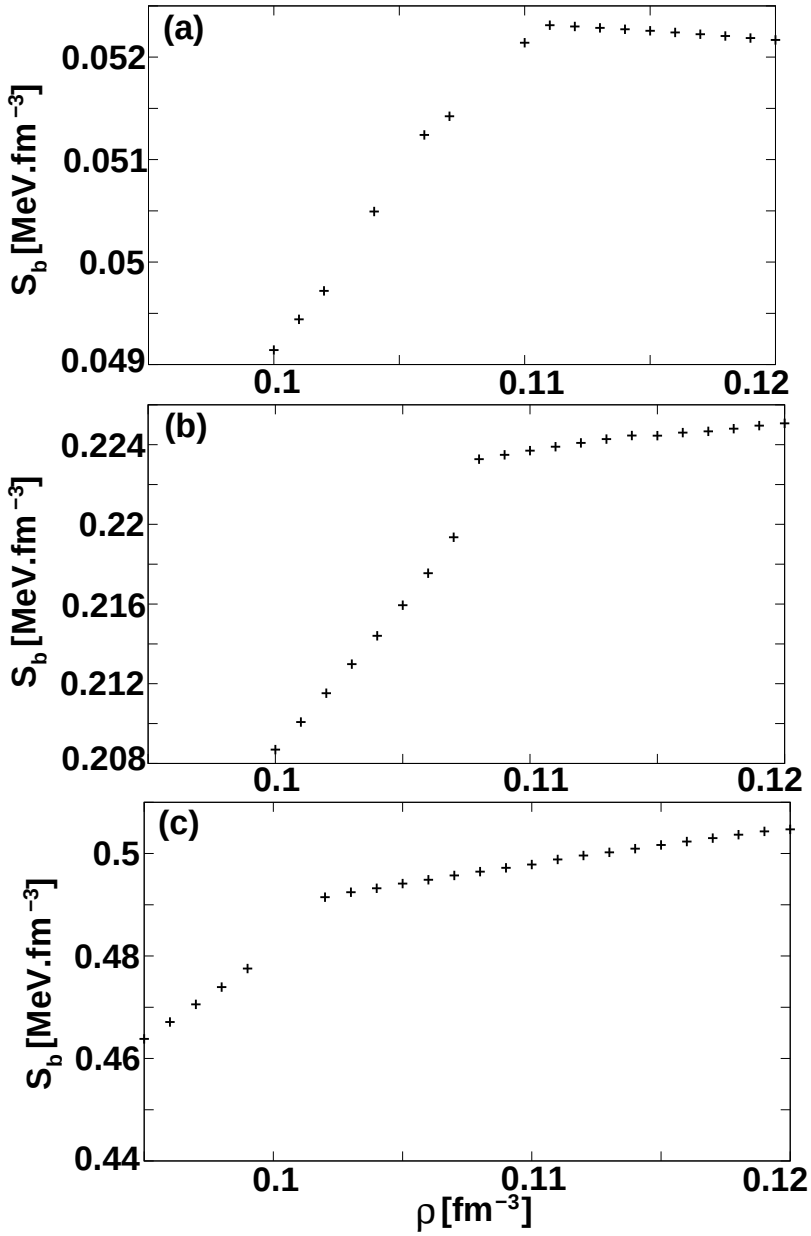

Figure 4.23: Baryonic entropy density as a function of number density for the NRAPR Skyrme interaction and (a) $T = 2$, (b) $T = 4$, and (c) $T = 6$ MeV. Left branch: pasta phase; Right branch: uniform matter.

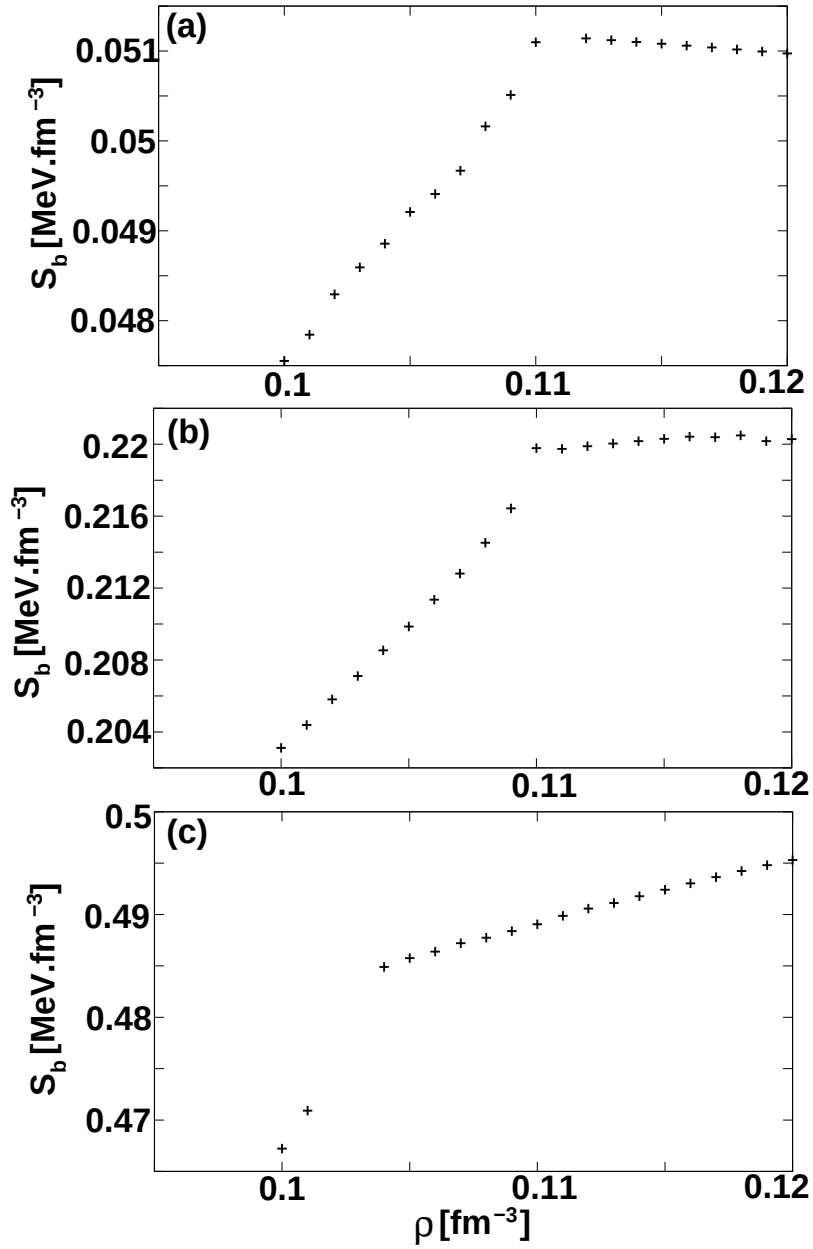

Figure 4.24: Baryonic entropy density as a function of number density for the SLy4 Skyrme interaction and (a) $T = 2$, (b) $T = 4$, and (c) $T = 6$ MeV. Left branch: pasta phase; Right branch: uniform matter.

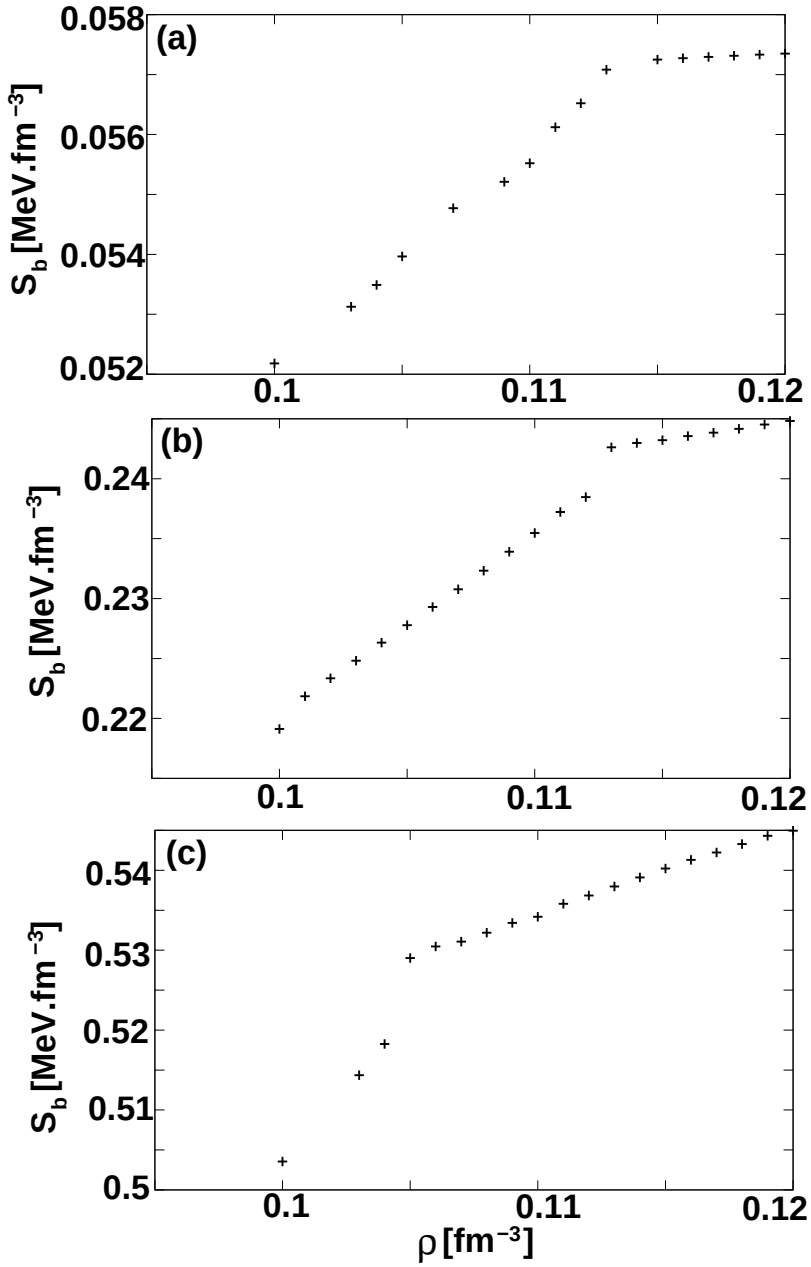

Figure 4.25: Baryonic entropy density as a function of number density for the QMC Skyrme interaction and (a) $T = 2$, (b) $T = 4$, and (c) $T = 6$ MeV. Left branch: pasta phase; Right branch: uniform matter.

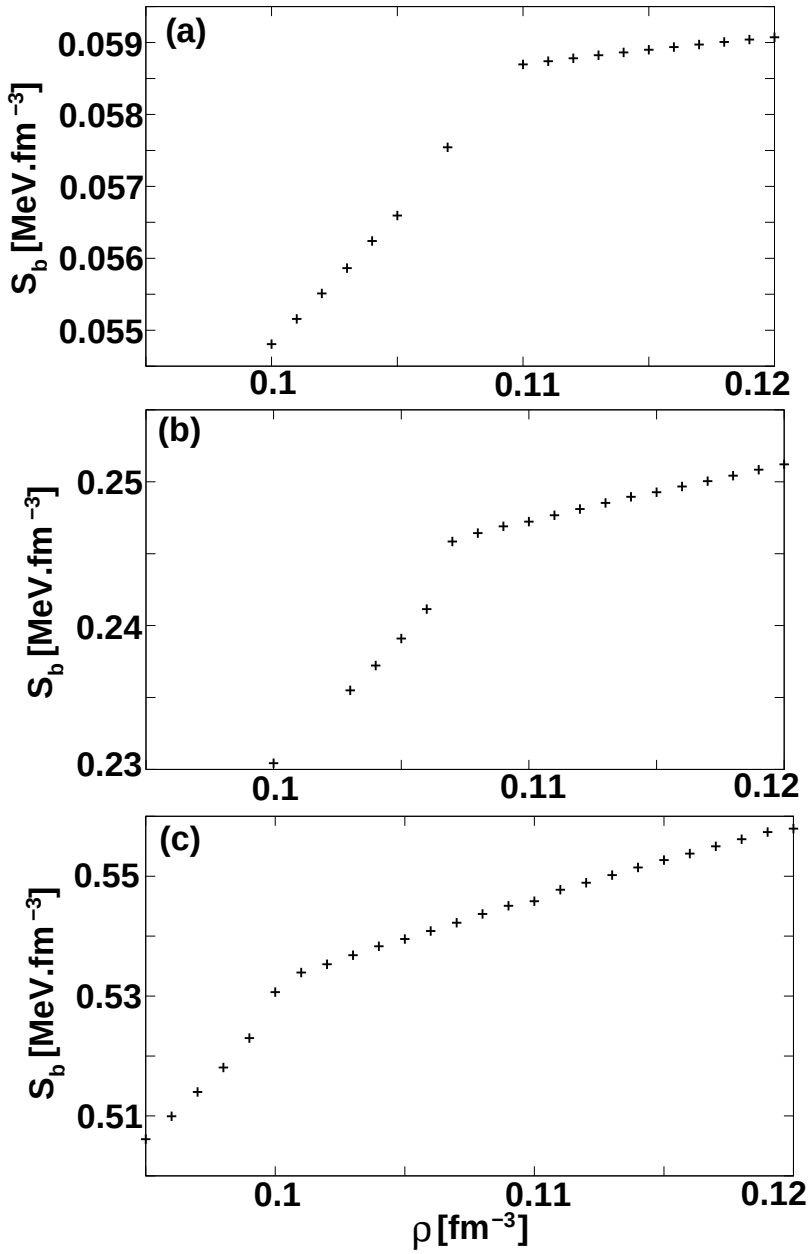

Figure 4.26: Baryonic entropy density as a function of number density for the SkM* Skyrme interaction and (a) $T = 2$, (b) $T = 4$, and (c) $T = 6$ MeV. Left branch: pasta phase; Right branch: uniform matter.

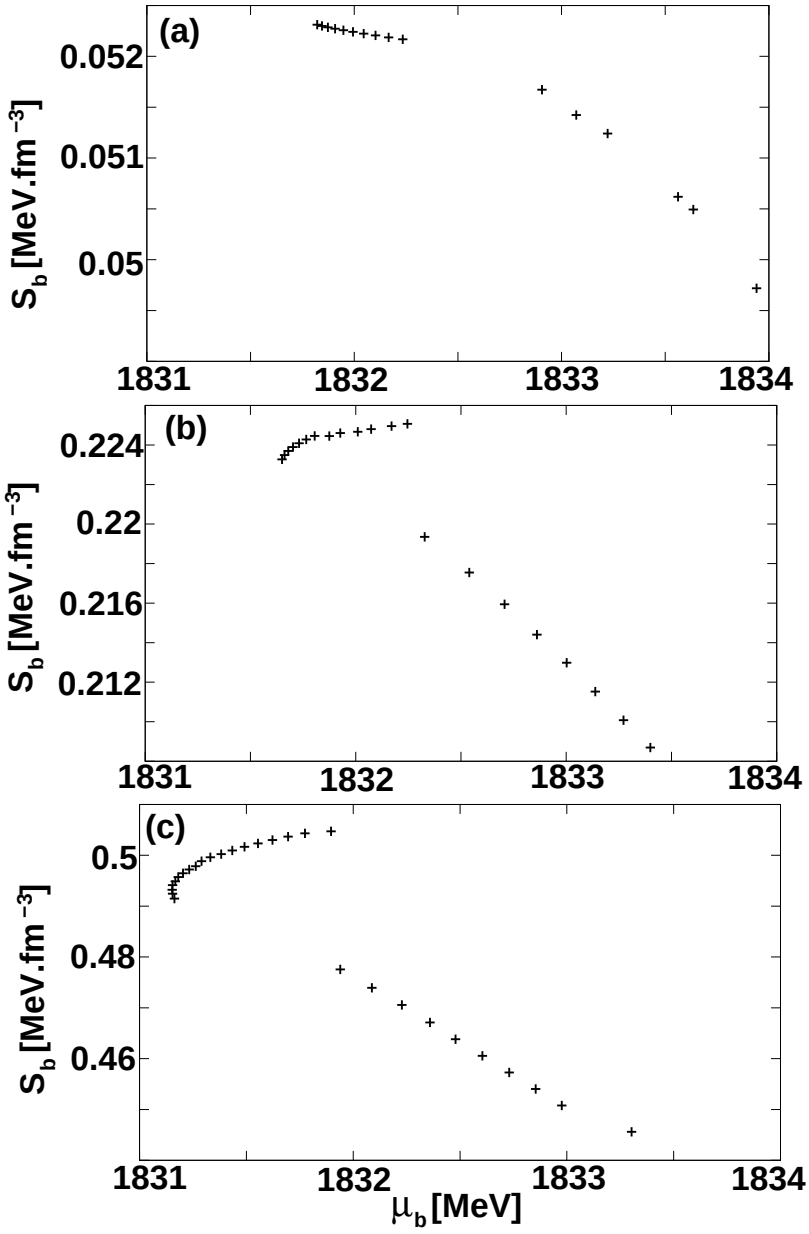

Figure 4.27: Baryonic entropy density as a function of baryonic chemical potential for the NRAPR Skyrme interaction and (a) $T = 2$, (b) $T = 4$, and (c) $T = 6$ MeV. Left branch: uniform matter; Right branch: pasta phase.

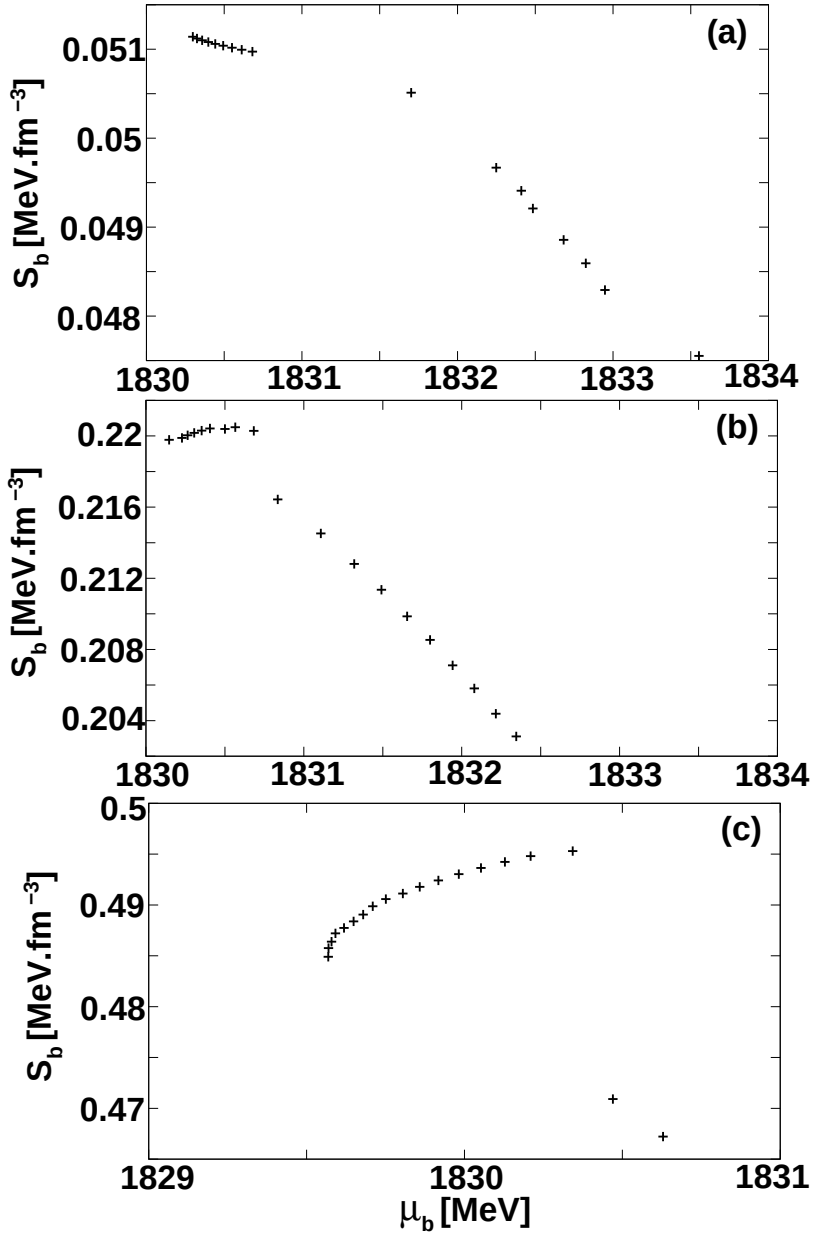

Figure 4.28: Baryonic entropy density as a function of baryonic chemical potential for the SLy4 Skyrme interaction and (a) $T = 2$, (b) $T = 4$, and (c) $T = 6$ MeV. Left branch: uniform matter; Right branch: pasta phase.

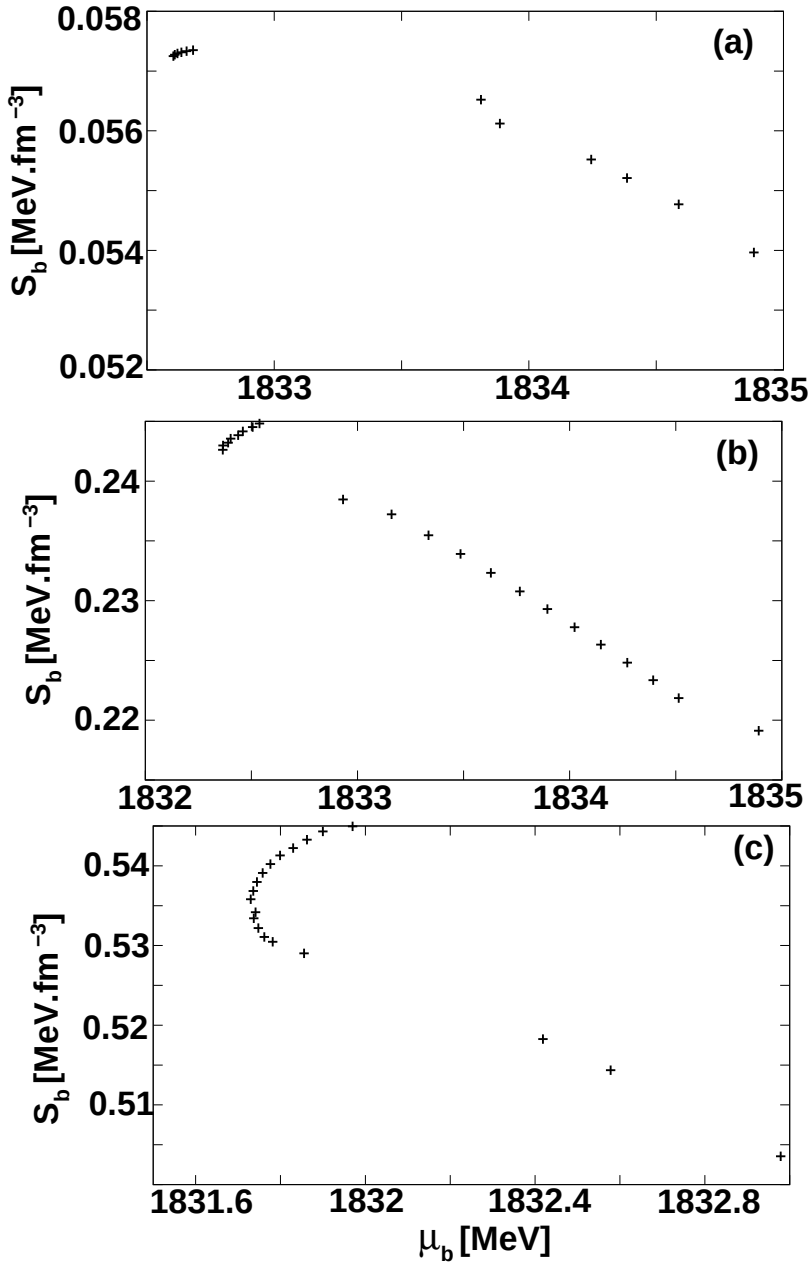

Figure 4.29: Baryonic entropy density as a function of baryonic chemical potential for the QMC Skyrme interaction and (a) $T = 2$, (b) $T = 4$, and (c) $T = 6$ MeV. Left branch: uniform matter; Right branch: pasta phase.

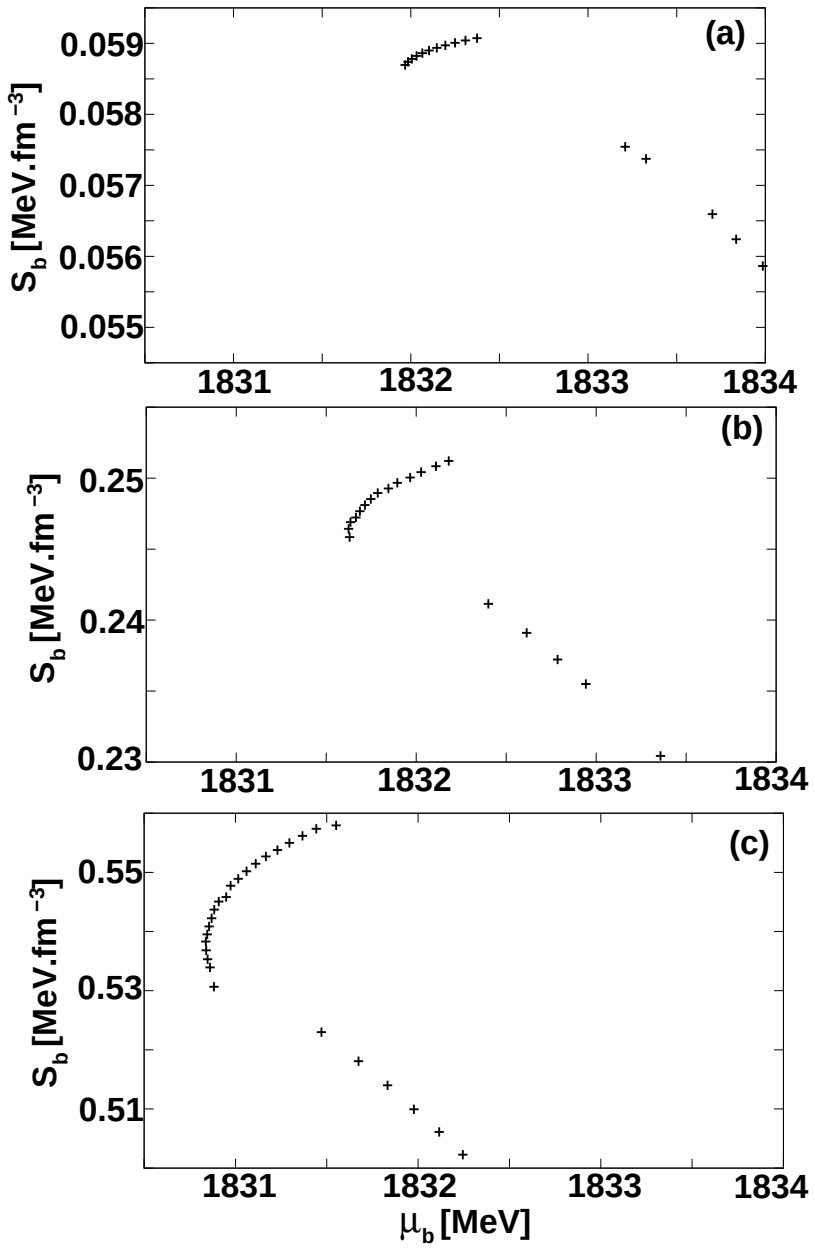

Figure 4.30: Baryonic entropy density as a function of baryonic chemical potential for the SkM* Skyrme interaction and (a) $T = 2$, (b) $T = 4$, and (c) $T = 6$ MeV. Left branch: uniform matter; Right branch: pasta phase.

The discontinuities shown in the first derivatives of the free energy, indicating a phase transition of first order at a specific temperature, coincide with the transitions to uniform matter in the neutron density distributions graphical analysis (see e.g. Fig. 4.6).

Chapter 5

Conclusions

We have proven, for the first time, that pasta is not just an empirical construction but arises naturally from a self-consistent model. We were able to localize all classical pasta formations in fully self-consistent calculations that lacked any preconceptions of the shape as input to the calculation. Possible shapes were somewhat limited by technical constraints on the calculation, as we assumed parity conservation (reflection symmetry) and a cubic shape of the unit cell, issues whose effect will be examined in the future.

Results of our analysis show some intriguing features, especially concerning the phase transition from the pasta phase to homogeneous matter (Maruyama and Tatsumi, 2010). First, we see a clear indication for the presence of the transition, manifesting itself at densities and temperatures in different observables, such as pressure, entropy and chemical potentials. We were able to identify jumps (of the order of $\mu_b = 1$ MeV) in all the first derivatives of the free energy, indicating the presence of a first-order phase transition to uniform matter. The inclusion of the pasta phase in our model hence does not remove the first order phase transition to uniform matter. Any discontinuities in the first derivatives of the free energy density at lower densities are too small to be identified and probably are at the limit of our numerical accuracy, preventing us from clearly identifying the character of

these smaller transitions between shapes. However we can observe that they happen gradually, with increasing density.

Second, we observe that for temperatures higher than 2 MeV, the transition density decreases with increasing temperature. Finally, we also find, for the first time, that the choice of the Skyrme interaction does not greatly affect the appearance and structure of the pasta phase of CCSN matter.

In conclusion, we have identified, fully self-consistently, the onset of the pasta phase in inhomogeneous CCSN matter consisting of neutron-rich heavy nuclei and a free neutron and electron gas and its dissolution to homogeneous neutron, proton and electron liquid. The density range of the pasta phase is temperature dependent; it decreases with increasing temperature. On the currently used density/temperature grid, all accepted shapes have been identified with one new cross-rod shape. The slab phase is found over the widest density range. Although this is true for all four interactions used, the particular widths of the various pasta phases show interesting variation. Consistent with the Avancini et al. (2012) result, we find that, for temperatures higher than 2 MeV, the transition density from the pasta phase to homogeneous matter decreases far more slowly with increasing temperature than the QMD result. A self-consistent calculation including the Coulomb field and finite size effects and allowing a large freedom for the pasta formation has been performed and we have obtained a first order pasta-uniform matter phase transition.

5.1 Future Work

The results of this work, extended to relevant temperatures and proton/neutron ratios, can be used to construct four EoS for supernova simulation models, augmented by 1D calculation at densities below and above the pasta region, where this approximation is valid. Neutron and proton density distributions in the unit cell, obtained in this work, can also be employed in the modelling of neutrino transport through the pasta formations, making such a calculation, where, for the first time,

a continuous particle density distribution rather than individual particles, is used. Another interesting analysis would be to identify the critical temperature at which the pasta phase disappears, in the range of proton fractions considered. On the technical side, it would be interesting to apply the Bloch boundary conditions and to remove the reflection symmetry to see if additional pasta shapes are possible.

Bibliography

Akmal, A., Pandharipande, V. R., and Ravenhall, D. G. (1998). *Phys. Rev. C*, 58:1804. 22

Arnett, D. (1996). *Supernovae and Nucleosynthesis: An Investigation of the History of Matter, from the Big Bang to the Present*. Princeton University Press, Princeton, New Jersey. 4

Avancini, S. S., Brito, L., Chomaz, P., Menezes, D. P., and Providência, C. (2006). *Phys. Rev. C*, 74:024317. 73

Avancini, S. S., Brito, L., Marinelli, J. R., Menezes, D. P., de Moraes, M. M. W., Providência, C., and Santos, A. M. (2009). *Phys. Rev. C*, 79:035804. 10

Avancini, S. S., Chiacchiera, S., Menezes, D. P., and Providência, C. (2010). *Phys. Rev. C*, 82:055807. 9, 10, 69

Avancini, S. S., Chiacchiera, S., Menezes, D. P., and Providência, C. (2012). *Phys. Rev. C*, 85:059904(E). x, 66, 69, 71, 74, 104

Avancini, S. S., Menezes, D. P., Alloy, M. D., Marinelli, J. R., Moraes, M. M. W., and Providência, C. (2008). *Phys. Rev. C*, 78:015802. 8, 10

Baldo, M., Burgio, G. F., and Schulze, H.-J. (2000). *Phys. Rev. C*, 61:055801. 22

Baran, V., Colonna, M., Greco, V., and Di Toro, M. (2005). *Phys. Rep.*, 410:335. 1

Baranger, M. (1963). *Phys. Rev.*, 130:1244. 32

Bardeen, J. M., Cooper, L. M., and Schrieffer, J. R. (1957). *Phys. Rev.*, 106:162. 30

Bartel, J., Quentin, P., Brack, M., Guet, C., and Håkansson, H.-B. (1982). *Nucl. Phys. A*, 386:79. 13

Bender, M., Reinhard, P.-G., Rutz, K., and Maruhn, J. A. (2000). *Eur. Phys. J. A*, 8:59. 31, 51, 52

Bethe, H. A. (1990). *Rev. Mod. Phys.*, 62:801. 4

Bethe, H. A., Applegate, J. H., and Brown, G. E. (1980). *Astrophys. J.*, 241:343. 8

Bethe, H. A., Brown, G. E., Applegate, J., and Lattimer, J. M. (1979). *Nucl. Phys. A*, 324:487. 8

Bethe, H. A. and Wilson, J. R. (1985). *Astrophys. J.*, 295:14. 5

Bisconti, C., de Saavedra, F. A., Co, G., and Fabrocini, A. (2006). *Phys. Rev. C*, 73:054304. 22

Blondin, J. and Mezzacappa, A. (2006). *Astrophys. J.*, 642:401. 6

Blondin, J., Mezzacappa, A., and DeMarino, C. (2003). *Astrophys. J.*, 584:971. 6

Bogoliubov, N. N. (1959). *Sov. Phys. Usp.*, 2:236. 32

Bombaci, I. and Lombardo, U. (1991). *Phys. Rev. C*, 44:1892. 22

Bonche, P., Flocard, H., Heenen, P. H., Krieger, S. J., and M. S. Weiss, M. (1985). *Nucl. Phys. A*, 443:39. 52

Bonche, P. and Vautherin, D. (1981). *Nucl. Phys. A*, 372:496. 10, 35, 71

Bonche, P. and Vautherin, D. (1982). *Astron. Astrophys.*, 112:268. 10

Brink, D. M. and Boeker, E. (1967). *Nucl. Phys. A*, 91:1. 22

Brito, L., Providência, C., Santos, A. M., Avancini, S. S., Menezes, D. P., and Chomaz, P. (2006). *Phys. Rev. C*, 74:045801. 12

Brown, B. A. (2000). *Phys. Rev. Lett.*, 85:5296. 2

Brown, G. E., Bethe, H. A., and Baym, G. (1982). *Nucl. Phys. A*, 375:481. 8

Brueckner, K. A. (1955). *Phys. Rev.*, 97:1353. 25

Bruenn, S. W. (1985). *Astrophys. J. Supp. S.*, 58:771. 5

Bruenn, S. W., De Nisco, K. R., and Mezzacappa, A. (2001). *Astrophys. J.*, 560:326. 5

Bruenn, S. W., Dirk, C. J., Mezzacappa, A., Hayes, J. C., Blondin, J. M., Hix, W. R., and Messer, O. E. B. (2006). *J. Phys. Conf. Ser.*, 46:393. 6

Bruenn, S. W., Mezzacappa, A., Hix, W. R., Blondin, J. M., Marronetti, P., Messer, O. E. B., Dirk, C. J., and Yoshid, S. (2009). *J. Phys. Conf. Ser.*, 180:012018. 6

Buras, R., Rampp, M., Janka, H.-T., and Kifonidis, K. (2003). *Phys. Rev. Lett.*, 90:241101. 6

Buras, R., Rampp, M., Janka, H.-T., and Kifonidis, K. (2006). *Astron. Astrophys.*, 447:1049. 6

Burrows, A. and Goshy, J. (1993). *Astrophys. J.*, 416:75. 6

Burrows, A., Hayes, J., and Fryxell, B. A. (1995). *Astrophys. J.*, 450:830. 6

Burrows, A. and Lattimer, J. M. (1985). *Astrophys. J.*, 299:19. 5

Burrows, A. and Lattimer, J. M. (1986). *Astrophys. J.*, 307:178. 5

Burrows, A., Livne, E., Dessart, L., Ott, C. D., and Murphy, J. (2006). *Astrophys. J.*, 640:878. 7

Burrows, A., Livne, E., Dessart, L., Ott, C. D., and Murphy, J. (2007). *Astrophys. J.*, 655:416. 7

Carlson, J., Morales, Jr., J., Pandharipande, V. R., and Ravenhall, D. G. (2003). *Phys. Rev. C*, 68:025802. 22

Chabanat, E., Bonche, P., Haensel, P., Meyer, J., and Schaeffer, R. (1997). *Nucl. Phys. A*, 627:710. 25

Chabanat, E., Bonche, P., Haensel, P., Meyer, J., and Schaeffer, R. (1998). *Nucl. Phys. A*, 635:231. 13

Chandrasekhar, S. (1931). *Astrophys. J.*, 74:81. 4

Chomaz, P., Colonna, M., and Randrup, J. (2004). *Phys. Rep.*, 389:263. 12

Cugnon, J., Deneye, P., and Lejeune, A. (1987). *Z. Phys. A*, 328:409. 22

Cusson, R. Y., Reinhard, P.-G., Strayer, M. R., Maruhn, J. A., and Greiner, W. (1985). *Z. Phys. A - Atoms and Nuclei*, 320:475. 55

Danielewicz, P. and Lee, J. (2009). *Nucl. Phys. A*, 818:36. 2

Day, B. D. (1967). *Rev. Mod. Phys.*, 39:719. 25

Day, B. D. and Wiringa, R. B. (1985). *Phys. Rev. C*, 32:1057. 22

de Jong, F. and Lenske, H. (1998). *Phys. Rev. C*, 57:3099. 22

Decharge, J. and Gogny, D. (1980). *Phys. Rev.*, 21:1568. 22

Dewulf, Y., Dickhoff, W. H., Neck, D. V., Stoddard, E. R., and Waroquier, M. (2003). *Phys. Rev. Lett.*, 90:152501. 22

Dorso, C. O., Giménez Molinelli, P. A., and López, J. A. (2012). *Phys. Rev. C*, 86:055805. 12

Dutra, M., Lourenço, O., Sá Martins, J. S., Delfino, A., Stone, J. R., and Stevenson, P. D. (2012). *Phys. Rev. C*, 85:035201. 2, 13, 22, 23, 33

Fabricioni, A. and Fantoni, S. (1993). *Phys. Lett. B*, 298:263. 22

Fock, V. A. (1930). *Z. Phys.*, 61:126. 27, 28

Frick, T. and Müther, H. (2003). *Phys. Rev. C*, 68:034310. 22

Frigo, M. and Johnson, S. G. (2005). *Proceedings of the IEEE*, 93(2):216–231. 56

Fryer, C. L. and Warren, M. S. (2002). *Astrophys. J.*, 574:65. 6

Fryer, C. L. and Warren, M. S. (2004). *Astrophys. J.*, 601:391. 6

Fuchs, C. (2006). *Prog. Part. Nucl. Phys.*, 56:1. 2

Gandolfi, S., Illarionov, A. Y., Fantoni, S., Pederiva, F., and Schmidt, K. E. (2008). *Phys. Rev. Lett.*, 101:132501. 22

Gandolfi, S., Illarionov, A. Y., Schmidt, K. E., Pederiva, F., and Fantoni, S. (2009). *Phys. Rev. C*, 79:054005. 22

Gandolfi, S., Pederiva, F., Fantoni, S., and Schmidt, K. E. (2007). *Phys. Rev. Lett.*, 99:022507. 22

Garg, U., Li, T., Okumura, S., Akimune, H., Fujiwara, M., Harakeh, M., Hashimoto, H., Itoh, M., Iwao, Y., Kawabata, T., Kawase, K., Liu, Y., Marks, R., Murakami, T., Nakanishi, K., Nayak, B., Rao, P. M., Sakaguchi, H., Terashima, Y., Uchida, M., Yasuda, Y., Yosoi, M., and Zenihirof, J. (2007). *Nucl. Phys. A*, 788:36. 2

Gögelein, P., van Dalen, E. N. E., Fuchs, C., and Müther, H. (2008). *Phys. Rev. C*, 77:25802. 10

Greiner, W. and Maruhn, J. A. (1996). *Nuclear Models*. Springer. 20, 21, 28, 29, 30, 35, 47, 48, 54

Greiner, W., Neiser, L., and Stöcker, H. (1997). *Thermodynamics and Statistical Mechanics*. Springer, second edition. 14, 15, 18

Guichon, P. A. M., Matevosyan, H. H., Sandulescu, N., and Thomas, A. W. (2006). *Nucl. Phys. A*, 772:1. 13

Hartree, D. R. (1928). *Proc. Camb. Phil. Soc.*, 24:89. 27, 28

Hebeler, K., Lattimer, J. M., Pethick, C. J., and Schwenk, A. (2010). *Phys. Rev. Lett.*, 105:161102. 22

Hebeler, K. and Schwenk, A. (2010). *Phys. Rev. C*, 82:014314. 22

Herant, M., Benz, W., Hix, W. R., Fryer, C. L., and Colgate, S. A. (1994). *Astrophys. J.*, 435:339. 6

Hix, W. R. (2013). private communication. 7

Horowitz, C. J., Perez-Garcia, M. A., Berry, D. K., and Piekarewicz, J. (2005). *Phys. Rev. C*, 72:035801. 8

Horowitz, C. J., Perez-Garcia, M. A., Carriere, J., Berry, D. K., and Piekarewicz, J. (2004a). *Phys. Rev. C*, 70:065806. 12, 13

Horowitz, C. J., Perez-Garcia, M. A., and Piekarewicz, J. (2004b). *Phys. Rev. C*, 69:045804. 8, 12, 13

Horowitz, C. J. and Piekarewicz, J. (2001). *Phys. Rev. Lett.*, 86:5647. 2

Janka, H.-T. (2001). *Astron. Astrophys.*, 368:527. 6

Janka, H.-T. (2012). *Annu. Rev. Nucl. Part. Sci.*, 62:407. 7

Janka, H.-T., Kifonidis, K., and Rampp, M. (2001). *arXiv:astro-ph/0103.015v1*. 5

Janka, H.-T. and Müller, E. (1996). *Astron. Astrophys.*, 306:167. 6

Keil, W., Janka, H.-T., and Müller, E. (1996). *Astron. Astrophys.*, 473:111. 6

Klähn, T., Blaschke, D., Typel, S., van Dalen, E. N. E., Faessler, A., Fuchs, C., Gaitanos, T., Grigorian, H., Ho, A., Kolomeitsev, E. E., Miller, M. C., Röpke, G., Trümper, J., Voskresensky, D. N., Weber, F., and Wolter, H. H. (2006). *Phys. Rev. C*, 74:035802. 3

Köhler, H. S. (1965a). *Phys. Rev.*, 137:1145. 22

Köhler, H. S. (1965b). *Phys. Rev.*, 138:831. 22

Kolomietz, V. M. and Shlomo, S. (2004). *Phys. Rep.*, 390:133. 12

Lalazissis, G. A., König, J., and Ring, P. (1997). *Phys. Rev. C*, 55:540. 76

Lamb, D. Q., Lattimer, J. M., Pethick, C. J., and Ravenhall, D. G. (1983). *Nucl. Phys. A*, 411:449. 9, 73, 84

Landau, L. D. and Lifshitz, E. M. (1980). *Statistical Physics — Part 1.* Pergamon Press, third edition. 14, 16, 17

Langanke, K., Maruhn, J. A., and S. E. Koonin, S. (1991). *Computational Nuclear Physics 1: Nuclear Structure.* Springer-Verlag. 32, 60

Lassaut, M., Flocard, H., Bonche, P., Heenen, P. H., and Suraud, E. (1987). *Astron. Astrophys.*, 183:L3. 9

Lattimer, J. M. and Prakash, M. (2007). *Phys. Rep.*, 442:109. 1

Lattimer, J. M. and Swesty, F. D. (1991). *Nucl. Phys. A*, 535:331. 9, 11, 71

Lenk, R. J. and Pandharipande, V. R. (1986). *Phys. Rev. C*, 34:177. 12

Lenk, R. J., Schlagel, T. J., , and Pandharipande, V. R. (1990). *Phys. Rev. C*, 42:372. 12

Lentz, E. J., Mezzacappa, A., Messer, O. E. B., Hix, W. R., and Bruenn, S. W. (2012). *Astrophys. J.*, 760:94. 7

Li, B.-A., Chen, L.-W., and Ko, C.-M. (2008). *Phys. Rep.*, 464:113. 1, 2

Li, B.-A., Yong, G.-C., and Zuo, W. (2005). *Phys. Rev. C*, 71:014608. 2

Liebendörfer, M., Messer, O. E. B., Mezzacappa, A., Bruenn, S. W., Cardall, C. Y., and Thielemann, F.-K. (2004). *Astrophys. J. Supp. S.*, 150:263. 6

Liebendörfer, M., Mezzacappa, A., Thielemann, F.-K., Messer, O. E. B., Hix, W. R., and Bruenn, S. W. (2001). *Phys. Rev. D*, 63:103004. 6

Magierski, P. and Heenen, P.-H. (2002). *Phys. Rev. C*, 65:045804. 10

Marek, A. and Janka, H.-T. (2009). *Astrophys. J.*, 694:664. 6

Maruyama, T., Niita, K., Oyamatsu, K., Maruyama, T., Chiba, S., and Iwamoto, A. (1998). *Phys. Rev. C*, 57:655. 11

Maruyama, T. and Tatsumi, T. (2010). *arXiv:1009.1198v1 [nucl-th]*. 103

Maruyama, T., Tatsumi, T., Voskresensky, D., Tanigawa, T., and Chiba, S. (2005). *Phys. Rev. C*, 72:015802. 8

Mezzacappa, A. (2005). *Annu. Rev. Nucl. Part. Sci.*, 55:467. 8

Mezzacappa, A. and Bruenn, S. W. (2000). *J. Italian Astron. Soc.*, 71:515. 5

Mezzacappa, A., Calder, A. C., Bruenn, S. W., Blondin, J. M., Guidry, M. W., Strayer, M. R., and Umar, A. S. (1998a). *Astrophys. J.*, 495:911. 6

Mezzacappa, A., Calder, A. C., Bruenn, S. W., Blondin, J. M., Guidry, M. W., Strayer, M. R., and Umar, A. S. (1998b). *Astrophys. J.*, 493:848. 6

Mezzacappa, A. and Messer, O. E. B. (1999). *J. Comput. Appl. Math.*, 109:281. 5, 6

Miralles, J. A. and Riper, K. A. V. (1996). *Ap. J. S.*, 105:407. 40

Moszkowski, S. A. (1970). *Phys. Rev. C*, 2:402. 22

Mueller, B., Janka, H.-T., and Marek, A. (2012). *Astrophys. J.*, 756:84. 6

Mukherjee, A. and Pandharipande, V. R. (2007). *Phys. Rev. C*, 75:035802. 22

Müller, H. and Serot, B. D. (1995). *Phys. Rev. C*, 52:2072. 15, 16, 17, 76

Negele, J. W. and Vautherin, D. (1973). *Nucl. Phys. A*, 207:298. 25, 49, 71

Newton, W. G. (2008). PhD thesis, Oxford University. 12, 25, 27, 28, 29, 32, 35, 40, 42, 47, 49, 53

Newton, W. G. and Stone, J. R. (2009). *Phys. Rev. C*, 79:055801. 9, 10, 12, 71

Pais, H. and Stone, J. R. (2012). *Phys. Rev. Lett.*, 109:151101. 64

Pandharipande, V. R. and Ravenhall, D. G. (1989). *Hot Nuclear Matter*. 35

Press, W. H., Teukolsky, S. A., Vetterling, W. T., and Flannery, B. P. (2007). *Numerical recipes in FORTRAN: The art of scientific computing*. Cambridge University Press, 3rd edition. 52, 58

Providência, C., Brito, L., Avancini, S. S., Menezes, D. P., and Chomaz, P. (2006a). *Phys. Rev. C*, 73:025805. 12

Providência, C., Brito, L., Santos, A. M. S., Menezes, D. P., and Avancini, S. S. (2006b). *Phys. Rev. C*, 74:045802. 12

Pudliner, B. S., Pandharipande, V. R., Carlson, J., Pieper, S. C., and Wiringa, R. B. (1997). *Phys. Rev. C*, 56:1720. 22

Raduta, A. and Gulminelli, F. (2010). *Phys. Rev. C*, 82:065801. 16

Rampp, M. and Janka, H.-T. (2002). *Astron. Astrophys.*, 396:361. 6

Ravenhall, D. G., Pethick, C. J., and Wilson, J. R. (1983). *Phys. Rev. Lett.*, 50:2066. 8, 9, 69

Reinhard, P.-G. and Cusson, R. Y. (1982). *Nucl. Phys. A*, 378:418. 50

Ring, P. and Schuck, P. (1980). *The Nuclear Many-Body Problem*. Springer-Verlag, New York. 24, 25, 35

Sagert, I., Hempel, M., Pagliara, G., Schaffner-Bielich, J., Fischer, T., Mezzacappa, A., Thielemann, F.-K., and Liebendörfer, M. (2009). *J. Phys. G*, 36:064009. 3

Schmidt, K. E. and Fantoni, S. (1999). *Phys. Lett. B*, 446:99. 22

Shapiro, S. L. and Teukolsky, S. A. (1986). *Black Holes, White Dwarfs and Neutron Stars: The Physics of Compact Objects*. Wiley-VCH. 39

Shen, G., Horowitz, C. J., and O'Connor, E. (2011a). *Phys. Rev. C*, 83:065808. 11

Shen, G., Horowitz, C. J., and Teige, S. (2010a). *Phys. Rev. C*, 82:045802. 11

Shen, G., Horowitz, C. J., and Teige, S. (2010b). *Phys. Rev. C*, 82:015806. 11

Shen, G., Horowitz, C. J., and Teige, S. (2011b). *Phys. Rev. C*, 83:035802. 11

Shen, H., Toki, H., Oyamatsu, K., and Sumiyoshi, K. (1998). *Nucl. Phys. A*, 637:435. 11

Skyrme, T. H. R. (1956). *Phil. Mag.*, 1:1043. 22, 23

Slater, J. C. (1929). *Phys. Rev.*, 34:1293. 28

Slater, J. C. (1951). *Phys. Rev.*, 81:385. 56

Sonoda, H., Watanabe, G., Sato, K., Takiwaki, T., Yasuoka, K., and Ebisuzaki, T. (2007). *Phys. Rev. C*, 75:042801(R). 11, 13

Sonoda, H., Watanabe, G., Sato, K., Yasuoka, K., and Ebisuzaki, T. (2008). *Phys. Rev. C*, 77:035806. x, xii, 8, 66, 69, 70, 71, 73, 74

Sonoda, H., Watanabe, G., Sato, K., Yasuoka, K., and Ebisuzaki, T. (2010). *Phys. Rev. C*, 81:049902. 8

Steiner, A. W., Prakash, M., Lattimer, J. M., and Ellis, P. J. (2005). *Phys. Rep.*, 411:325. 1, 13

Stevenson, P., Strayer, M. R., and Stone, J. R. (2001). *Phys. Rev. C*, 63:054309. 23

Stone, J. R. and Reinhard, P.-G. (2007). *Prog. Part. Nucl. Phys.*, 58:587. 8, 31

Stone, J. R., Stevenson, P. D., Miller, J. C., and Strayer, M. R. (2002). *Phys. Rev. C*, 65:064312. 23

Swesty, F. D. (1998). *Gray models of convection in core-collapse supernovae*. IOP, Bristol. 6

Tatsumi, T., Yasutake, N., and Maruyama, T. (2011). *arXiv:1107.0804[nucl-th]*. 76

ter Haar, B. and Malfliet, R. (1987). *Phys. Rep.*, 149:207. 22

Thompson, T. A., Burrows, A., and Pinto, P. A. (2003). *Astrophys. J.*, 592:434. 6

Tsang, M. B., Stone, J. R., Camera, F., Danielewicz, P., Gandolfi, S., Hebeler, K., Horowitz, C. J., Lee, J., Lynch, W. G., Kohley, Z., Lemmon, R., Möller, P., Murakami, T., Riordan, S., Roca-Maza, X., Sammarruca, F., Steiner, A. W., Vidaña, I., and Yennello, S. J. (2012). *Phys. Rev. C*, 86:015803. 2, 3

Typel, S. and Brown, B. A. (2001). *Phys. Rev. C*, 64:027302. 2

van Dalen, E. N. E., Fuchs, C., and Faessler, A. (2004). *Nucl. Phys. A*, 741:227. 22

Vautherin, D. and Brink, D. M. (1972). *Phys. Rev. C*, 5:626. 22, 25, 29

Vicentini, A., Jacucci, G., and Pandharipande, V. R. (1985). *Phys. Rev. C*, 31:1783. 12

Vidaña, I., Polls, A., Ramos, A., Engvik, L., and Hjorth-Jensen, M. (2000). *Phys. Rev. C*, 62:035801. 22

Vidaña, I., Providência, C., Polls, A., and Rios, A. (2009). *Phys. Rev. C*, 80:045806. 2, 15

Watanabe, G., Iida, K., and Sato, K. (2001). *Prog. Theor. Phys.*, 106:551. 11

Watanabe, G., Maruyama, T., Sato, K., Yasuoka, K., and Ebisuzaki, T. (2005). *Phys. Rev. Lett.*, 94:031101. 8

Watanabe, G. and Sonoda, H. (2005). *AIP Conf. Proceed.*, 791:101. 11

Watanabe, G., Sonoda, H., Maruyama, T., Sato, K., Yasuoka, K., and Ebisuzaki, T. (2009). *Phys. Rev. Lett.*, 103:121101. 73

Williams, R. D. and Koonin, S. E. (1985). *Nucl. Phys. A*, 435:844. 7, 8, 11, 69, 73, 84

Wilson, J. R. (1985). *Supernovae and Post-Collapse Behavior*. Jones and Bartlett Publ., Boston. 5

Wilson, J. R. and Mayle, R. W. (1993). *Phys. Rep.*, 227:97. 5, 6

Young, H. D. and Freedman, R. A. (2008). *Sears and Zemansky's university physics: with modern physics*. Pearson Addison-Wesley, 12th edition. 19

Zuo, W., Lejeune, A., Lombardo, U., and Mathiot, J. F. (2002). *Eur. Phys. J. A*, 14:469. 22

Vita

Helena Sofia de Castro Felga Ramos Pais was born on January 21st, 1981 in Porto, Portugal. After attending high school, she moved to Coimbra, where she got her Bachelor's degree in Physics. She then got a grant from the Portuguese Foundation for Science and Technology (FCT) to support Master thesis' studies at the University of Coimbra, under the supervision of Professor Constança Providência. The research project was on quark stars in a strong magnetic field, where the MIT bag model was used to study the EoS for quark matter with and without external magnetic fields. The phase transition between hadronic and quark matter was investigated and the Tolman-Oppenheimer-Volkoff (TOV) equations were integrated in order to obtain the mass-radius relation for hadronic, quark and hybrid stars. The results were presented at a CompStar workshop in Coimbra 2009 and the material of the poster was published in *Journal of Physics G*. After defended her Master's thesis, she got a Research Grant (Bolsa de Investigação) from FCT at the same institution working with the same group, where they focused their studies on the collective modes of relativistic asymmetric nuclear matter at both zero and finite temperature, with the inclusion of the δ meson, in the framework of a relativistic mean-field theory model, using the Vlasov formalism. The results were presented at a summer school in Huelva, Spain, 2009 and form the content of two papers in *Physical Review C*. She then moved to Knoxville, TN, USA, where she started working on her PhD thesis, under the supervision of Professor Jirina R. Stone. They have been working on the nuclear pasta phase at finite temperatures, using the 3D Skyrme-Hartree-Fock (HF)

model, for core-collapse supernova matter. The phase transition between uniform and non-uniform (pasta phase) matter and its dependence on density and temperature, and the choice of the Skyrme interaction, have been the subject of their studies, as well as the construction of the EoS table for use in Core-Collapse Supernovae (CCS) and Neutron Stars (NS) simulations. Preliminary results were presented at the CompStar Workshop in Catania, Sicily, 2011, and at the International Workshop on Baryon and Lepton Number Violation in Gatlinburg, Tennessee, 2011. Their first results have been published in *Physical Review Letters* and another article is being prepared for publication.